MINIATURIZED GUIDED WAVE STRUCTURES AND APPLICATIONS

A thesis submitted to the University of KENT
for the degree of Doctor of Philosophy
in Electronic Engineering

by

Ruo Feng Xu

September 2010

To my parents...

Abstract

This thesis examines the properties of novel transmission lines and waveguides as well as their practical applications. The research begins with a discussion of metamaterial transmission lines. Two new composite right/left-handed designs formed in shielded striplines are presented and shown to have great left-handed bands.

In the waveguides research, we demonstrate the multilayer, narrowband and half-mode folded waveguide with the benefit of guide miniaturization. Due to the almost half metallic surface reduction of half-mode waveguide, a novel planar half-mode substrate integrated waveguide is presented and its properties are analyzed. It has the great integration with planar components and stops the radiation of conventional open waveguides. One application based on this medium is a novel switchable substrate waveguide that can be switched between two types of mode via the biasing of pin diodes. Another application is a tunable phase shifter that has a maximum phase shift of 50 degrees with acceptable insertion loss.

A theoretical method for the analysis of planar half-mode waveguides using transverse resonance technique is introduced in this thesis. This method is used to locate the cut-off frequency of the waveguide and analyse the equivalent circuit loaded with discrete components. This novel technique has the advantage of simplicity and compares well with results of electromagnetic simulation and measurement.

Acknowledgement

My deepest gratitude goes first and foremost to Dr P. R. Young, my supervisor, for his constant encouragement and guidance. He has walked me through all the stages of the research with his consistent and illuminating instruction. Dr P. R. Young has not only been an excellent supervisor but a good friend as well.

I would also like to express my heartfelt gratitude to Mr Adam Jastrzebski, Mr Simon Jakes and Dr B. Sanz Izquierdo who have instructed and helped me a lot in these years and all the staff in School of Engineering and Digital Arts of the University of KENT.

CONTENTS

List of publications arising from this thesis:

- *Shielded stripline left-handed transmission line*, R. F. Xu and P. R. Young, 3rd International Congress on Advanced Electromagnetic Materials in Microwaves and Optics – Metamaterials, London, September 2009.

- *Switchable Substrate integrated waveguide*, R. F. Xu, B. Sanz Izquierdo and P. R. Young, accepted by IEEE microwave wireless component letter.

- *Tunable phase shifter in substrate integrated waveguide*, R. F. Xu, B. Sanz Izquierdo and P. R. Young, accepted by Antennas and propagation symposium 2010 in Cochin, India, Dec 2010.

- Theoretical analyses by using transverse resonance technique, R. F. Xu and P. R. Young, in preparation for IEEE journal.

Variables in this thesis:

ε_r - relative permittivity of the dielectric material

γ - propagation constant

α - attenuation constant

β - phase constant

λ - wavelength

f, ω - frequency; f_c, ω_c - cut off frequency

V_p - phase velocity

V_g - group velocity

c - speed of light

C - capacitance; L - inductance

V - voltage; I - current

R, r - resistance

δ - loss tangent

σ - conductivity

$|\boldsymbol{k}|$ - wavevector

η - intrinsic impedance of the medium

ϵ_0 - permittivity of free space

μ_0 - permeability of free space

k_0 - free space wave-number

Q - quality factor

Abbreviations in this thesis:

RWG - rectangular waveguides

SIW - substrate integrated waveguide

SIFW - substrate integrated folded waveguide

FHMSIW - folded half-mode substrate integrated waveguide

MIC - microwave integrated circuit

LTCC - low-temperature co-fired ceramic

HMSIW - half-mode substrate integrated waveguide

WHR - width-to-height ratio

MTMs - metamaterials

CRLH - composite right/left-handed

LH – left-handed

RH – right-handed

PLH – purely left-handed

PRH – purely right-handed

PCB - printed circuit board

SMA - SubMiniature version A

PTFE - polytetrafluoroethylene

TRT - transverse resonance technique

1. Introduction

The fundamental theory of electromagnetics was developed over 100 years ago. The microwave engineering benefits resulting from the properties of electromagnetic waves at higher frequencies which correspond to short wavelengths are well known [1]. The great advantages of small size, good performance and modern fabrication procedures make the applications of microwave systems very extensive. These include wireless communication systems, radar systems and intelligent transportation systems. Typically microwave circuits containing active devices are fabricated using planar transmission lines such as microstrip and coplanar waveguide. However, the large conductive, radiation loss and low power handling capability limit microstrip lines and coplanar waveguides to lower microwave frequencies.

Rectangular waveguides (RWG) have very low losses and high power-handling capability. They solve the radiation and crosstalk problem in the transmission lines and have the applications in high-power systems and millimeter wave systems. The RWGs can propagate TM and TE modes. Unfortunately traditional RWGs are bulky three-dimensional structures that are often referred to as "plumbing" due to their unwieldy nature. The techniques to fabricate RWGs using circuit and monolithic fabrication techniques have been proposed, such as bulk micromachining of silicon [2] and photoimageable spin-on materials [3]. However, the fabrication procedures are complicated and the guided wavelength is large because of the air-filled nature of guides. Furthermore, they are difficult to integrate with planar circuits and the size is too large.

Over years' developments, an alternative method is to use dielectric-filled RWG. Dielectric materials can be gases, liquids and solids, for example ceramics, glasses, plastics, nitrogen etc. A dielectric-filled waveguide by spray coating a dielectric rod with metal had been demonstrated by Hinken [4] in 1980. In 1995, Lucyszyn first presented the monolithic

dielectric-filled metal-pipe RWG [5] [6]. Dielectric-filled RWGs can be fabricated photolithographically by employing multilayer processing and using photoimageable thick film materials [7]. This new technique achieved improvements in the edge definition and smaller sizes. To solve the large conductive loss issues, Kinayman [8] demonstrated a low loss glass filled waveguide which is formed by etching pedestals from a silicon glass wafer. However, due to the many processing steps, the cost was not cheap.

Quite a few new waveguides have been investigated to overcome the problem of size reductions and cost, such as the substrate integrated waveguide (SIW) which is embedded into a microwave substrate. A generic SIW report which introduced a rectangular waveguide integrated into a substrate was first proposed in 1998 by Lucyszyn [9]. The SIW is a very promising microwave and millimeter-wave medium. And techniques have been developed to fabricate SIWs, using low-temperature co-fired ceramic (LTCC) [10], and standard microwave integrated circuit (MIC) [11] etc. In these techniques, series of vias are used to form the sidewall of the guides with metallization on the top and bottom substrates. In [12], a 2D lattice of plated via holes are used to form the sidewalls of a RWG using microwave laminates [13]. While keeping the advantages of conventional rectangular waveguides, the dielectric filled waveguides have low cost, easy integration and size reduced by a factor of $\varepsilon_r^{-1/2}$, where ε_r is the permittivity of the dielectric material. However, these waveguides are still large for some applications at lower microwave frequencies.

In recent years, two size reduction methods have become popular. The first one is the substrate integrated folded waveguide (SIFW) [14]. Maintaining all the advantages of SIW, it has a further reduction on the transverse size. Another one is the half-mode substrate integrated waveguide (HMSIW) [15], which have the size reduction on the total metallic cross sectional area.

The SIFW has a smaller package, compared with RWGs. In fact, since the height of the guide is not important, the volume of SIFW can be much smaller. It can be easily integrated with other planar devices and used at low millimeter-wave frequency range. This technique has been widely used in antenna systems [16], filter systems [17] and couplers [18] etc.

The HMSIW almost reduced the width and total metallic surface of the SIW by half. For the dominant mode of a SIW, it has the maximum E-field value in the symmetric central plane along the transmission direction. Thus, if the waveguide is cut into half along the vertical middle direction, the cutting plane can be considered as a magnetic wall. With the large width-to-height ratio (WHR), the HMSIW can still keep the original field distribution in order to propagate the half guided waves [15]. Based on this new technique, some components have been designed such as couplers [19], filters [20] and the propagation properties have been analyzed [21].

On the other hand, in recent years, electromagnetic metamaterials (MTMs) have been demonstrated with the properties of negative permittivity and permeability, backward-wave, left-handed propagation, etc [22]. The most popular application of the MTMs is the left-handed (LH) structure, in which the electric field, magnetic field and wave vector follow a left-hand rule rather than the conventional right-handed propagation. A practical transmission line is the composite right/left-handed (CRLH) line, which contains two pass bands - right and left-handed regions. A stop band may occur between them. Under the loss-less condition, the complex propagation constant of CRLH transmission line γ can be purely imaginary $\gamma = j\beta$ in the pass band and be purely real $\gamma = \alpha$ in the stop band. Dispersion and attenuation curves of CRLH line are shown in figure 1.1. For a given phase shift $\emptyset$ [figure 1.1 (a)], the signals can propagate at the lower frequency f_1 in the left-handed range, rather than the higher frequency f_2 in the right-handed range. Due to the frequency dependant wavelength λ ($\lambda = v/f$, v is the constant phase velocity of materials, f is the frequency), the size of the structure can be reduced corresponding to the reduced wavelength in LH region. In figure 1.1 (b), an example of group velocity (V_g) curves versus phase constant is shown. The group velocity presents the slope of the phase velocity (V_p), In left-handed range of CRLH line, the phase velocity becomes negative and the group velocity keeps positive. This causes the backward-wave propagation.

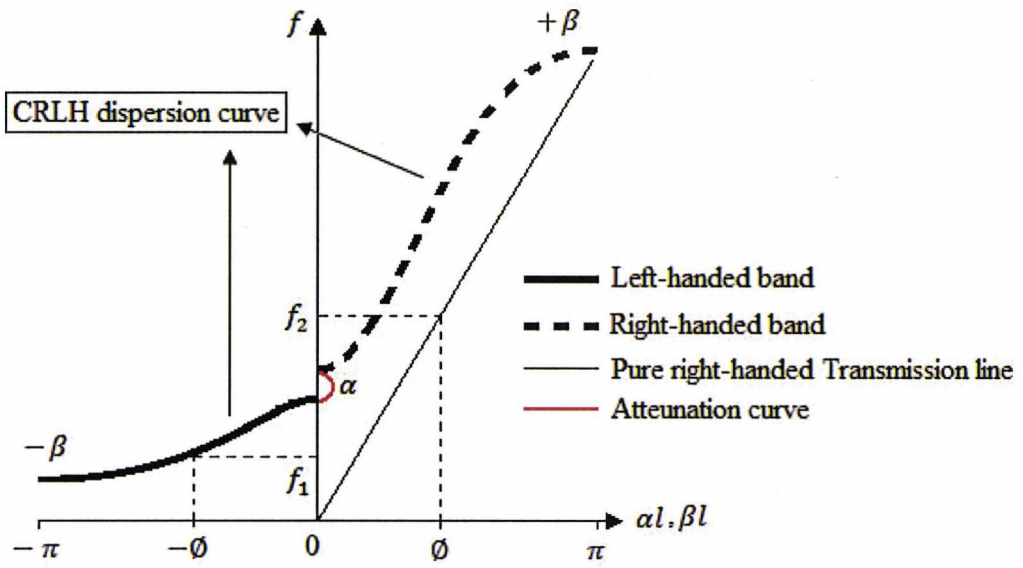

(a)

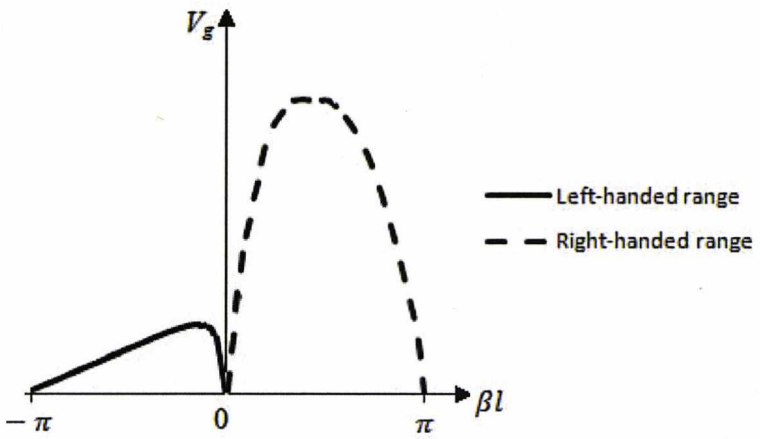

(b)

Figure 1.1. CRLH transmission line (a) dispersion and attenuation curves, (b) group velocity curves

In this thesis, we introduce the stripline CRLH lines, multilayer substrate integrated folded waveguides, half-mode substrate integrated waveguides and their novel applications.

Furthermore, theoretical analyses based on the transverse resonance technique are proposed to build up mathematical models for systematic researches.

1.1 Outline of thesis

The aim of this thesis is the development of miniaturized guided wave structures and applications.

Chapter 2 introduces the metamaterials line. Two novel types of CRLH transmission line formed in the shielded stripline have been simulated and fabricated. In the same chapter, a transmission matrix analysis is applied to define the equivalent circuit of the structure.

In chapter 3, a general discussion of multilayer substrate integrated folded waveguides is proposed, including the designs of transitions to microstrip transmission. Furthermore, the narrowband and half-mode waveguides are introduced.

In chapter 4, a novel planar half-mode substrate integrated waveguide is presented. We discussed the propagation properties and how the configuration of the structure affects the loss and bandwidth of the waveguide. Then, the determination of cut-off frequency of planar half-mode SIW is described by using transverse resonance technique.

Chapter 5 shows a novel switchable SIW based on the design of chapter 4. The propagating mode of the waveguide can be switched between two types of mode via the biasing of pin diodes.

In chapter 6, a further research based on the transverse resonance technique explains how loaded components in the SIW circuit affect properties of the propagations. Two situations – distributed capacitance and periodically load components are presented. Furthermore, a novel tunable phase shifter is demonstrated with the advantages of easy fabrication processing and small size.

Chapter 7 summarizes the results of the thesis and gives suggestions for the further research on the half-mode SIWs.

References

[1] David M. Pozar, "*Microwave Engineering*" third edition, John Wiley & Sons, Inc, ISBN 0-471-44878-8

[2] McGrath W.R., Walker C., Yap M. and Tai Y., "Silicon micromachined waveguides for millimeter-wave for millimeter-wave and submillimeter-wave frequencies," *IEEE Microw. Guided Wave Lett.*, vol. 3, no.3, pp.61-63, March 1993.

[3] Digby J. W., McIntosh C. E., Parkhurst G. M., Hadjiloucas J. W., Chamberlain J. M., Pollard R. D., Miles R. E., Steenson D. P., Cronin N. J. and Davies S. R., "Fabrication and characterization of micromachined rectangular waveguide components for use at millimeter-wave and terahertz frequencies," *IEEE Trans. Microwave Theory Tech.*, vol. 48, no. 8, pp. 1293-1302, Aug. 2000.

[4] Hinken J. H., "Waveguides become integrated circuits in new space and cost saving method," *MSN*, no. 9, pp. 106-118, Nov. 1983.

[5] Lucyszyn S., Budimir D., Wang Q.H., and Robertson, I.D., "Design of compact monolithic dielectric-filled metal-pipe rectangular waveguides for millimeter-wave applications," *IEE Proc. H, Microw. Antennas Propag.*, vol. 143, no. 5, pp. 451-453, 1996.

[6] Lucyszyn S., Wang Q.H., and Robertson, I.D., "0.1 THz rectangular waveguide on GaAs semi-insulating substrate," *Electron. Lett.*, vol. 31, no. 9, pp.721-722, 1995.

[7] Aftanasar M.S., Young P.R., Robertson I.D., Minalgiene J., Lucyszyn, S., "Photoimageable thick-film millimetre-wave metal-pipe rectangular waveguides," *Electron. Lett.*, vol. 37, no. 18, pp.1122-1123, August 2001.

[8] N. Kinayman, C. Eswarappa, N. Jatin and A. Buckle, "A novel surface-mountable millimeter-wave bandpass filter," *IEEE Microw. Wireless Compon. Lett.*, vol. 12, no. 3, pp. 76-78, March 2002.

[9] S. Lucyszyn, S. R. P. Silva, I. D. Robertson, R. J. Collier, A. K. Jastrzebski, I. G. Tayne and S. P. Beaumont, " Terahertz multi-chip module (T-MCM) technology for the 21st century?", IEE Colloquium Digest on Multi-Chip Modules and RFICs, London, pp.6/1-8, May 1998.

[10] H. Uchimura, T. Takenoshita, and M. Fujii, "Development of a laminated waveguide," *IEEE Trans. Microw. Theory Tech.,* vol. 46, no. 12, pp. 2438–2443, Dec. 1998.

[11] D. Deslandes and K.Wu, "Integrated microstrip and rectangular waveguide in planar form," *IEEE Microw. Guided Wave Lett.*, vol. 11, no. 2, pp. 68–70, Feb. 2001.

[12] C. Y. Chang and W. C. Hsu, "Photonic bandgap dielectric waveguide filter," *IEEE Microwave wireless Compon. Lett.,* vol. 12, no. 4 pp137-139, April 2002.

[13] J. Hirokawa and M. Ando, "Single-layer feed waveguide consisting of posts for plane TEM wave excitation in parallel plates," *IEEE Trans. Antennas Propag.*, vol. 46, no. 5, pp. 625–630, May 1998.

[14] N. Grigoropoulos and P. R. Young, "Compact folded waveguides," in *34th Eur. Microw. Conf.*, Amsterdam, Netherlands, pp. 973–976, 2004.

[15] W. Hong, B. Liu, Y. Q. Wang, Q. H. Lai, and K. Wu, "Half mode substrate integrated waveguide: a new guided wave structure for microwave and millimeter wave application," in *Proc. Joint 31st Int. Conf. Infrared Millim. Waves 14th Int. Conf. Terahertz Electron*, pp.219, Sep. 2006.

[16] B. Sanz Izquierdo, and P. R. Young, N.Grigoropoulos, J. C. Batchelor and R. J. Langley, "Substrate Integrated Folded Waveguides (SIFW) slot antenna," *Pro. IEEE Int. Workshop Antenna Technology,* pp. 307-309, Mar. 2005.

[17] N. Grigoropoulos, B. Sanz Izquierdo, and P. R. Young, "Substrate integrated folded waveguide (SIFW) and filters," *IEEE Microwave wireless compon. Lett.*, Vol. 15, No.12, pp.829-831, Dec. 2005.

[18] Guo Hua Zhai, Wei Hong, Ke Wu, Ji Xin Chen, Peng Chen, and Hong Jun Tang, " Substrate Integrated Folded Waveguide (SIFW) narrow-wall directional coupler, " *International Conference on Microwave and Millimeter Wave Technology,* vol.1, pp.174-177, 2008.

[19] B. Liu, W. Hong, Y.Q. Wang, Q. H. Lai, and K. Wu, "Half mode substrate integrated waveguide (HMSIW) 3-dB coupler," *IEEE Microw. Wireless Compon. Lett.,* vol. 17, no. 1, pp. 22-24, Jan. 2007.

[20] Y. Q. Wang, W. Hong, Y. D. Dong, B. Liu, H. J. Tang, J. X. Chen, X. X. Yin, and K. Wu, "Half mode substrate integrated waveguide (HMSIW) filter," *IEEE Microw. Wireless Compon. Lett.,* vol. 17, no. 4, pp. 265–267, Apr. 2007.

[21] Qinghua Lai, Fumeaux C., Wei Hong, Vahldieck R., "Characterization of the propagation properties of the half-Mode substrate integrated waveguide," *IEEE Trans. Microw. Theory Tech.*, vol 57, no. 8, Aug 2009.

[22] Christophe Caloz and Tatsuo Itoh, "*Electromagnetic Metamaterials*," Wiley Interscience, 2006.

2. Metamaterials lines

Electromagnetic metamaterials (MTMs) have been well developed in recent years. The MTMs structures are effectively homogeneous that the average cell size p is smaller than a quarter of wavelength ($\lambda/4$) and the condition $p=\lambda/4$ is the effective-homogeneity limit. MTMs have properties of equivalently negative permittivity ε and permeability μ that are unusual in nature [1]. Most of the metamaterial lines are periodic structures, which contain small electrical scatterers (inclusions) embedded into a dielectric host line. And the distance between neighbouring scatterers is much smaller than a wavelength. The scattering properties are similar to electric and magnetic polarizations, thus the permittivity ε and permeability μ of the host line may be modified to be negative [2]. The double negative parameters make the phase velocity V_p propagate in the opposite direction to the flow of energy, which relates to group velocity V_g. That is called backward-wave propagation [3].

The most popular application of the MTMs is the left-handed (LH) structure, in which the electric field, magnetic field and wave vector follow a left-hand rule rather than the conventional right-handed propagation. The pure LH circuit model consists of series capacitors and shunt inductors (figure 2.1).

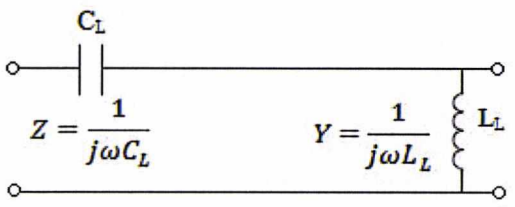

Figure 2.1. Pure left-handed circuit model of a single cell

A transmission line approach of metamaterials has been introduced [4-7]. In the lossless case, substituting Z and Y from figure 2.1 gives the propagation constant γ

$$\gamma = j\beta = \sqrt{ZY} = \frac{1}{j\omega\sqrt{L_L C_L}} = -j\frac{1}{\omega\sqrt{L_L C_L}} \tag{2.1}$$

Thus, the phase constant β is negative

$$\beta = -\frac{1}{\omega\sqrt{LC}} \tag{2.2}$$

The characteristic impedance Z_c

$$Z_c = \sqrt{\frac{Z}{Y}} = \sqrt{\frac{L_L}{C_L}} \tag{2.3}$$

The phase velocity V_p

$$v_p = \frac{\omega}{\beta} = -\omega^2\sqrt{L_L C_L} \tag{2.4}$$

The group velocity V_g

$$v_g = \frac{\partial\omega}{\partial\beta} = \omega^2\sqrt{L_L C_L} \tag{2.5}$$

The dimensions of L_L and C_L are values per meter. Compared equation (2.4) and (2.5), the phase and group velocities are antiparallel. They have the same absolute value, but opposite in sign. The group velocity associates to the direction of the energy flow. Thus, the effect of this property is that the phase shifts backward to the energy flow.

In wave propagation along structures, other natural effects are caused by the associated currents and voltages. A series inductance L_R is presented by the current flow over C_L, and a shunt capacitance C_R is presented by the existing voltage between the upper conductors and the ground plane. Hence, considering the right-handed (L_R, C_R) contribution to the left-handed (L_L, C_L) reactance, the composite right/left-handed (CRLH) structure is introduced [8] [9]. The equivalent circuit of CRLH transmission line is in figure 2.2.

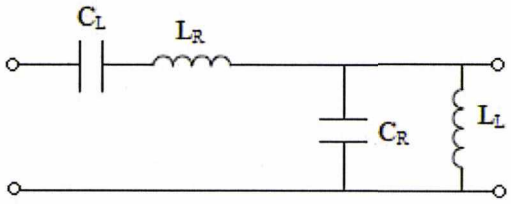

Figure 2.2. Equivalent circuit of CRLH transmission line

At low frequencies, L_R and C_R are short and open, so the equivalent circuit is simplified to be the left-handed (L_L, C_L) which has antiparallel phase and group velocities. Therefore, below a certain cut-off frequency, LH stopband is present. At high frequencies, L_L and C_L are short and open, so the equivalent circuit is the right-handed (L_R, C_R), in which phase and group velocities are parallel. Therefore, above a certain cut-off frequency, RH stopband is present. If four elements L_R, C_R, L_L, and C_L all contribute to the transmission characteristic, then it is called CRLH.

2.1 CRLH transmission line characteristics

Figure 2.3 shows the dispersion figure of a CRLH line [1]. The figure also includes pure LH, RH and "balanced" CRLH dispersion curves

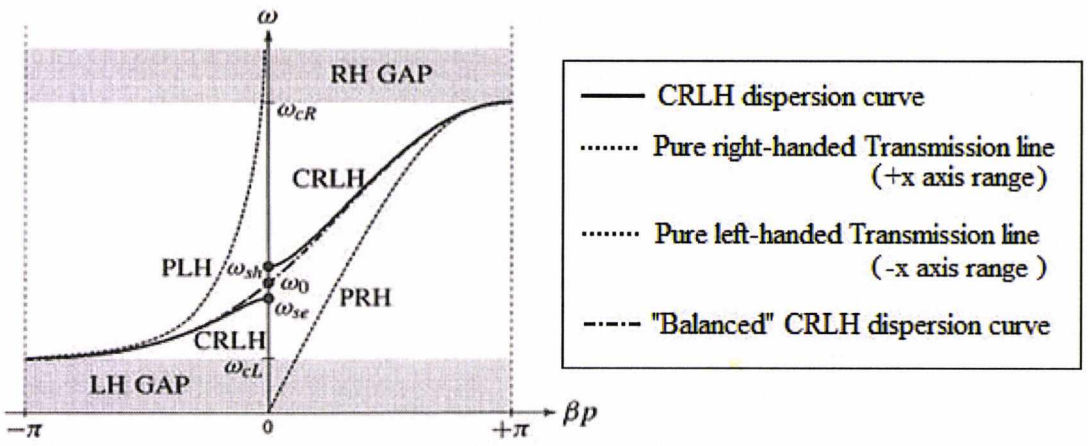

Figure 2.3. Theoretical dispersion figure of a CRLH line in [1]

In this figure, the CRLH transmission line propagates between the LH and RH gap. The left-handed propagation starts at ω_{cL} and stops at the resonance frequency ω_{se}; then, the right-handed propagation starts at the resonance frequency ω_{sh} and stops at ω_{cR}. In the dispersion, -π~0 is the LH range that contains pure left-handed (PLH) curve. Z_L is the PLH impedance.

$$Z_L = \sqrt{\frac{L_L}{C_L}} \tag{2.6}$$

and 0~π is the RH range that has pure right-handed (PRH) curve. Z_R is the PRH impedance.

$$Z_R = \sqrt{\frac{L_R}{C_R}} \tag{2.7}$$

A CRLH structure has a LH range and a RH range, but the dispersion curve in each range is different from that of PLH and PRH curves. That is caused by the combined effects of LH and RH contributions at all frequencies.

Referred to the figure 2.3, the resonance frequency of series components is ω_{se}

$$\omega_{se} = \frac{1}{\sqrt{L_R C_L}}\ rad/s \tag{2.8}$$

The resonance frequency of shunt components is ω_{sh}

$$\omega_{sh} = \frac{1}{\sqrt{L_L C_R}}\ rad/s \tag{2.9}$$

Normally, if these two resonances are different, there is a gap between the LH and RH ranges, which is called "unbalanced". The CRLH has two curves in both ranges. However, if two resonances are equal, which is called "balanced", the gap disappears. The CRLH will become a continuous curve and cross the Y axis at the transition frequency ω_0 (referred to figure 2.3). At this frequency, the phase constant β is zero and the propagation has an infinite-wavelength. In this particular case, $\omega_{se} = \omega_{sh}$ is equivalent to

$$L_R C_L = L_L C_R \tag{2.10}$$

or equivalent to

$$Z_L = Z_R \tag{2.11}$$

The guided wavelength for the CRLH transmission line is

$$\lambda_g = \frac{2\pi}{|\beta|} = \frac{2\pi}{\left|\frac{\omega}{\omega_R} - \frac{\omega_L}{\omega}\right|} \tag{2.12}$$

Where ω is the operating frequency and two variables are

$$\omega_R = \frac{1}{\sqrt{L_R C_R}}, \omega_L = \frac{1}{\sqrt{L_L C_L}} \tag{2.13}$$

This equation suits for the unbalanced and balanced case. At low frequency, λ_g is small. As the frequency increases, λ_g increases. At the transition frequency ω_0, $\lambda_g = \infty$, which means the electrical length of the line is zero, $\theta = l/\lambda_g = 0$. When the frequency increases to the RH range, λ_g starts to decrease.

There are numbers of advantages under the balanced case in CRLH transmission line, such as the constant frequency independent characteristic impedance, no stop band and broad bandwidth, nonzero group velocity and zero phase shift at the transition frequency, etc.

The applications of metamaterials are widely covered in many areas, such as antenna systems [10-13], coupler systems [14-16], filter systems [17], resonators [18] [19], etc. Furthermore, the research for the waveguide to obtain the left-handed characters has been proposed [20] [21]. Particularly, under the balanced case, the phase constant is zero and not related to the physical length of the structure.

Referred to figure 1.1, we see that for a given phase shift and therefore wavelength, the LH region occurs at a much reduced frequency and thus provides a reduced size for any device that is dependent on wavelength. A waveguide miniaturization by the propagation below cut-off frequency is shown in [22].

In this chapter, we will introduce two types of novel metamaterials models, then simulated and measured results are presented.

2.2 Designs of the shielded stripline CRLH transmission lines

The host line of our designs is the shielded stripline. The stripline is a purely TEM line as well as being completely shielded and the model becomes easy to analyse [23]. Since stripline is TEM, the geometry and equivalent circuit of the shielded stripline is shown in figure 2.4.

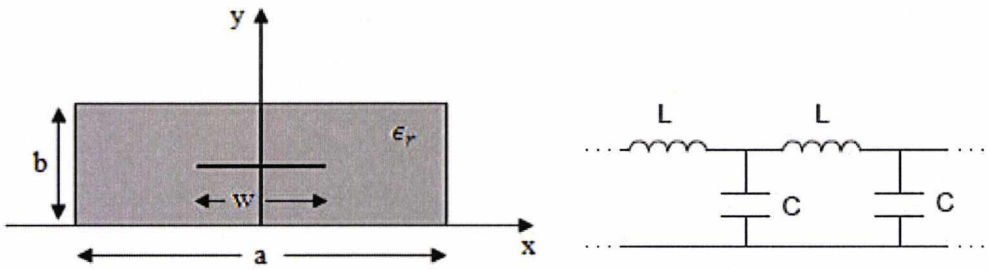

Figure 2.4. Geometry of the shielded stripline and equivalent circuit

The stripline consists of the series inductors and shunt capacitors. The characteristic impedance of the shielded stripline is determined by the capacitance and inductance per unit length of the stripline.

$$Z_0 = \sqrt{\frac{L}{C}} = \frac{1}{V_p C} = \frac{\sqrt{\epsilon_r}}{cC} \tag{2.14}$$

Where L and C are the inductance and capacitance per unit length of the stripline, c is the speed of light in the free space, and ϵ_r is the dielectric constant of the substrate material.

It is well known that the capacitance per unit length C is determined by the values of a, b and w in the shielded stripline. Therefore, in our design, the dimensions of a, b and w are chosen to make the Z_0 equal to 50Ω.

The purpose of our design is to build periodic structures, which contain small electrical scatterers to obtain the left-handed characteristics at lower frequency. There are two types of unit cell designed in this chapter, one is called "planar" and another is "via".

Figure 2.5 shows the geometries of the unit cells and the equivalent circuit.

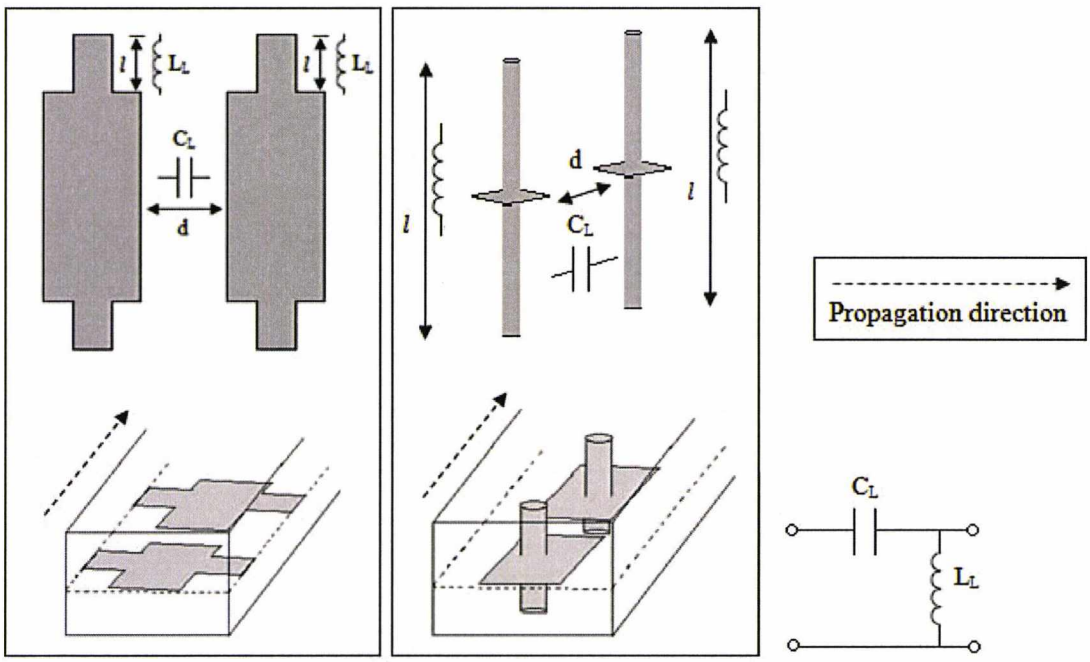

(a) (b) (c)

Figure 2.5 Geometries of unit cells and equivalent circuit. (a) planar type, (b) via type, (c) equivalent circuit.

In the figure, the dash line plane is the middle layer of the model and the dash arrow points to the propagation direction. As we can see that the gap between two discontinuities will perform as a series capacitor C_L. For the planar type, the slim metal in each discontinuity which connects to the side wall of the host line will perform as a shunt inductor L_L. For the via type, the metallise vias can be considered as the shunt inductors L_L.

By embedding the circuit elements of inclusions, the original stripline will become the conventional transmission line with series capacitors and shunt inductors. Therefore, the equivalent circuit is complicated and the model of one unit cell is shown in figure 2.6.

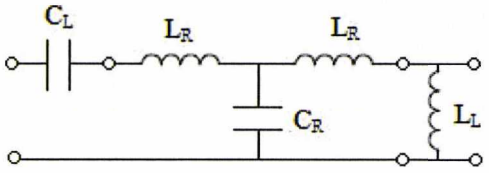

Figure 2.6 Equivalent circuit of CRLH stripline

2.2.1 The transmission (ABCD) matrix analysis

The transmission matrix formalism provides a convenient method to describe the characteristics of two or more two-port networks [23]. Before the simulations, the ABCD matrix analysis can approximately present the affects of all elements in the equivalent circuit.

The characteristics of the waveguide parameters such as Z, Y and S can be represented by applying the matrix method. In an N-port microwave network, once the voltages and currents have been defined at various points, the impedance matrices of circuit theory can be used to quantify the reactance. Then the matrix description of the network can be determined. The impedance matrix (Z) of the N-port microwave network relates voltages and currents in matrix form as

$$[V] = [Z][I] \tag{2.15}$$

The parameters of a two-port network can be defined by a 2 × 2 or ABCD matrix (figure 2.7) [23]. The total voltages and currents can be written as:

$$V_1 = AV_2 + BI_2 \tag{2.16}$$

$$I_1 = CV_2 + DI_2 \tag{2.17}$$

Or in matrix form as:

$$\begin{bmatrix} V_1 \\ I_1 \end{bmatrix} = \begin{bmatrix} A & B \\ C & D \end{bmatrix} \begin{bmatrix} V_2 \\ I_2 \end{bmatrix} \tag{2.18}$$

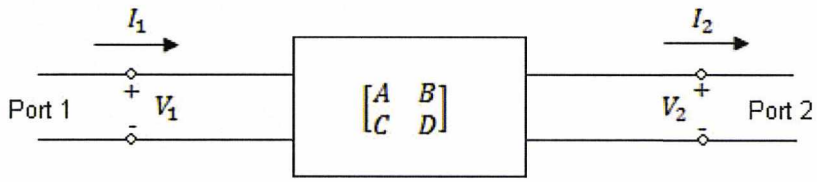

Figure 2.7. A two-port network

For the cascade connection of two-port networks (figure 2.8) [23], the individual matrix expressions are:

$$\begin{bmatrix} V_1 \\ I_1 \end{bmatrix} = \begin{bmatrix} A_1 & B_1 \\ C_1 & D_1 \end{bmatrix} \begin{bmatrix} V_2 \\ I_2 \end{bmatrix} \tag{2.19}$$

$$\begin{bmatrix} V_2 \\ I_2 \end{bmatrix} = \begin{bmatrix} A_2 & B_2 \\ C_2 & D_2 \end{bmatrix} \begin{bmatrix} V_3 \\ I_3 \end{bmatrix} \tag{2.20}$$

To get the total ABCD matrix of the cascade connection of two-port networks, we can substitute these two matrices.

$$\begin{bmatrix} V_1 \\ I_1 \end{bmatrix} = \begin{bmatrix} A_1 & B_1 \\ C_1 & D_1 \end{bmatrix} \begin{bmatrix} A_2 & B_2 \\ C_2 & D_2 \end{bmatrix} \begin{bmatrix} V_3 \\ I_3 \end{bmatrix} \tag{2.21}$$

The order of the multiplication of the matrix must be the same as the order of the arranged networks.

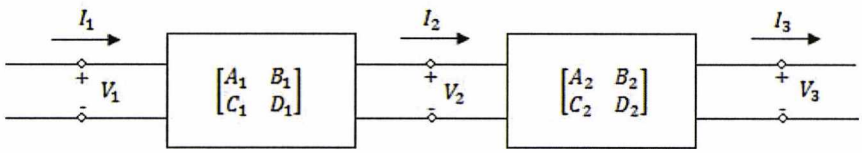

Figure 2.8. The cascade connection of two-port networks

The purpose of using this method is to define the change of phase constant β with the frequency. As long as we get the $\beta - \omega$ figure, we could compare it with the dispersion figure of the composite right/left-handed transmission line.

The equivalent circuit of our design (figure 2.9) can be considered as a cascade connection of two-port networks. We could assume three two-port networks consist of one unit cell. If the ABCD matrix of each individual network can be formed, the multiplication of all the matrices will be the total parameter expression. The parameters of each part can be easily found in the text book [23].

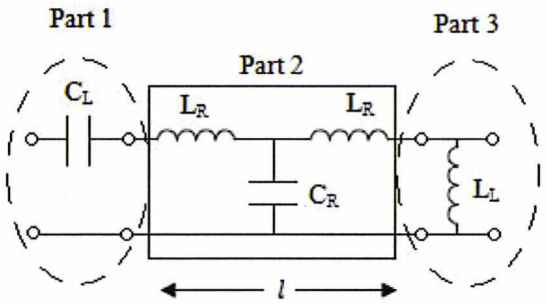

Figure 2.9. Three two-port networks of our design

The circuit of part 1 is a series capacitor, which can be considered as a series component in the circuit (figure 2.10).

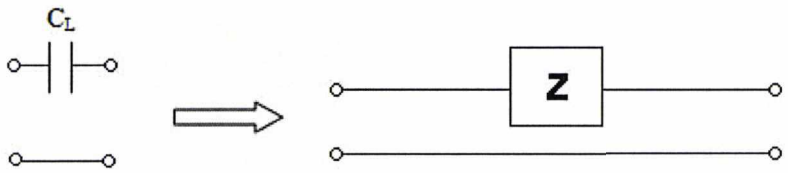

Figure 2.10. A series component circuit

And its ABCD parameters are:

$$A = 1; B = Z; C = 0; D = 1 \tag{2.22}$$

Transferring the capacitance C_L to the impedance expression, it is:

$$B = Z = \frac{1}{j\omega C_L} \tag{2.23}$$

So the ABCD matrix will be:

$$\begin{bmatrix} A_1 & B_1 \\ C_1 & D_1 \end{bmatrix} = \begin{bmatrix} 1 & \frac{1}{j\omega C_L} \\ 0 & 1 \end{bmatrix} \tag{2.24}$$

Part 2 is a small length of traditional transmission line with the impedance Z_0 and phase constant β_0, and its circuit can be simplified in figure 2.11.

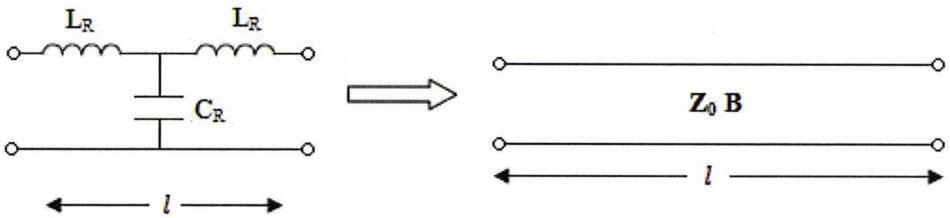

Figure 2.11. Conventional transmission line circuit

The ABCD parameters are:

$$A = \cos\beta_0 l\,, B = jZ_0 \sin\beta_0 l\,, C = jY_0 \sin\beta_0 l\,, D = \cos\beta_0 l \tag{2.25}$$

In the parameters, l is the length of the transmission line.

So the ABCD matrix will be:

$$\begin{bmatrix} A_2 & B_2 \\ C_2 & D_2 \end{bmatrix} = \begin{bmatrix} \cos\beta_0 l & jZ_0 \sin\beta_0 l \\ jY_0 \sin\beta_0 l & \cos\beta_0 l \end{bmatrix} \tag{2.26}$$

The phase constant β_0 of the transmission line is:

$$\beta_0 = \frac{\omega}{V_p} \tag{2.27}$$

Where V_p is the phase velocity. Because the host line we use is the stripline, so in TEM mode, $V_p = \frac{c}{\sqrt{\epsilon_r}}$. Here, ε_r is the relative permittivity of the stripline material. So:

$$\beta_0 = \frac{\omega}{V_p} = \frac{\omega\sqrt{\epsilon_r}}{c} \tag{2.28}$$

Part 3 is a shunt inductor, and figure 2.12 shows the circuit with a shunt component.

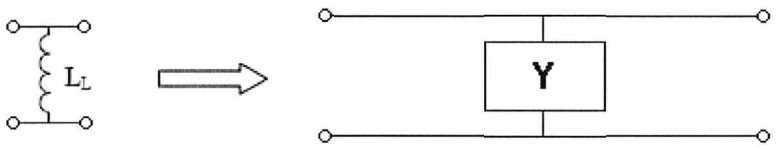

Figure 2.12. A shunt component circut

The ABCD parameters for this circuit are:

$$A = 1, B = 0, C = Y, D = 1 \tag{2.29}$$

Y is the inductance value L_L, and transferring the inductance to the impedance expression is:

$$C = Y = \frac{1}{j\omega L_L} \tag{2.30}$$

So the ABCD matrix will be:

$$\begin{bmatrix} A_3 & B_3 \\ C_3 & D_3 \end{bmatrix} = \begin{bmatrix} 1 & 0 \\ \frac{1}{j\omega L_L} & 1 \end{bmatrix} \tag{2.31}$$

Now, all parameters of three two-port networks have been settled. If we say matrix X is the final multiplication of these three matrices. So

$$X = \begin{bmatrix} A & B \\ C & D \end{bmatrix} = \begin{bmatrix} A_1 & B_1 \\ C_1 & D_1 \end{bmatrix}\begin{bmatrix} A_2 & B_2 \\ C_2 & D_2 \end{bmatrix}\begin{bmatrix} A_3 & B_3 \\ C_3 & D_3 \end{bmatrix}$$

$$= \begin{bmatrix} 1 & \frac{1}{j\omega C_L} \\ 0 & 1 \end{bmatrix}\begin{bmatrix} \cos\beta_0 l & jZ_0 \sin\beta_0 l \\ jY_0 \sin\beta_0 l & \cos\beta_0 l \end{bmatrix}\begin{bmatrix} 1 & 0 \\ \frac{1}{j\omega L_L} & 1 \end{bmatrix} \tag{2.32}$$

Our structure consists of symmetrical periodic unit cells along the transmission line and it can be considered as the composition of the cascade connection of two-port networks. Through the analysis of the infinite periodic structures, we could use the ABCD matrix to define the voltages and currents on each side of the multiple unit cells [23].

$$\begin{bmatrix} V_n \\ I_n \end{bmatrix} = \begin{bmatrix} A & B \\ C & D \end{bmatrix} \begin{bmatrix} V_{n+1} \\ I_{n+1} \end{bmatrix} \tag{2.33}$$

We define the length of each unit cell is d, so the propagation factor is $e^{-\gamma d}$.

$$V_{n+1} = V_n e^{-\gamma d}, I_{n+1} = I_n e^{-\gamma d} \tag{2.34}$$

Comparing (2.33) with (2.34) gives

$$e^{\gamma d} = \frac{(A+D) \pm \sqrt{(A+D)^2 - 4}}{2} \tag{2.35}$$

$\gamma = \alpha + j\beta$. For symmetrical networks, if we only consider the lossless case, the attenuation constant α is zero in the passband. So the formula could be transferred as:

$$j\beta = \frac{1}{d} \ln\left(\frac{(A+D) \pm \sqrt{(A+D)^2 - 4}}{2} \right) \tag{2.36}$$

Now for our structure, we already have the ABCD matrix X of one unit cell.

$$X = \begin{bmatrix} A & B \\ C & D \end{bmatrix} = \begin{bmatrix} 1 & \frac{1}{j\omega C_L} \\ 0 & 1 \end{bmatrix} \begin{bmatrix} \cos\beta_0 l & jZ_0 \sin\beta_0 l \\ jY_0 \sin\beta_0 l & \cos\beta_0 l \end{bmatrix} \begin{bmatrix} 1 & 0 \\ \frac{1}{j\omega L_L} & 1 \end{bmatrix} \tag{2.37}$$

Now in the equation for X, if the transmission line has a certain length l and Z_0=50Ω, there are only two variables C_L and L_L except frequency ω. By inputting the variables, an approximate phase constant value can be calculated. If X matrix can be solved to get value A, D, then the imaginary part of equation (2.36) can be plotted with ω. The $\beta - f$ plots are shown in figure 2.13 under "unbalanced" and "balanced" cases. The length l is 0.5mm, under "unbalanced" case, C_L=0.067pF, L_L=0.4nH and under "balanced" case, C_L=0.095pF, L_L=0.24nH.

This dispersion figure in figure 2.13 shows that our design could provide the left-handed propagation. That is because in $\beta < 0$ range, the phase velocity $V_p = \frac{\omega}{\beta} < 0$, and also the group velocity $V_g = \frac{\Delta\omega}{\Delta\beta} > 0$. Thus, we have the left-handed propagation.

In the unbalanced diagram, the left-handed region is from 14GHz to 23GHz, and the right-handed region starts at 38GHz. The stopband exists between them. The shape of this curve is exactly the same as the theoretical CRLH plot (figure 2.3) [1]. The input PLH impedance Z_L does not match with the PRH impedance Z_R.

By changing the value of L_L and C_L, the balanced condition can be achieved (figure 2.13b). The dispersion has the perfect continuous curve across the special $\beta = 0$ point.

This method can approximately locate the value ranges of series capacitance C_L and shunt inductance L_L before the actual structure design. However, the practical design will include other contributions which make the circuit more complex.

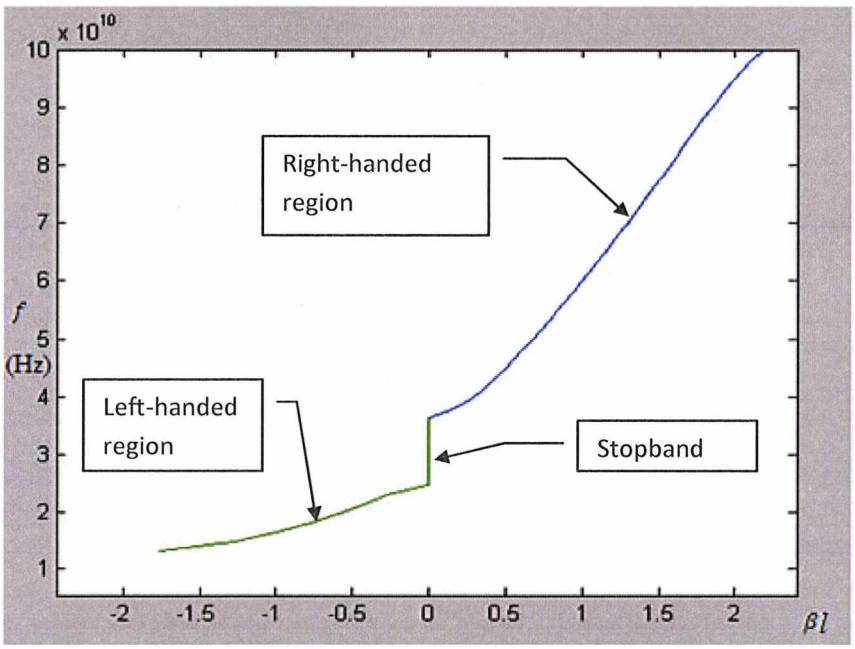

(a)

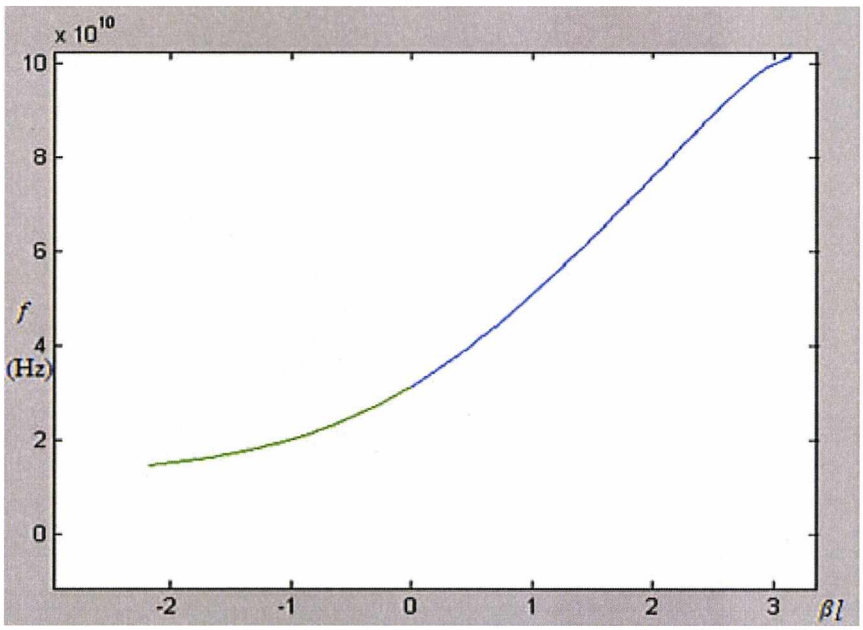

(b)

Figure 2.13. $\beta(rad) - f$ plots. (a) unbalanced case (C_L=0.067pF, L_L=0.4nH), (b) balanced case (C_L=0.095pF, L_L=0.24nH)

2.2.2 The calculations of series capacitance C_L and shunt inductance L_L

The values of the capacitance C_L and inductance L_L in the left-handed circuit part are very important in the design process of the structures. There is a method to calculate the approximate values in HFSS. We can simulate the single cell and plot the imaginary parts of Y/Z parameters. By dealing with the slopes of plots, the impedance L_L and C_L can be determined. Ansoft HFSS is the software we use to optimize and simulate the real project models. Most of the simulated results in this thesis are from this software.

Series capacitance C_L

The series capacitor C_L is formed by the gap with the length of d between each unit cell. To calculate the series components, Y parameter is straight forward. In HFSS, two pieces of

metallised planes are parallel set in the dielectric materials. Although the metallised planes will have shunt capacitance contributions, the capacitance values are quite small and the series capacitance C_L will dominate the transmission characteristic. A simple simulation can be set in HFSS.

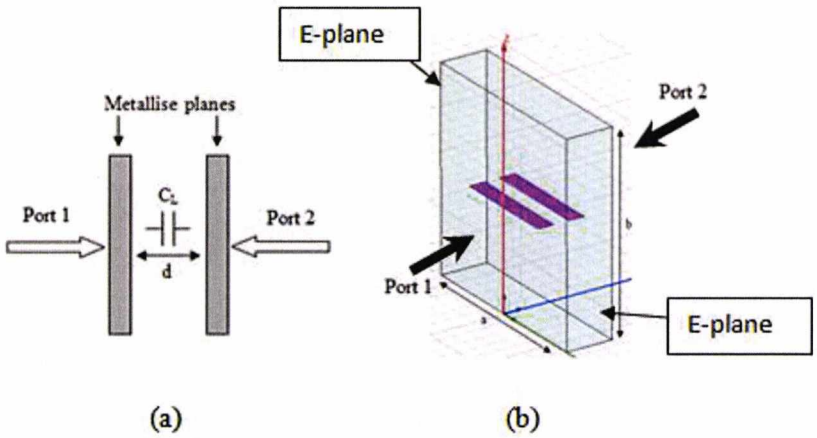

Figure 2.14. Models of (a) planar unit cell, (b) HFSS.

The figure (a) is the geometry of the model, and (b) is the practical model in HFSS. The E-plane boundary condition needs to be applied at the side walls. The top and bottom layers are perfect electric boundaries.

If we let d=0.5mm, the imaginary Y plot is shown in figure 2.15. In fact, there is no material dispersion. Therefore, the capacitance C_L calculated at lower frequencies can be assumed as the same value at higher frequencies.

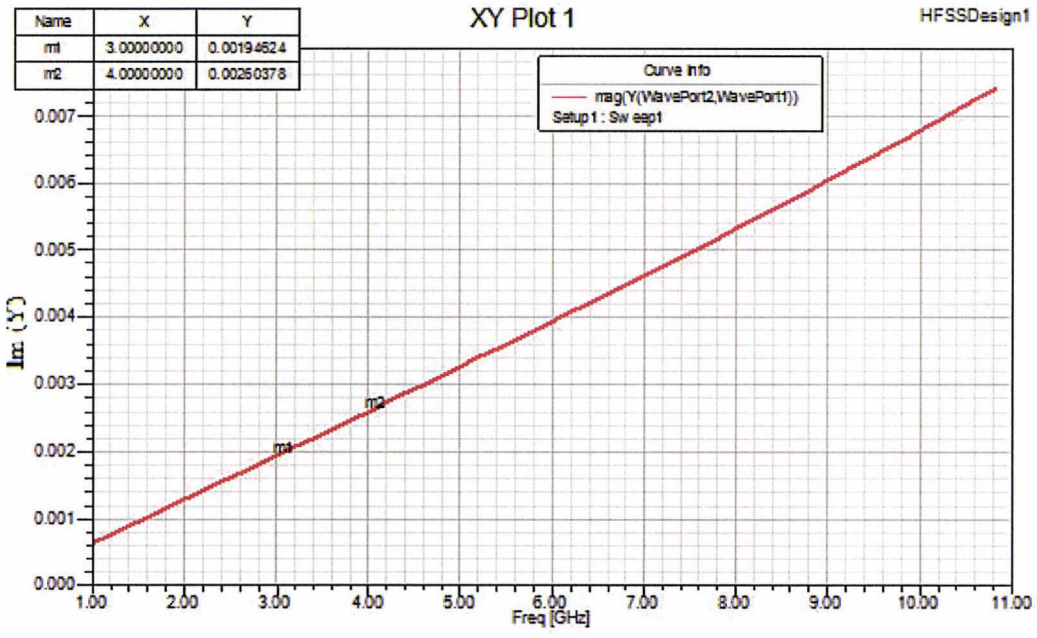

Figure 2.15. Imaginary Y parameters (d=0.5mm)

The magnitude of Y parameter is linear. The capacitance C_L is:

$$C_L = \frac{\Delta Y}{\Delta f}\frac{1}{2\pi} \tag{2.38}$$

The point m1 is at 3GHz, and m2 is at 4GHz. Δf = 1GHz. According to the Y values of these two point, ΔY = 0.00074. So the approximate value of the series capacitance is:

$$C_L = \frac{0.00074}{1e^9}\frac{1}{2\pi} \approx 0.12pF \tag{2.39}$$

The value of C_L is related to the gap d between two units. Figure 2.16 shows the plot of the series capacitance C_L varies with gap d. It is clear that the series capacitance decreases as the gap becomes larger.

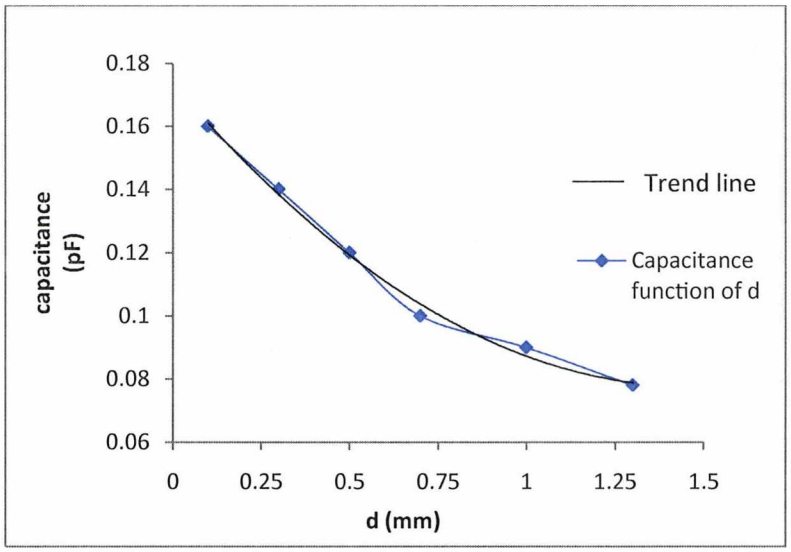

Figure 2.16. Series capacitances versus gap d

Shunt inductance L_L

In our design, the shunt inductor L_L with the length l is formed by the metal plane or post which is connected to the metallised wall of the structure. Figure 2.17 shows the geometries and HFSS model of two types.

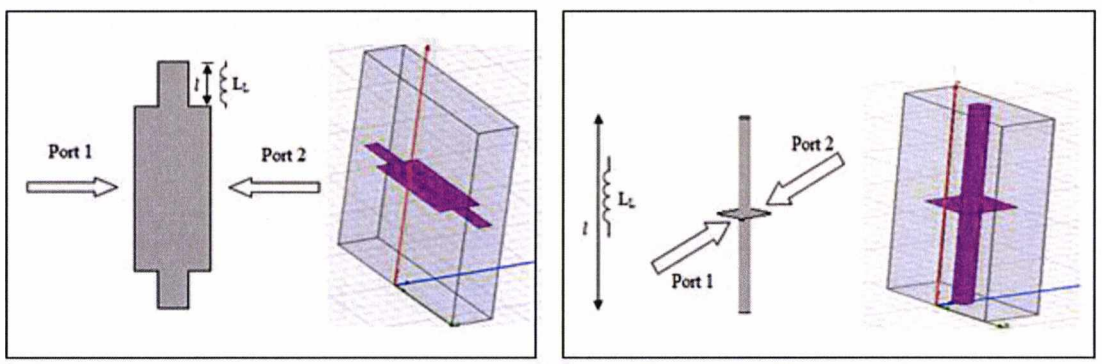

(a) (b)

Figure 2.17. Unit cell and HFSS simulation models of (a) planar type, (b) via type.

Although the metal plane along the signal transmission direction will create a series inductance, it has very little effect on the shunt inductance L_L. The length of l will determine the shunt inductance value.

The shunt inductance L_L can be calculated by the slope of the Z parameter plot. If we take the planar type as an example and let the l=1.4mm, figure 2.18 shows the Z-f diagram.

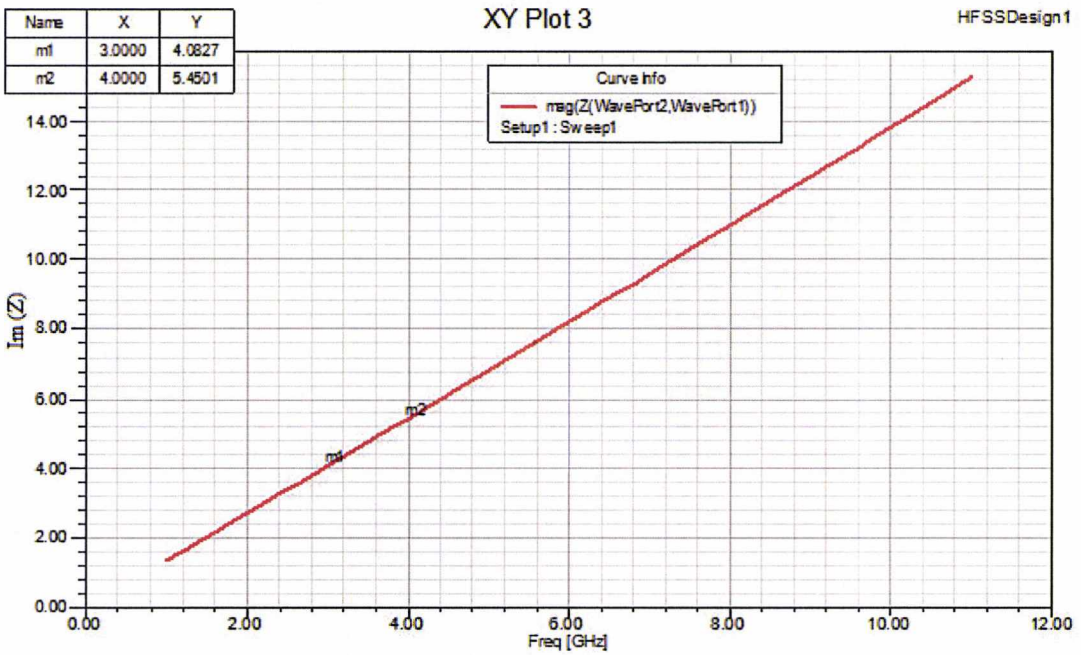

Figure 2.18. Imaginary Z parameters (l=1.4mm)

$$L_L = \frac{\Delta Z}{\Delta f}\frac{1}{2\pi} \tag{2.40}$$

The point m1 is at 3GHz, and m2 is at 4GHz. Δf = 1GHz. According to the Y values of these two point, ΔZ = 1.45. So the approximate value of the shunt inductance is:

$$L_L = \frac{1.45}{1e^9}\frac{1}{2\pi} \approx 0.23nH \tag{2.41}$$

The inductance value will increase if we make the metallic slot longer. The plot of the shunt inductance L_L varies with length l is shown in figure 2.19.

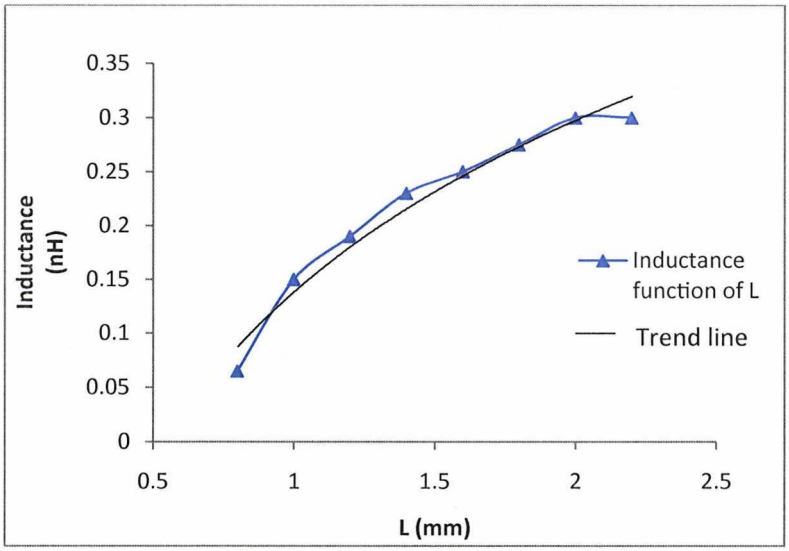

Figure 2.19. Shunt inductances versus length l

The left-handed elements L_L and C_L can be calculated with respect to the pure LH impedance $Z_L = \sqrt{L_L/C_L}$. The pure right-handed impedance $Z_R = \sqrt{L_R/C_R}$ is related to the characteristics impedance of stripline. The gap d and slot length l can be changed to have the proper Z_L. If we approach the balanced case of CRLH transmission line, the condition Z_R=Z_L needs to be satisfied.

2.3 Planar type CRLH transmission line design and fabrication

The first design is the planar type. We embedded the host stripline with ten unit cells periodically along the middle plane. The geometry of the HFSS model with ten unit cells and the dimensions of the structure are shown in figure 2.20.

In the structure, each port has the stripline as the host transmission line. Between these two striplines, there are series planar discontinuities in the middle plane. The gap between two discontinuities is very small, only 0.5mm, which is much less than $\lambda/4$. Each cell has a slim slot which connects to the side-wall. The boundary condition of the shielded stripline box is perfect electric conductor.

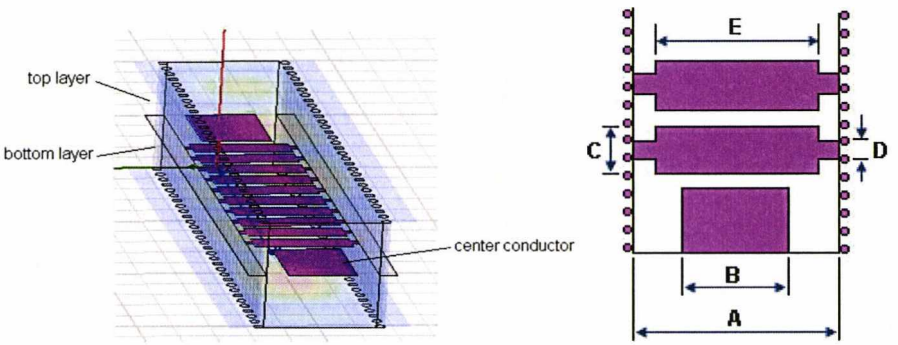

(a)

A	B	C	D	E
6.2	3.9	1.5	0.5	5.4

(b)

Figure 2.20. (a) HFSS model of ten unit cells, (b) dimensions of the structure.

The animation plots of magnetic field in the plane passing through the axis of the structure clearly show the propagation of the phase (figure 2.21). The energy keeps transmitting from port 1 to port 2. The phase change in the right-handed propagation part follows the same direction of the energy flow. However, because of the negative phase velocity during the left-handed transmission, the phase shifts to the opposite direction of the energy flow. That is the "backward-wave" [3]. The dash lines in figure 2.21 show the shift of the wave peak in a certain phase change period.

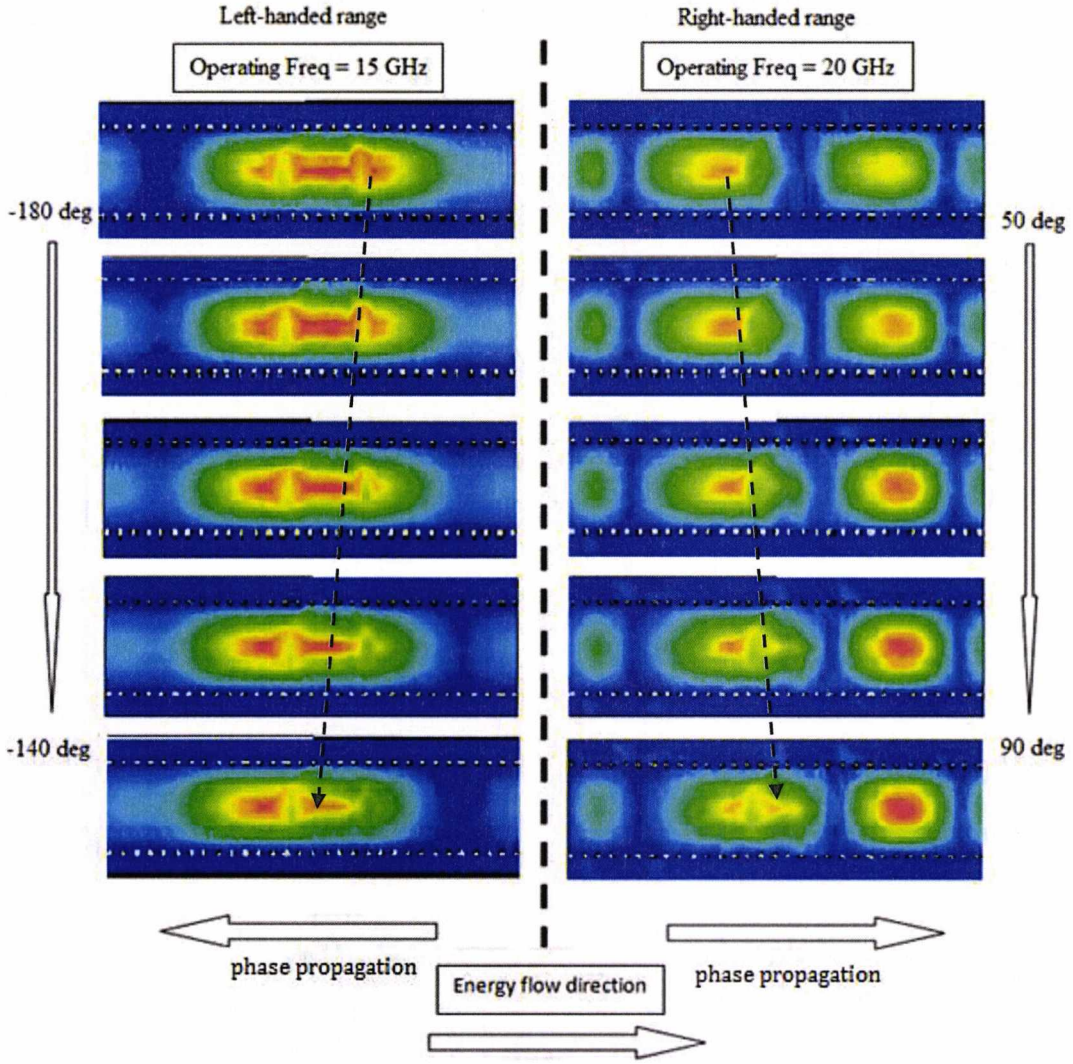

Figure 2.21. The animation plots of electronic field intensity at different frequencies

2.3.1 Phase constant dispersion figure and simulated results

The phase constant dispersion curve shows how the phase changes in degrees while the frequency increases. At the beginning of the design, we need to check the dispersion diagram to verify the left-handed propagation exist in our structures. Figure 2.22 shows the dispersion figure of one unit cell of the planar type.

The simulation is set in HFSS eigenmode while the periodic boundary condition has been applied to the unit. In this diagram, the dispersion curve has the same shape as the theoretical plot (figure 2.13), but it is the unbalanced case. The left-handed range is approximately from 14GHz to 15.7GHz. The stop band occurs around 16GHz. The left-handed part, as expected, has the negative phase velocity which is opposite to the group velocity. This proves that our structure is a CRLH transmission line.

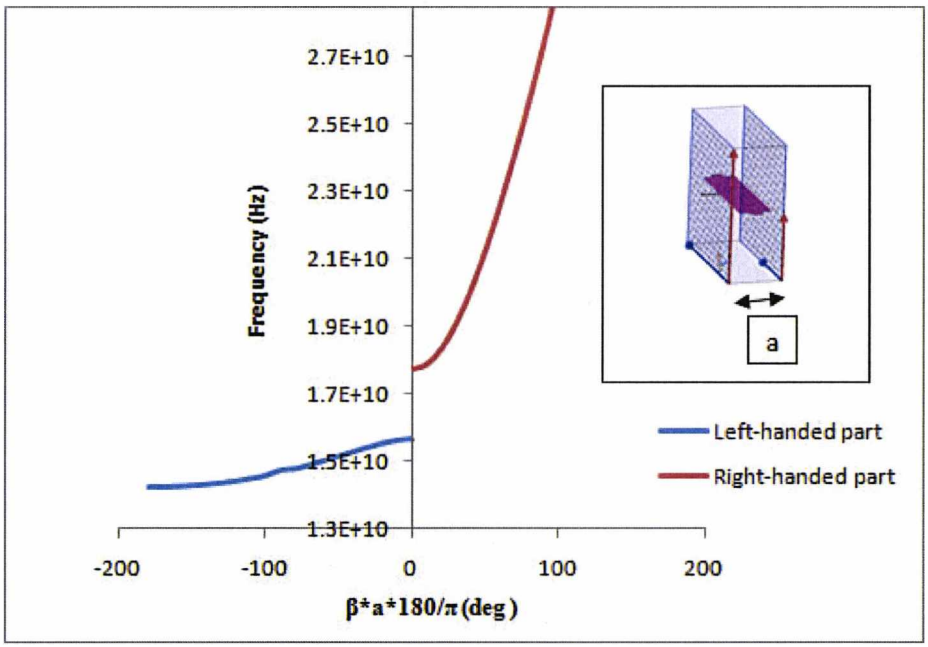

Figure 2.22. Dispersion curve of planar type CRLH line

Figure 2.23 shows the magnitudes of S parameters in HFSS. The blue line is S_{21}, and the red line is S_{11}. Both are presented in dB. A clear stop band is between these two kinds of propagations. Corresponded to the phase dispersion figure in figure 2.22, there is a left-handed propagation between 14.4GHz to 15.7GHz and the right-handed propagation starts at 17.9GHz. It is quite hard to locate ranges of the pass band and stop band precisely in S parameters. Because at the stop band of a structure with the length l, the attenuation constant α expresses in dB/m is $20\log_{10} e^{-\alpha l}$. Therefore, the slope of the curve is determined by the length of the structure. Thus, we defined ranges of pass and stop band from the theoretical dispersion plot in S parameters. In figure 2.23, the left-handed pass

band propagates well and reasonably matches with the dispersion curve. Unfortunately, the right-handed pass band S parameters are not good enough, that may because the transition does not match properly for this band.

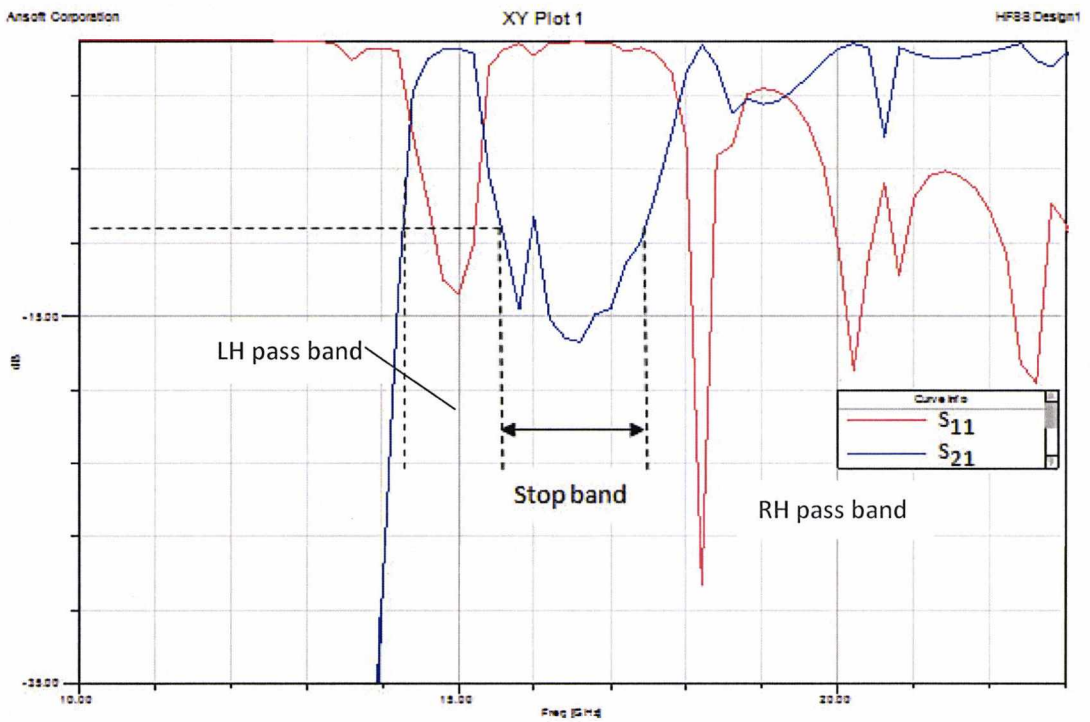

Figure 2.23. Simulated S parameters of planar type CRLH line

We could not achieve the balanced case, because the limit distance can be reached in the mechanical workshop. For instance, the gap of 0.5mm can only provide 0.12pF series capacitance, which much smaller than required to satisfy the balanced condition $Z_L = Z_R$.

2.3.2 Fabrication techniques

By using the conventional PCB fabrication methods, all the waveguides and the transmission lines can be manually made in the mechanical workshop. In this section, the series of vias method and the standard fabrication processes are introduced.

The traditional PCB board does not have the copper foil along the vertical direction. Thus, the conducting wall is not straight forward to manufacture. In microwave circuit design, the series of conducting vias along the wave propagation can be considered as the conducting walls of the guide. The distance between two vias must be much shorter than the wavelength. This technique is practical and the drilling machine can do the job perfectly in the workshop. The drilling machine in the mechanical workshop is LPKF Protomat C60 machine. Figure 2.24 shows the process how the vias consist of the conducting wall.

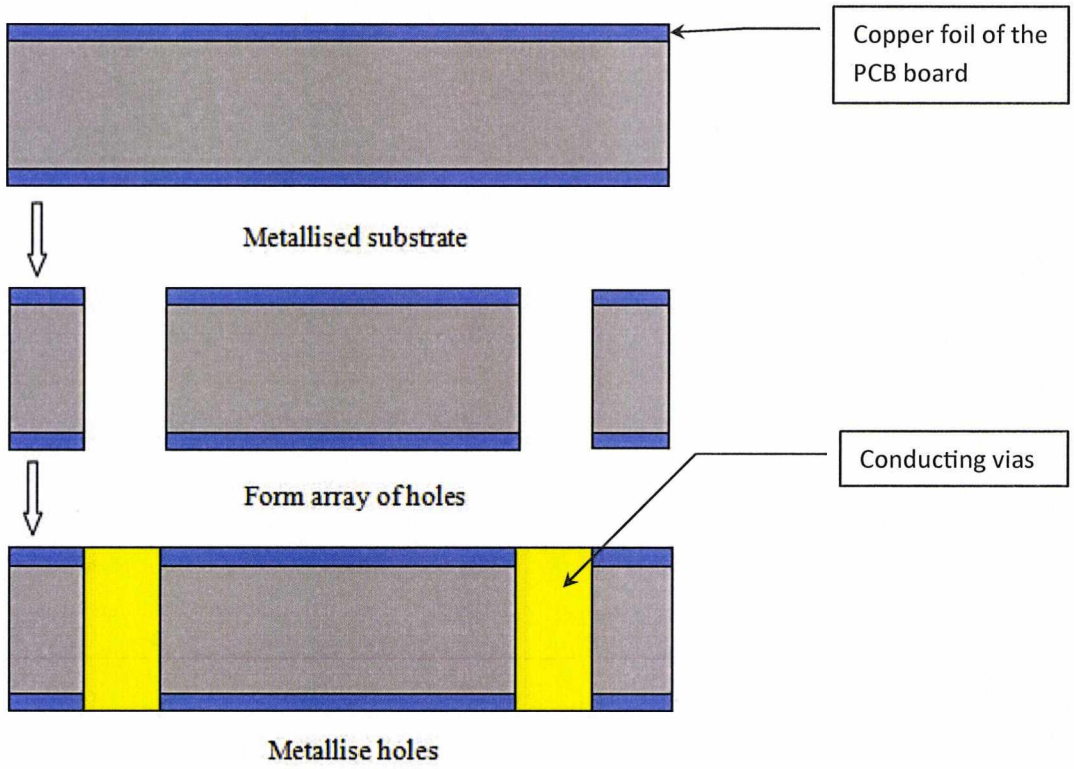

Figure 2.24. Procedures of conducting walls substituted by series of vias

In HFSS, the planar type of metamaterials line is set to be an example (figure 2.25). The two series of conducting vias consist of the two side walls. It is clear to see that these two series of vias are like the conducting walls and keep the energy mostly inside the guide.

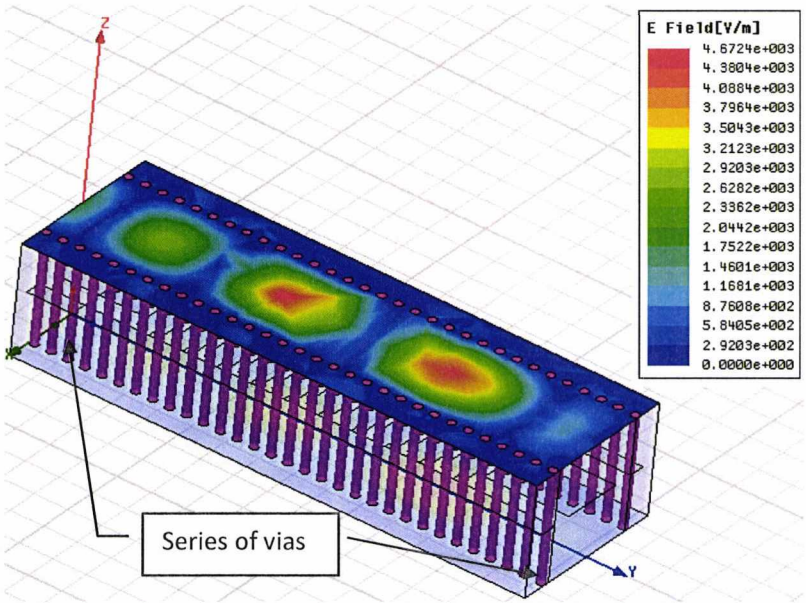

Figure 2.25 Simulated field plot where picket fence side walls substituted by series of vias

2.3.3 Standard PCB fabrication process

Our design is a two-layer structure. At the beginning, the masks for both layers need to be printed on the plastic film individually. The position of the holes on both layers must be corresponding to each other. The steps below show the process of one layer fabrication.

The PCB board needs to be cut in the approximate size by using the hand guillotine, and put into the drilling machine to drill the holes. After the drilling, the photo resistive laminated films apply to both sides of the board and then expose. After the exposure, the PCB board will be etched.

The host transmission line in our design is the stripline. Therefore, the SMA connecter has to be soldered on to the layer which has the middle circuit first. After soldering the SMA connecters on both ends, the two layers PCB boards are assembled with copper vias.

Rogers 5880 material is used to fabricate the waveguide. The relative permittivity of the substrate is 2.2 and the thickness is 3.175 mm. The total thickness of the structure which

consists of two dielectric layers is 6.35 mm. The diameter of the metal conducting vias is 0.5 mm, and the distance between vias is 1mm.

2.3.4 Measurements

The measurement is performed on the Anritsu 37397C vector network analyser with coaxial calibration. Compared with the simulated results, the insertion loss increased significantly to approximate 2-4dB. The dielectric and conductive loss are unavoidable. Also, during the fabrication, the loss may be greatly affected by the solder work and the gap that exists between layers and etc.

Figure 2.26 shows the measurement results. The frequency range of the left-handed transmission is from 14.2GHz to 15.5GHz, which is roughly matched with the simulated results. The right-handed part is from 18.9GHz to 21.5GHz, and the stop band range (S_{21} < -10dB) is about 3GHz. The insertion loss is less than 3dB for both parts.

The reflection line S_{11} is below -10dB at least in the two transmission regions. Both S parameters compares well to the simulated ones.

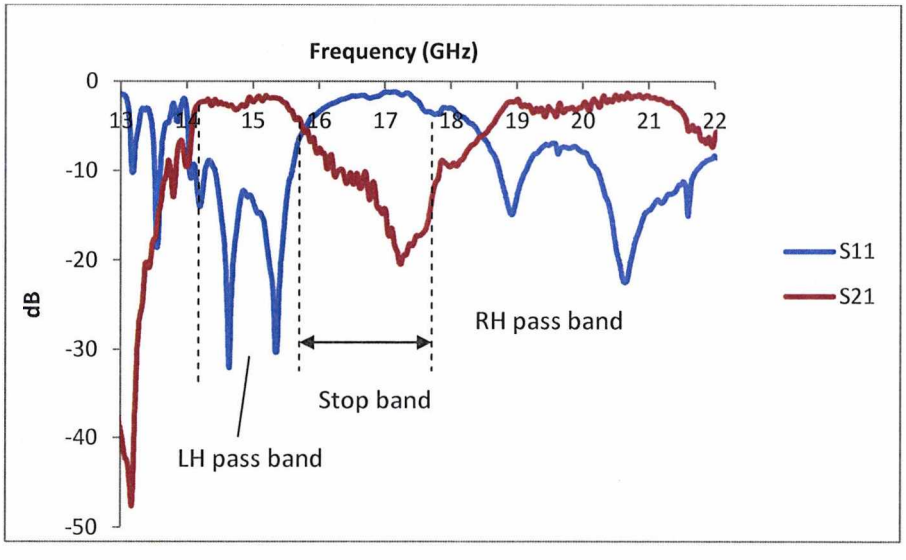

Figure 2.26. Measured results of planar type CRLH line

2.4 Via type CRLH transmission line design and fabrication

The via type CRLH transmission line is very similar to the first type, but using a via to connect the top and bottom metallisation. The geometry of ten unit cells model and dimensions of structure are shown in figure 2.27.

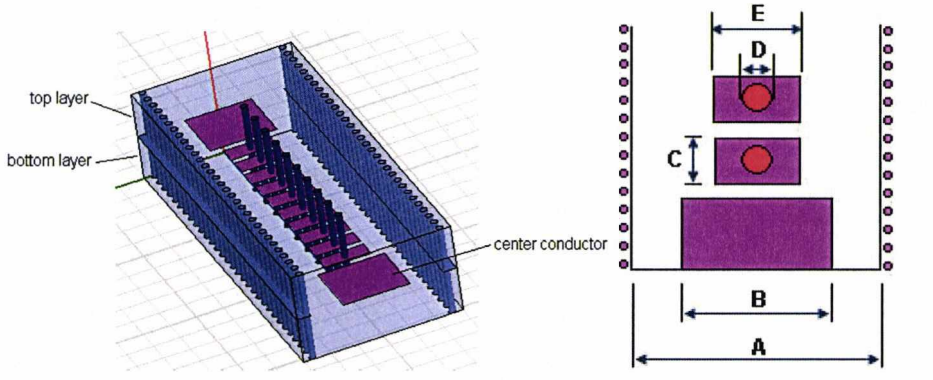

(a)

A	B	C	D	E
10	5	1.5	0.5	3.4

(b)

Figure 2.27. (a) HFSS model of ten unit cells, (b) dimensions of the structure.

In this design, the gaps between each discontinuity still form the series capacitors C_L and the distance between two unit cells still determines the series capacitance C_L. The metallised vias can be considered as the shunt inductors L_L. The height of the cylinder via will determine the value of L_L. The advantage of this type is that the vertical vias have little coupling with other components of the guide. However, due to the PCB fabrication technique, the height of via which relates to the shunt inductance L_L is difficult to change. Figure 2.28 shows the dominant mode in the via type CRLH line.

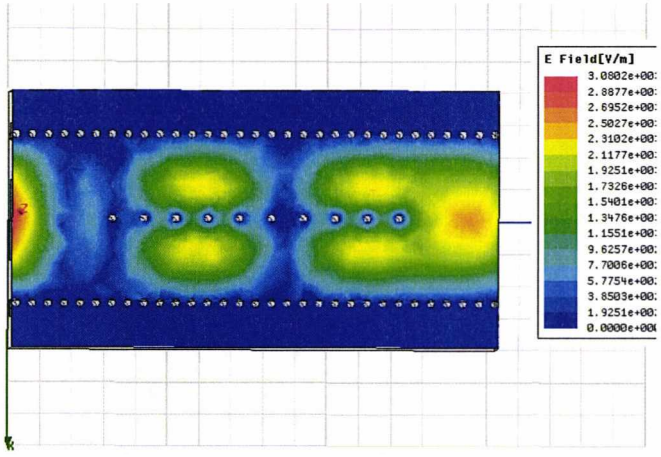

Figure 2.28. Dominant mode in the via type CRLH line

2.4.1 Phase constant dispersion figure

Figure 2.29 shows the dispersion figure of one unit cell of the via type CRLH line. As shown in the planar type, the metal vias can also support the left-handed propagation.

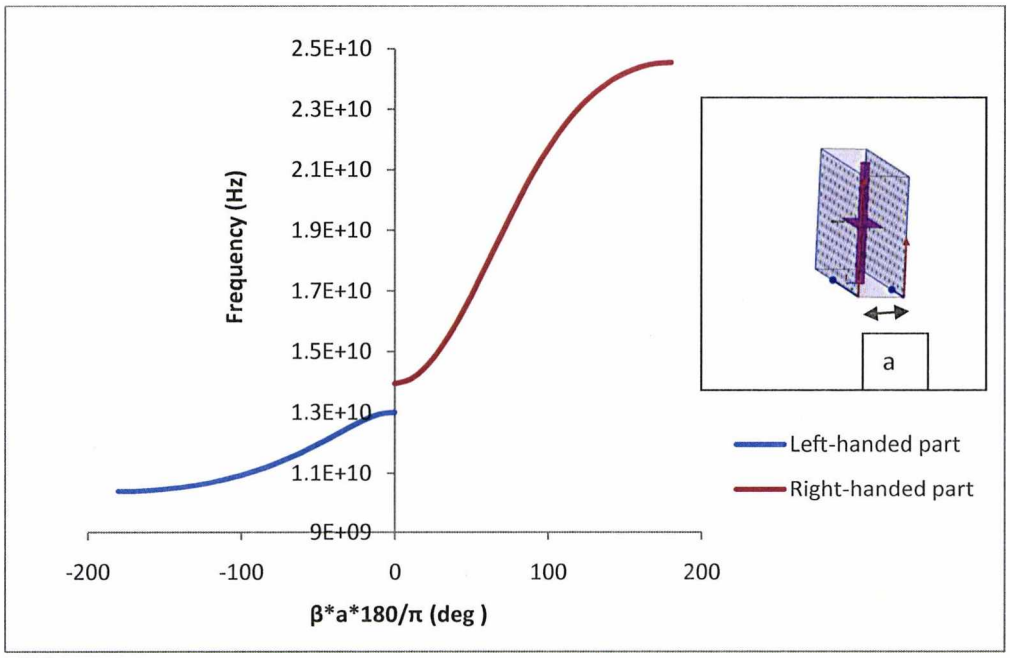

Figure 2.29. Dispersion curve of via type CRLH line

From the dispersion curve, the left-handed range is approximately from 10GHz to 13GHz, and the right-handed range starts at 14GHz. There is 1GHz stopband.

2.4.2 Simulated and measured results

Figure 2.30 shows the magnitudes of S parameters in HFSS. The blue line is S_{21}, and the red line is S_{11}. Compared with the planar type results, the left-handed region of the via type increases significantly. It is from 9.9GHz to 12.9GHz, which reaches 3GHz range. Compared with the dispersion curve, the left-handed ranges show good agreement.

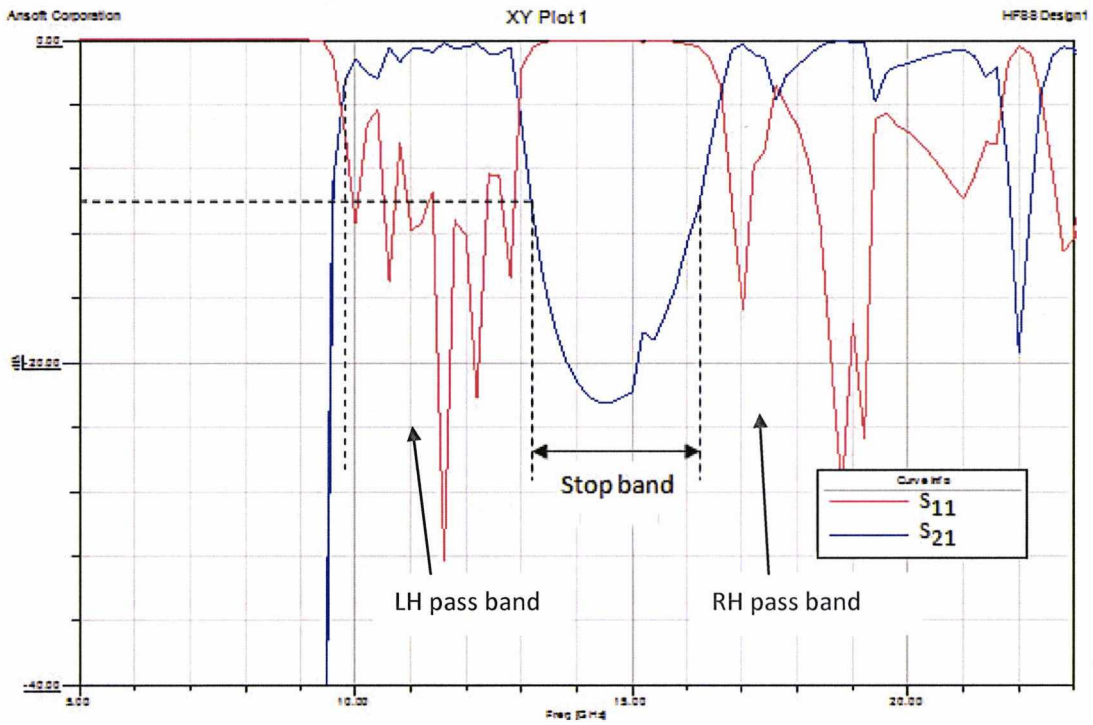

Figure 2.30. Simulated S parameters of via type CRLH line

Figure 2.31 is the measured results from the analyzer. Actually, the results are not as successful as simulated. The left-handed period only has a peak point at 14.5GHz; the insertion loss is very high as well. The main reason is attributed to the crude fabrication technique that was used and the complex structure. The vias in the center which forms the

shunt inductors are difficult to adjust accurately. During the assemble process, the vias are too easy to twist or move. The result may be much better if a professional fabrication process is applied.

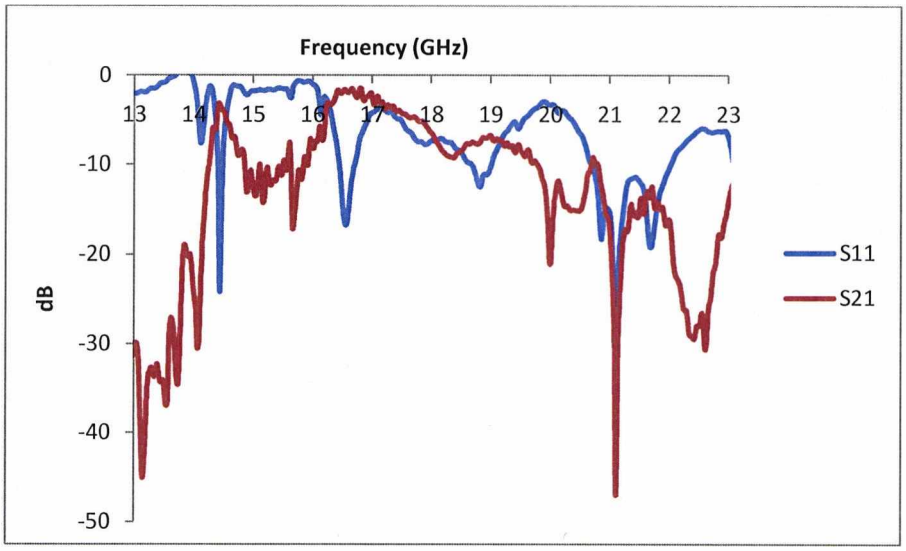

Figure 2.31. Measured results of via type CRLH line

A photograph of the fabricated structures is shown in figure 2.32.

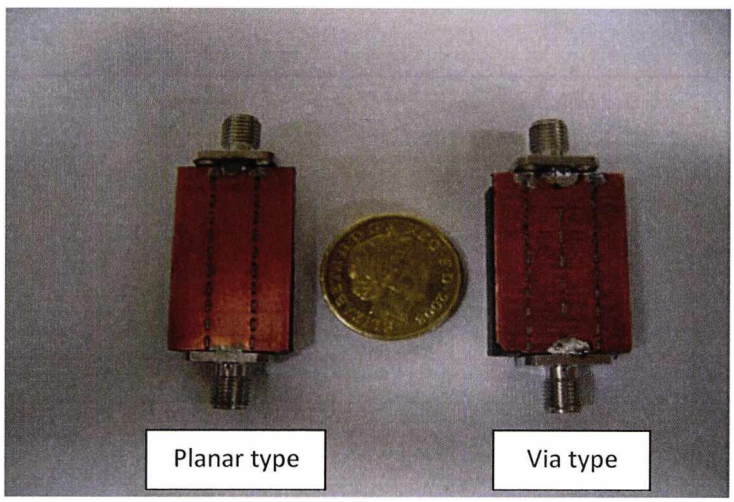

Figure 2.32. A photograph of the fabricated structures

2.5 Summary

In this chapter, a general introduction of metamaterials (MTMs) is given. The composite right/left-handed (CRLH) transmission line is presented, which is one of the most popular of MTMs with unusual properties, such as left-handed propagation, double negative parameters, negative phase velocity, backward-wave, etc. The dispersion curve of CRLH line is shown and the advantages of the special $\beta = 0$ point are introduced.

We used the transmission matrix analysis to approximately compute the equivalent circuit of the design and the dispersion curve of CRLH line is demonstrated. This method can be used to roughly determine the left-handed range by changing shunt inductance L_L and series capacitance C_L in the matrix. This is very important for the structure to reach the unbalanced case or balanced case. Then, the calculation through HFSS shows how the dimensions affect shunt inductance L_L and series capacitance C_L.

Two new types of CRLH transmission lines are presented - the planar type and via type. CRLH transmission is achieved in the host shield stripline is novel. All embedded electrical scatterers are shielded inside the stripline with the advantage of no radiation. By analysing the field distributions and dispersion curves, both lines have the significant left-handed range with backward-wave, negative phase velocity. Another advantage of our design is that the periodic units are very simple, unlike the interdigital slots on the metal surface [21].

Both CRLH lines have good simulated S parameters in the left-handed propagations, however, due to the crude fabrication technique and the complexity of the multi-layer assembling, the measured results have more insertion loss, especially in via type. A better fabrication environment can greatly improve the results.

This work has been presented at the third International Congress on Advanced Electromagnetic Materials in Microwaves and Optics – Metamaterials, London, 2009 [24].

References

[1] Christophe Caloz and Tatsuo Itoh, "*Electromagnetic Metamaterials*," Wiley Interscience, 2006.

[2] V.Veselago, "The electrodynamics of substances with simultaneously negative values of ε and μ," *Soviet Physics Uspekhi*, vol.10, no. 4, pp. 509-514, Feb. 1968.

[3] S. Ramo, J. R. Whinnery and T. Van Duzer, "*Fields and Waves in Communication Electronics*," Third Edition, John Wiley & Sons, 1994.

[4] A. K. Iyer and G. V. Eleftheriades, "Negative refractive index metamaterials supporting 2-D waves," *IEEE-MTT Int'l Symp.*, vol. 2, Seattle, WA, pp. 412-415, June 2002.

[5] A. A. Oliner, "A periodic-structure negative-refractive-index medium without resonant elements," *URSI Digest, IEEE-AP-S USNC/URSI National Radio Science Meeting*, San Antonio, TX, pp. 41, June 2002.

[6] C. Caloz and T.Itoh, "Application of the transmission line theory of left-handed (LH) materials to the realization of a microstrip LH transmission line," in *Proc. IEEE-AP-SUSNC/URSI National Radio Science Meeting,* vol. 2, San Antonio, TX, pp. 412-415, June 2002.

[7] C. Caloz and T.Itoh, "Transmission line approach of left-handed (LH) structures and microstrip realization of a low-loss broadband LH filter," *IEEE Trans. Antennas Propagat.*, vol. 52, no. 5, pp. 1159-1166, May 2004.

[8] C. Caloz and T.Itoh, "Novel microwave devices and structures based on the transmission line approach of meta-materials," in *IEEE-MTT Int'l Symp.*, vol. 1, Philadelphia, PA, pp. 195-198, June 2003.

[9] A. Sanada, C. Caloz and T.Itoh, "Characteristics of the composite right/left-handed transmission lines," *IEEE Microwave Wireless Compon. Lett.*, vol. 14, no. 2, pp. 68-70, Feb. 2004.

[10] C. Caloz and T.Itoh, "Array factor approach of leaky-wave antennas and application to 1D/2D composite right/left-handed (CRLH) structures," *IEEE Microwave Wireless Compon. Lett.*, vol. 14, no. 14, no. 6, pp. 274-276, June 2004.

[11] S. Lim, C. Caloz and T. Itoh, "Metamaterial-based electronically-controlled transmission line structure as a novel leaky-wave antenna with tunable radiation angle and beamwidth," *IEEE Trans. Microwave Theory Tech.*, vol. 53, no. 1, pp. 161-173, Nov. 2005.

[12] T. Ueda, N. Michishita, M. Akiyama, and T. Itoh, "Dielectricresonator- based CRLH transmission lines and their application to leaky wave antenna," *IEEE Trans. Microwave Theory Tech.*, vol. 56, no. I 0, pp. 2259-2268, Oct. 2008.

[13] R. Ziolkowski and A. Erentok, "Metamaterial-based efficient electrically small antennas," *IEEE Trans. Antennas Propag.*, vol. 54, no. 7, pp. 2113-2130, Jul. 2006.

[14] C. Caloz and T.Itoh, "A novel mixed conventional microstrip and composite right/left-handed backward-wave directional coupler with broadband and tight coupling characteristics," *IEEE Microwave Wireless Compon. Let.,* vol. 14, no. 1, pp. 31-33, Jan. 2004.

[15] C. Caloz, A. Sanada and T.Itoh, "A novel composite right/left-handed coupled-line directional coupler with arbitrary coupling level and broad bandwidth," *IEEE Trans. Microwave Theory Tech.*, vol. 52, no. 3, pp. 980-992, March 2004.

[16] Yuandan Dong and Itoh, T., "Application of composite right/left-handed half-mode substrate integrated waveguide to the design of a dual-band rat-race coupler," *IEEE MTT-S International Microwave Symposium Digest*, pp. 712-715, 2010

[17] C. Caloz and T.Itoh, "Transmission line approach of left-handed (LH) structures and microstrip realization of a low-loss broadband LH filter," *IEEE Trans. Antennas Propagat.*, vol. 52, no. 5, May 2004.

[18] A. Sanada, C. Caloz and T.Itoh, "Zeroth-order resonance in composite right/left-handed transmission line resonators," *Asia-Pacific Microwave Conference*, vol. 3, pp. 1588-1592, Seoul, Korea, Nov. 2003.

[19] G. Lubkowski, C. Damm, B. Bandlow, R. Schuhmann, "Broadband transmission below the cutoff frequency of a waveguide loaded with resonant scatterer arrays," *IET Proc. Microw. Antennas Propag.*, vol. 1, no. 1, pp. 165–169, 2007.

[20] I. Eshrah, A. Kishk, A. Yakovlev, and A. Glisson, "Rectangular waveguide with dielectric-filled corrugations supporting backward waves," *IEEE Trans. Microw. Theory Tech.*, vol. 53, no. 11, pp. 3298-3304, Nov. 2005.

[21] Y. Dong and T. Itoh, "Composite right/left-handed substrate integrated waveguide and half-mode substrate integrated waveguide," in *IEEE MTT-S Int. Microw. Symp. Dig.*, Boston, USA, pp. 49-52, 2009.

[22] Hrabar S., Bartolic J. and Sipus Z, "Waveguide miniaturization using uniaxial negative permeability metamaterial," *IEEE Trans. Antennas and Propag.*, vol. 53, no. 1, pp. 110-119, January 2005.

[23] David M. Pozar, "*Microwave Engineering*" third edition, John Wiley & Sons, Inc, ISBN 0-471-44878-8

[24] Ruo Feng Xu, P.R. Young, "Shield Stripline Left-Handed Transmission Lines," *3rd International Congress on Advanced Electromagnetic Materials in Microwaves and Optics, London*, August 2009.

3. Multilayer folded waveguides

In the microwave and millimetre-wave systems, rectangular waveguides (RWGs) have been well developed for many years. However, it is quite hard to integrate planar circuits with RWGs because of their three-dimensional nature. In recent years, some techniques have been developed to allow integration, such as the post wall waveguide [1], laminated waveguide [2], and substrate integrated waveguide (SIW) [3]. Compared with the RWGs, these new waveguides have the great advantage of easy integration with planar circuit, low cost and size reduction. SIW can be designed by using low temperature co-fired ceramics (LTCC) [4], microwave laminates [2] and photoimageable thick-films [5], which are the conventional microwave fabrication techniques. Based on the research on the characteristics of the SIW [6-8], lots of high performance devices have been demonstrated [9-12]. But at low frequency, the SIW is very wide. In order to reduce the transverse size of SIW and enhance the bandwidth, the folded substrate integrated waveguide (FSIW) has been proposed [13] [14] and applied for filters [15], antennas [16], couplers [17] etc.

In this chapter, the multi-layer substrate integrated folded waveguides are presented. The designs of transition and tapers are introduced. Then the narrowband waveguides are presented, which have applications on filters [18]. In the end, the multilayer folded waveguides are cut in the middle vertical, and each half part can support the half mode guided waves.

3.1 Two, three, four layers folded substrate integrated waveguides

The multiple layers folded waveguides have been widely applied in many fields, such as the folded waveguide filter, the antenna, the power divider, etc. There are two types of the folded waveguide. One is T type, which means the rectangular waveguide is folded from both ends to the centre. Another one is C type, which means the rectangular waveguide is folded from one end to another end. Both types can have the vary size reductions.

An example of two layers folded T type waveguide is shown in figure 3.1. Compared with the conventional waveguide, the typical folded guide has the half width $a/2$, but the double height $2b$. The design of the multiple layers folded waveguide need to consider the efficiency and the loss. Based on the design theory [19], the width of the waveguide, the height, and the width of the middle layer will have a direct affect on the bandwidth and the phase dispersion.

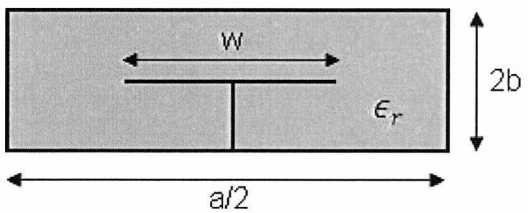

Figure 3.1. Geometry of two layers folded waveguide

The attenuation constant plots are shown in figure 3.2 [19]. The losses of the folded waveguide will increase as the number of layers increase. The conventional rectangular waveguide has the lowest loss compared with the multilayer folded waveguides. The four layers folded waveguide has the maximum width reduction; however, its loss is higher than others.

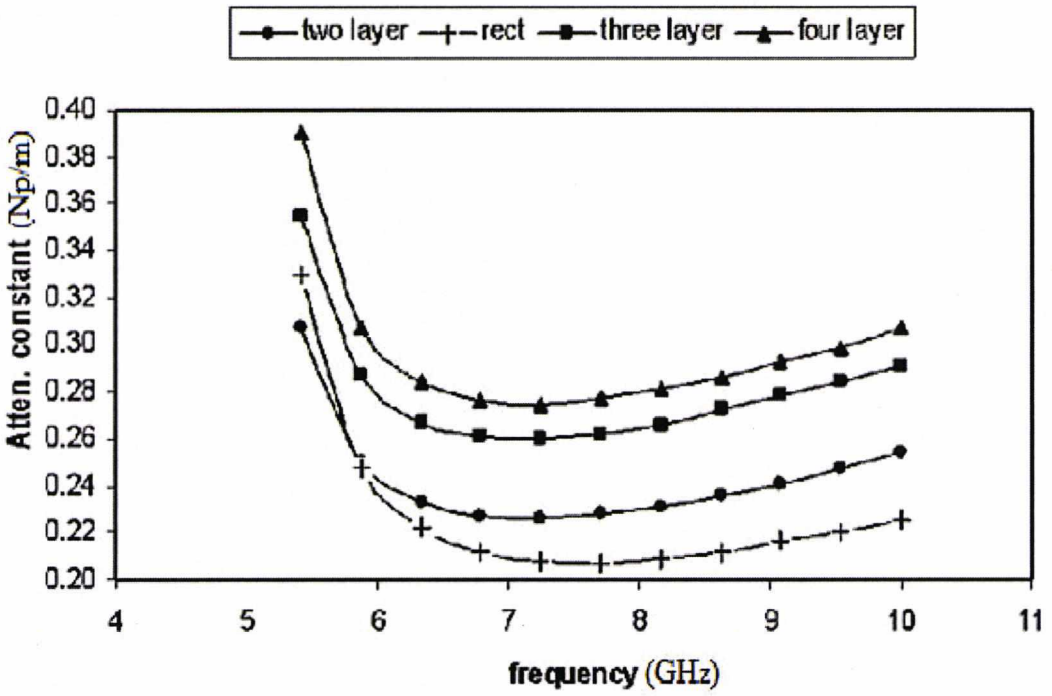

Figure 3.2. Attenuation constant plots in Rogers^{TM} Duroid ($\varepsilon_r = 2.2, \tan\delta = 0.0009$)

The geometries and dimensions of two, three and four layers folded waveguides are shown in figure 3.3.

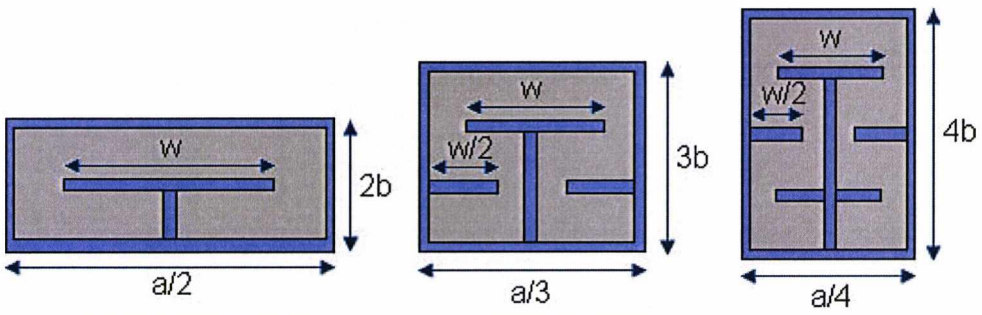

a/2	2b	w
15.48	1.27	3.06

a/3	3b	w
11.3265	1.905	4.6

a/4	4b	w
9	2.54	2.2

(a) (b) (c)

Figure 3.3. Geometries and dimensions of (a) two layers, (b) three layers, (c) four layers folded waveguide. (unit: mm)

3.2 The transition design for multilayer folded waveguides

3.2.1 Microstrip transmission line

The microstrip line has been chosen to be the transmission line to be transitioned to the folded waveguide. The main condition to choose the transition is that the field distribution needs to be similar to the folded waveguide. The electric field of the microstrip line has the maximum between the centre conductor and the ground plane (figure 3.4).

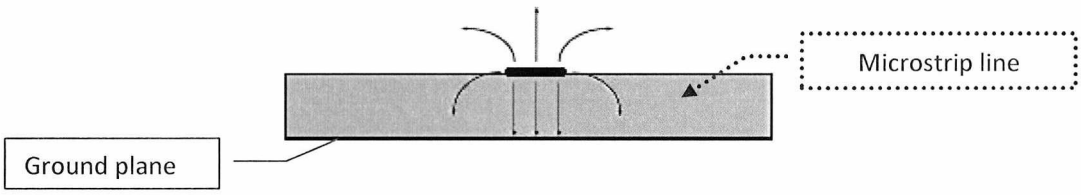

Figure 3.4. Microstrip line model

The electric field of the T type folded waveguide has the maximum between the top metallise layer and the first layer. Figure 3.5 shows the E-field plots of the fundamental mode in the folded waveguides. In each folded waveguide, the dominant region of the E-field matches with the microstrip's at the fundamental mode. The input impedance can be easily controlled by changing the width of the microstrip line. The required impedance is 50 ohm.

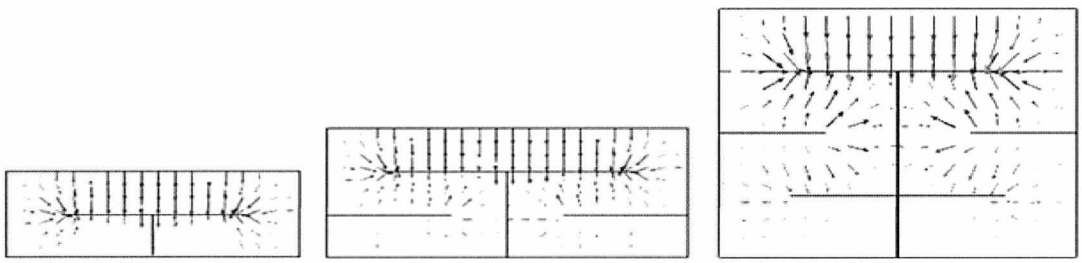

(a) (b) (c)

Figure 3.5. Fundamental E-field plots of (a) two layers, (b) three layers, (c) four layers folded waveguide.

3.2.2 Taper design

The taper is used to transform the 50 ohm impedance on the microstrip line to the impedance of the folded waveguide. It is also important in the matching of the magnetic field from the input line to the folded waveguide. Figure 3.6 shows the magnetic field matching by the taper.

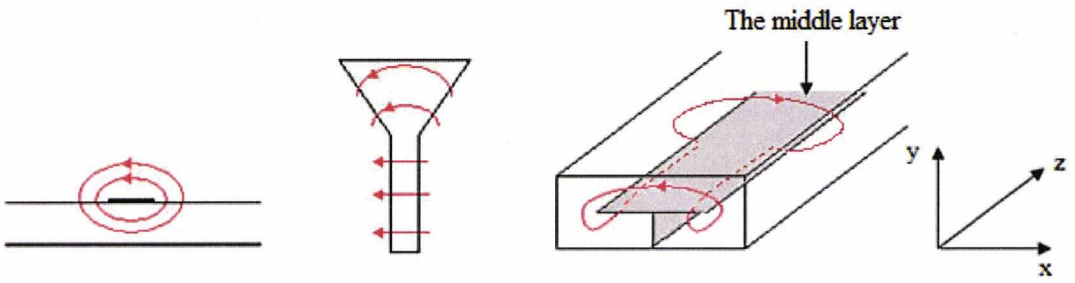

(a) (b) (c)

Figure 3.6. Magnetic field in (a) Microstrip line, (b) Taper, (c) Folded waveguide.

In this figure, the red line denotes the magnetic field flow. In the microstrip line (a), the H-field only has two components H_x and H_y. In the waveguide (c), the H-field has another direction H_z – the red dash line underneath the middle layer. The function of the taper (b) is to make the magnetic field have a component in the Z direction.

The width and length of a taper will determine its performance. Normally, the length needs to be less then $\lambda/4$. Quite a few simulations of the optimization need to be done in HFSS, in order to reach the maximum H-field matching.

Figure 3.7 shows the dimensions of the microstrip transmission line with the taper for each type of folded waveguide. Because of the different width of each waveguide, the widths of the microstrip line are different, which will give 50 ohm impedance on the port.

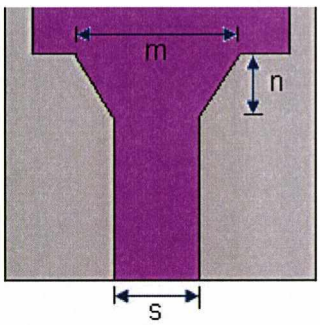

m	n	s
3.06	7.5	0.6

Two layers

m	n	s
3	6	0.6

Three layers

m	n	s
2.2	5.4	0.6

Four layers

Figure 3.7. Dimensions of the transitions for multilayer waveguides

The microstrip transmission line is always connected to the top metal layer of the folded waveguide. The ground plane of the microstrip line will connect to the first metal layer of folded waveguide. Figure 3.8 shows the geometries of the transitions. The two layers folded waveguide is used as an example.

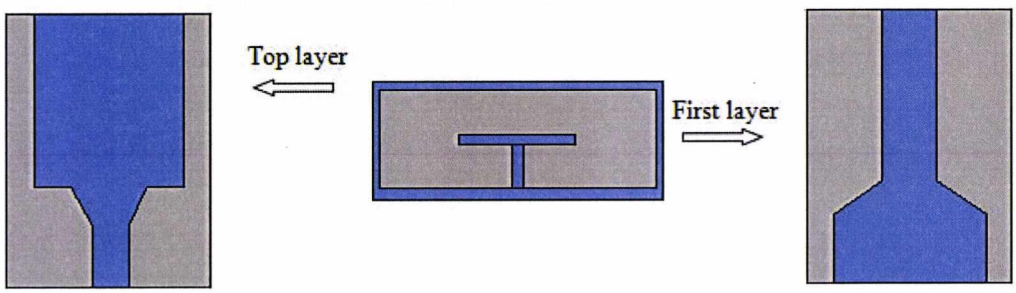

Figure 3.8. Geometries of transitions

3.3 Simulated and measured results

Ansoft HFSS is the software we used to simulate the waveguides with transitions. The dielectric material is Roger RT Duriod 6010 with the dielectric constant of ε_r=10.8. The thickness of the material is 0.635mm. Figure 3.9 to 3.11 show the S parameters for different numbers of layers. The brown lines are the magnitudes of S_{21} in dB, and the red lines are the magnitudes of S_{11} in dB.

Also, the bandwidth of each type has been calculated by f_{c2}/f_{c1}. f_{c1} is the cut off frequency of the fundamental mode and f_{c2} is the cut off frequency of the second order mode.

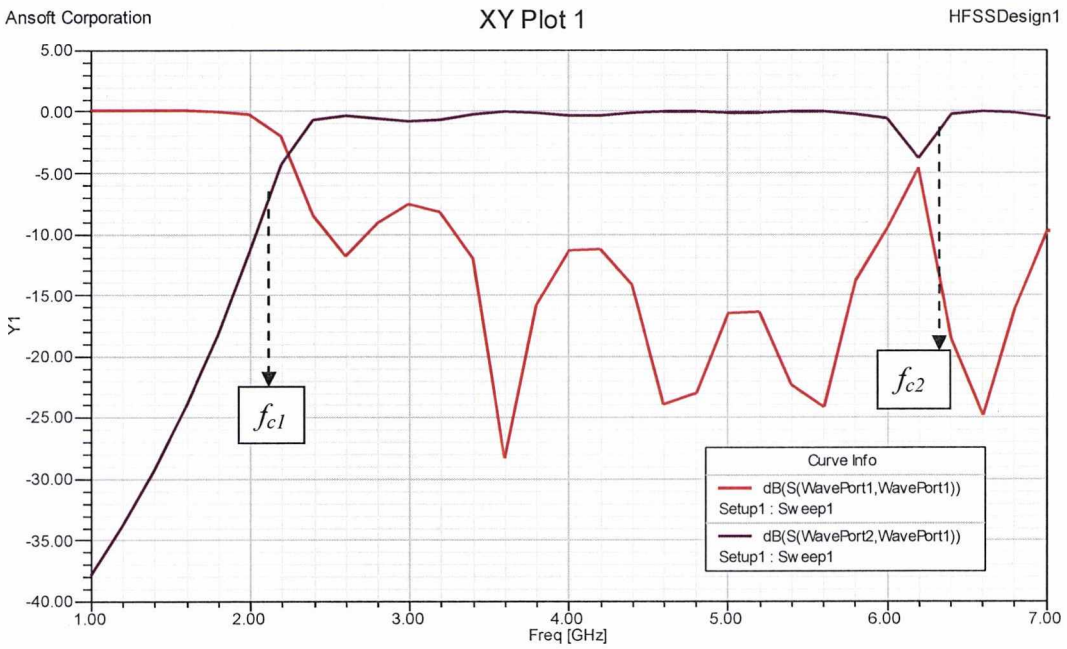

Figure 3.9. Simulated S parameters (dB) of two layers folded waveguide

The bandwidth of two layers folded waveguide is f_{c2}/f_{c1}=2.9.

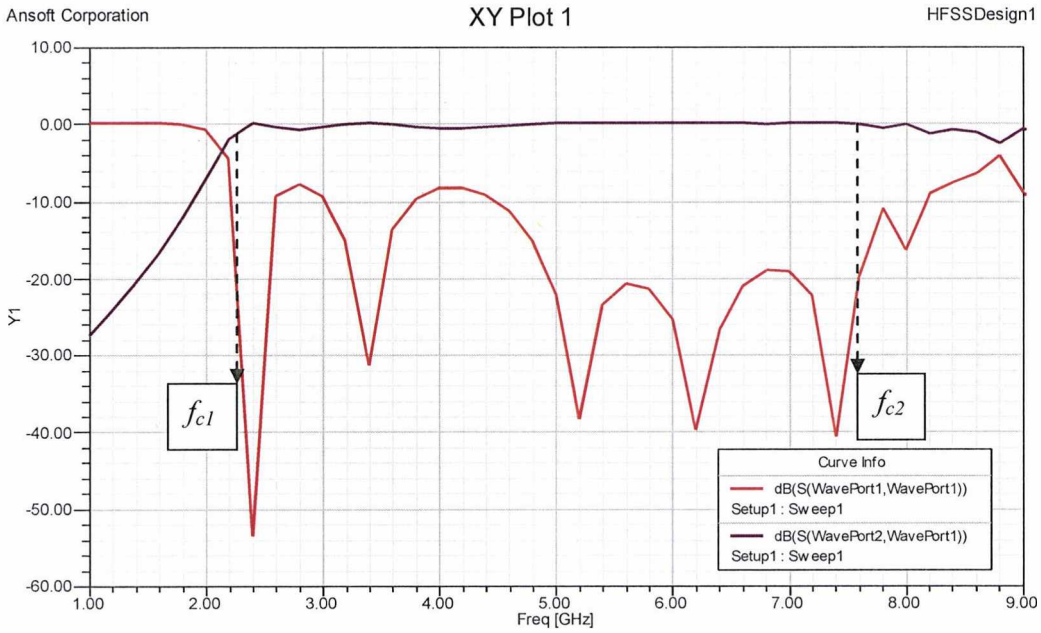

Figure 3.10. Simulated S parameters (dB) of three layers folded waveguide

The bandwidth of three layers folded waveguide is f_{c2}/f_{c1}=3.3.

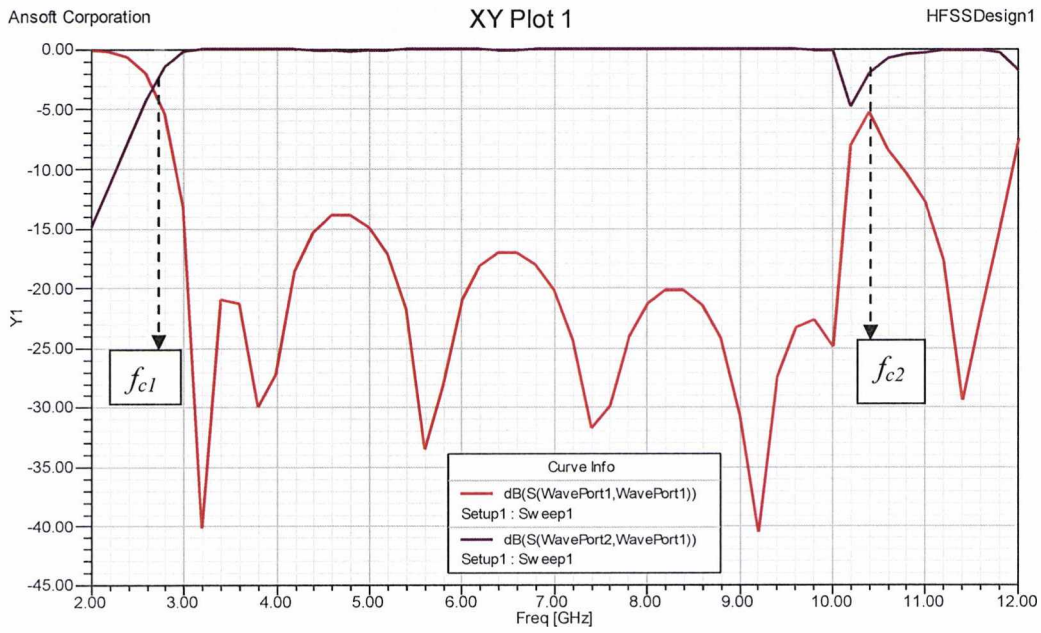

Figure 3.11 Simulated S parameters (dB) of four layers folded waveguide

The bandwidth of four layers folded waveguide is f_{c2}/f_{c1}=4.

The traditional PCB fabrication techniques are applied to manufacture the folded waveguides. Figure 3.12–3.14 shows the fabricated waveguides with SMA connectors and the measured results. We can see that the results are not as good as simulated. The transmissions only operate in the limited range in each folded waveguide. However, the crude fabrication techniques cause more losses and reflections. Additionally, assembling the multiple boards manually is very difficult which has a negative affect on the propagation.

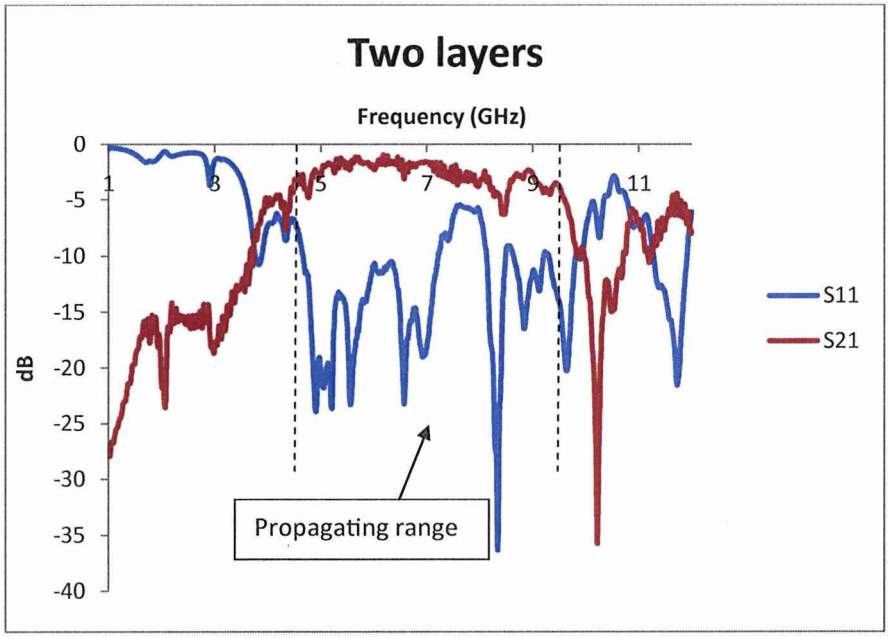

Figure 3.12. Measured S parameters of two layers folded waveguide

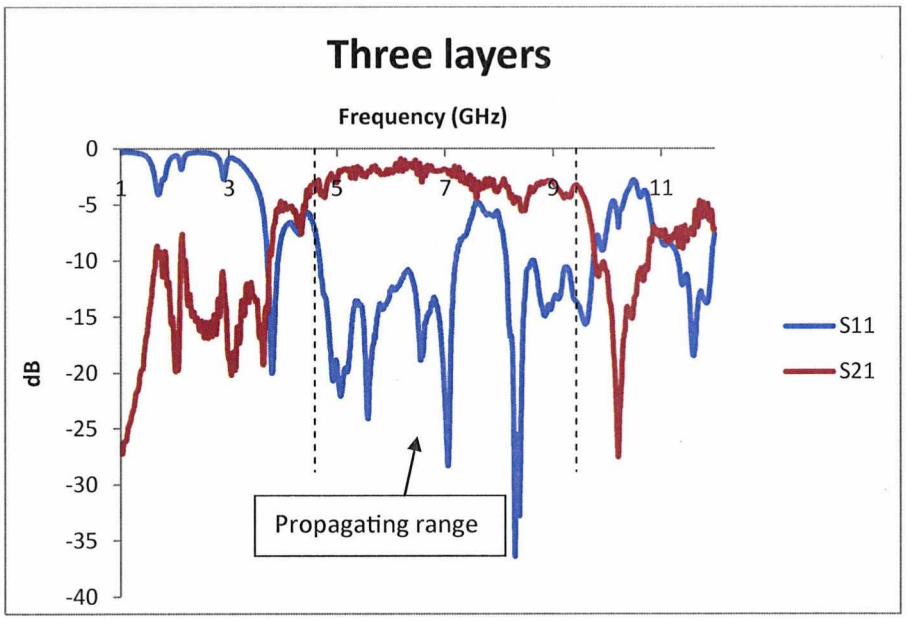

Figure 3.13. Measured S parameters of three layers folded waveguide

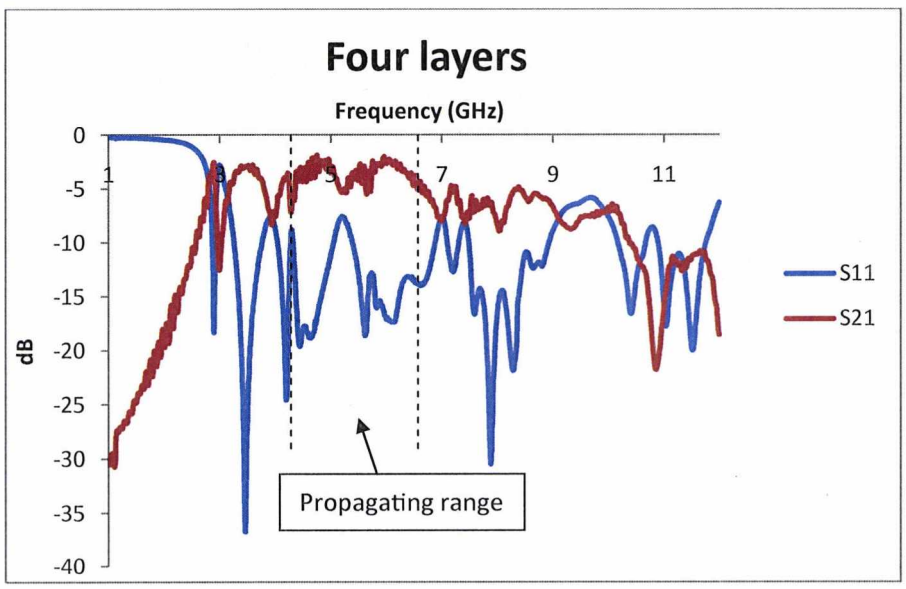

Figure 3.14. Measured S parameters of four layers folded waveguide

A photograph of the fabricated structures is shown in figure 3.15.

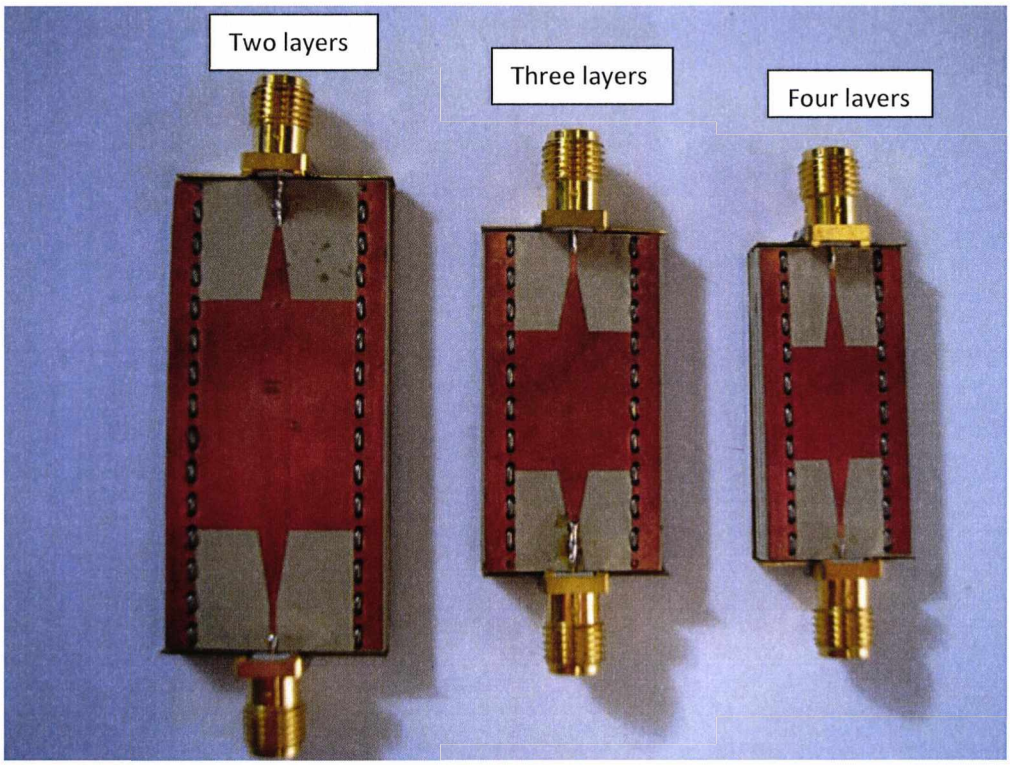

Figure 3.15. A photograph of fabricated structures

3.4 Narrowband folded substrate integrated waveguides

In last section, the broadband folded waveguides had been introduced, that have the bandwidths f_{c2}/f_{c1} vary from 2.9 to 4. This section shows a brief design of the narrowband folded waveguide, which will decrease the bandwidth to a certain level. Although the bandwidth has been reduced, the size of the folded waveguide becomes smaller. This could be the advantage in some narrowband application. However, the narrowband waveguides have the disadvantage of high insertion loss, because the metallised planes are closed to the side walls.

Figure 3.16 shows the dimensions of the three types of narrowband folded waveguide. They keep the same height, but the widths of the guides are shorter. The widths of the planes inside have been increased to decrease the bandwidth.

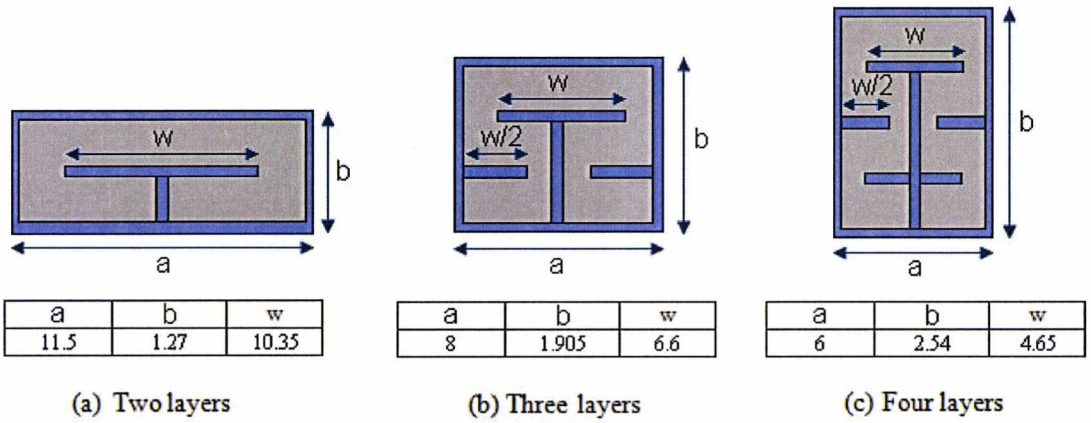

a	b	w
11.5	1.27	10.35

(a) Two layers

a	b	w
8	1.905	6.6

(b) Three layers

a	b	w
6	2.54	4.65

(c) Four layers

Figure 3.16. Dimensions of narrowband folded waveguides

Figure 3.17 shows the reduction of the bandwidth in each type of the folded waveguide. Approximately, all the bandwidths have been decreased to 2, which is the same as conventional waveguide.

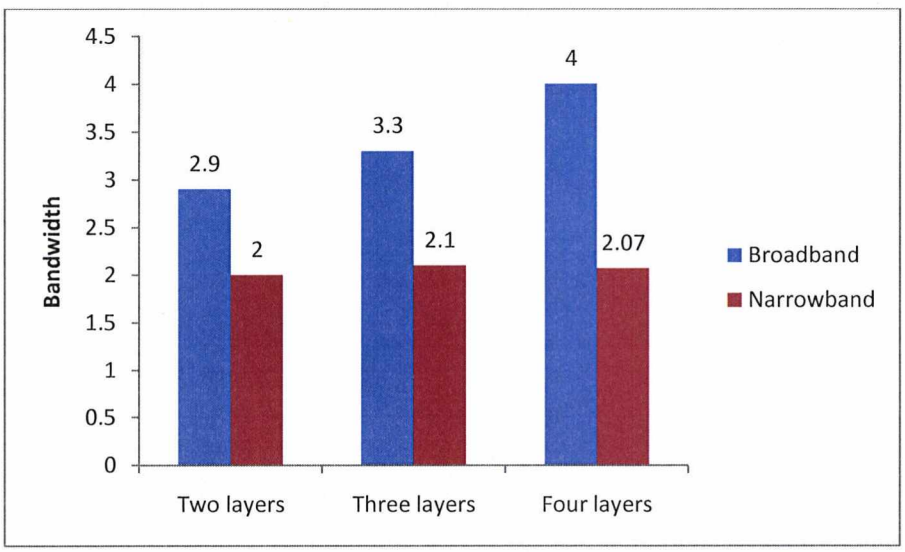

Figure 3.17. Bandwidth comparison between broadband and narrowband waveguides

3.5 Multilayer half-mode folded waveguides

In this section, the half mode folded waveguide will be introduced. It is well known that the folded waveguide has the maximum E-field in the first layer at the dominant mode. If the guide is cut in the middle vertical plane, there will be an open plane in the first layer, which is at the maximum E-field region. At the dominant mode, the open side can be considered as a magnetic wall, and it will keep the original field distribution along the transmission direction. The guide will propagate the half TE_{10} mode, which is called as the half mode folded substrate integrated waveguide. Some other groups had the publications at half mode transmissions, such as [20].

Figure 3.18 shows the cross section views and the field distributions of each type of half mode folded waveguide

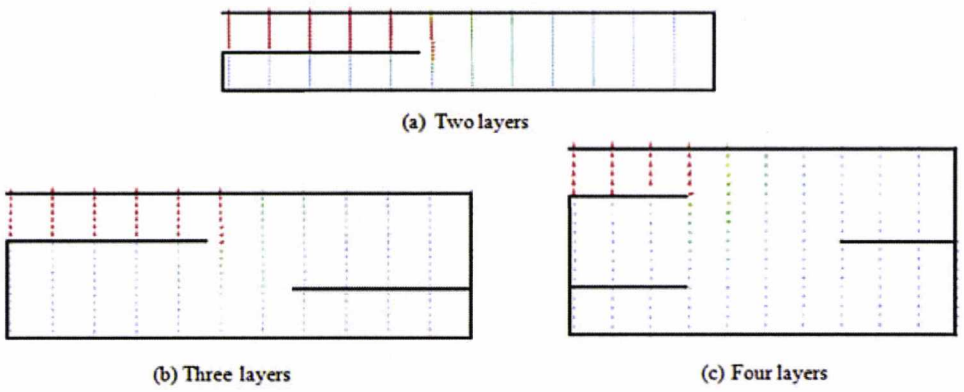

Figure 3.18. E-Fields of each type half mode folded waveguide

3.5.1 Simulations

In order to match the field distribution, the taper of the feed line need to be half as well. The microstrip is still used as the transmission line. By optimizing the transition, the propagations of half mode folded waveguides are shown in figure 3.19–3.21. The brown lines are the magnitudes of S_{21} in dB, and the red lines are the magnitudes of S_{11} in dB.

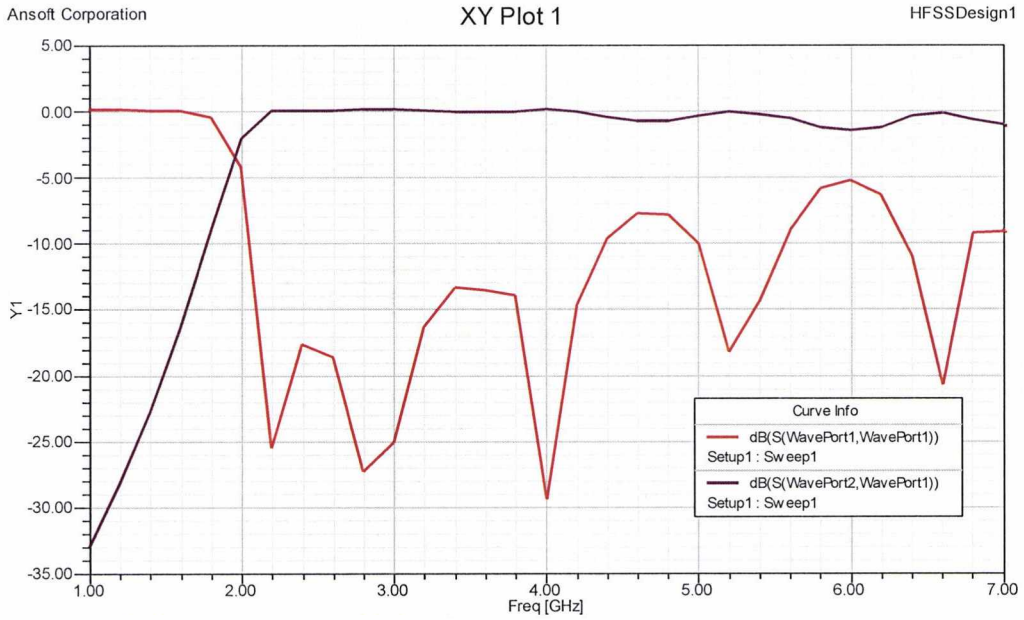

Figure 3.19. Simulated S parameters (dB) of two layers half mode folded waveguide

The bandwidth of two layers half mode folded waveguide is f_{c2}/f_{c1}=1.4.

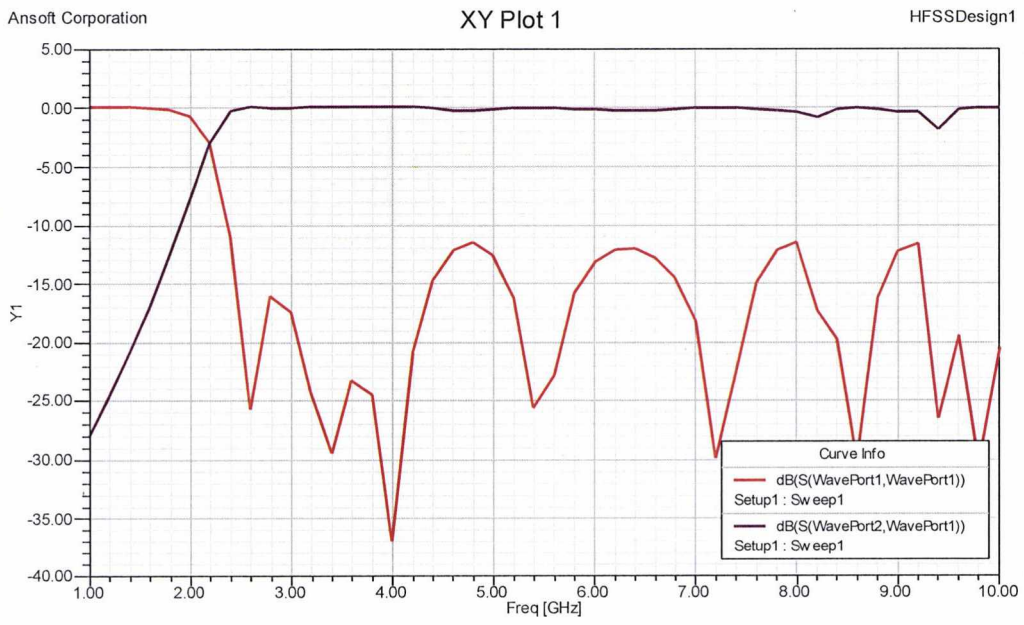

Figure 3.20. Simulated S parameters (dB) of three layers half mode folded waveguide

The bandwidth of three layers half mode folded waveguide is f_{c2}/f_{c1}=1.7.

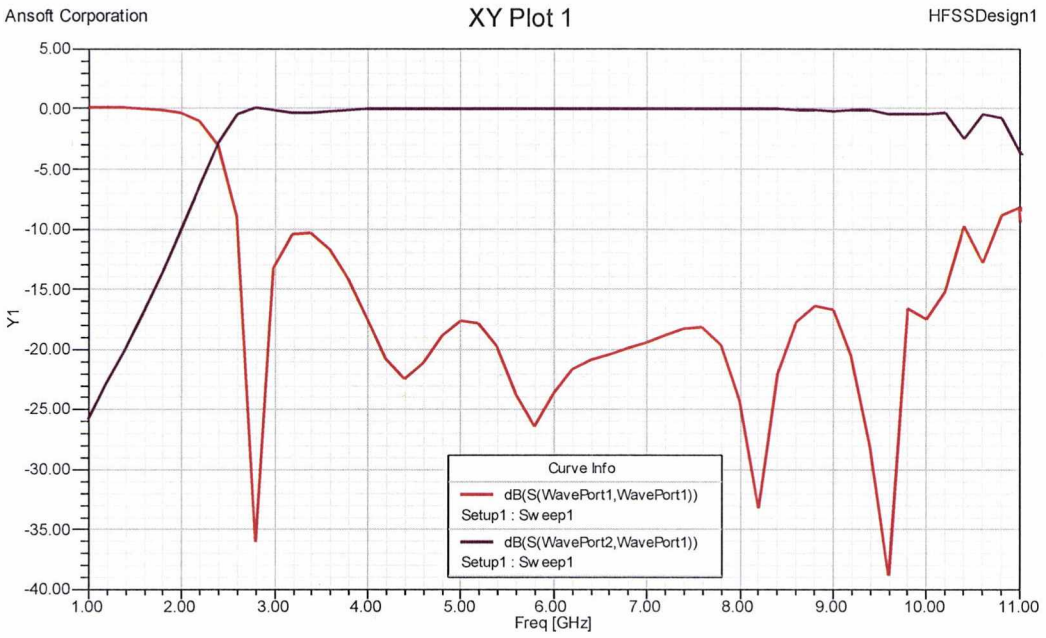

Figure 3.21. Simulated S parameters (dB) of four layers half mode folded waveguide

The bandwidth of four layers half mode folded waveguide is f_{c2}/f_{c1}=2.6.

Although the bandwidth of the half mode folded waveguides are narrow compared with the normal folded ones, the sizes of the structures are further reduced. With some more optimizations, the bandwidth of the half mode folded waveguide can be greatly improved.

3.6 Summary

In this chapter, the multilayer folded substrate integrated waveguide (FSIW) has been presented. The purpose is to study how the FSIW works by optimizing the microstrip transmission line and the taper. Novel transitions designed for the multilayer folded waveguide are demonstrated. The four layers FSIW has the maximum bandwidth, which is approximately twice than the normal SIW. However, due to the layer increases, the fabrication becomes more complicated.

Then a brief study of the narrowband waveguide is proposed. The cross section size of the waveguide has been reduced as the bandwidth becomes narrow. A bandwidth comparison of broad and narrow bands is shown.

The novel folded half-mode substrate integrated waveguide (FHMSIW) is presented which has the further cross-sectional size reduction. The FHMSIW propagates half guided waves and can keep the original E-field distribution. The half-mode SIW has been independently discovered by other groups as well. A further research based on the half-mode substrate integrated waveguide will be demonstrated in the next chapter.

References

[1] J. Hirokawa and M. Ando, "Single-layer feed waveguide consisting of posts for plane TEM wave excitation in parallel plates," *IEEE Trans. Antennas Propag.*, vol. 46, no. 5, pp. 625–630, May 1998.

[2] H. Uchimura, T. Takenoshita, and M. Fujii, "Development of a laminated waveguide," *IEEE Trans. Microw. Theory Tech.*, vol. 46, no. 12, pp. 2438–2443, Dec. 1998.

[3] D. Deslandes and K. Wu, "Integrated microstrip and rectangular waveguide in planar form," *IEEE Microw. Guided Wave Lett.*, vol. 11, no. 2, pp. 68–70, Feb. 2001.

[4] W. Menzal and J. Kassner, "Millimeter-wave 3-D integration techniques using LTCC and related multilayer circuits," in *Proc. 30th European Microwave Conf.*, Paris, France, pp. 33-53, 2000.

[5] D. Stephens, P. R. Young and I. D. Robertson, "Millimeter-wave substrate integrated waveguides and filters in photoimageable thick-film technology," *IEEE Trans. Microwave Theory Tech.*, Vol. 53, No. 12, pp. 3822-3838, December 2005.

[6] Y. Cassivi and K. Wu, "Dispersion characteristics of substrate integrated rectangular waveguide," *IEEE Microw. Wireless Compon. Lett.*, vol. 12, no. 9, pp. 333–335, Sep. 2002.

[7] L. Yan, W. Hong, K. Wu, and T. J. Cui, "Investigations on the propagation characteristics of the substrate integrated waveguide based on the method of lines," *Proc. Inst. Elect. Eng.—Microw., Antennas, Propag.*, vol. 152, no. 1, pt. H, pp. 35–42, Feb. 2005.

[8] F. Xu and K. Wu, "Guided-wave and leakage characteristics of substrate integrated waveguide," *IEEE Trans. Microw. Theory Tech.*, vol. 53, no. 1, pp. 66–72, Jan. 2005.

[9] L. Yan, W. Hong, G. Hua, J. X. Chen, K. Wu, and T. J. Cui, "Simulation and experiment on SIW slot array antennas," *IEEE Microw. Wireless Compon. Lett.*, vol. 14, pp. 446–448, Sep. 2004.

[10] A. J. Farrall and P. R. Young, "Integrated waveguide slot antennas," *Electron. Lett.*, vol. 40, no. 16, pp. 974-975, Aug 2004.

[11] Z. C. Hao, W. Hong, J. X. Chen, X. P. Chen, and K. Wu, "Compact super-wide bandpass substrate integrated waveguide (SIW) filters," *IEEE Trans. Microw. Theory Tech.*, vol. 53, no. 9, pp. 2968–2977, Sep. 2005.

[12] E. Moldovan, R. G. Bosisio, and K. Wu, "W-band multiport substrate integrated waveguide circuits," *IEEE Trans. Microw. Theory Tech.*, vol. 54, no. 2, pp. 625–632, Feb. 2006.

[13]N. Grigoropoulos and P. R. Young, "Compact folded waveguides," in *34th Eur. Microw. Conf.*, Amsterdam, The Netherlands, pp. 973–976, 2004.

[14] B. Sanz Izqueirdo, N. Grigoropoulos, and P. R. Young, "Ultra-wideband multilayer substrate integrated folded waveguides," in *IEEE MTT-S International Microwave Symposium Digest.*, pp. 610–612, Jun. 2006.

[15] N. Grigoropoulos, B. Sanz Izquierdo, and P. R. Young, "Substrate integrated folded waveguide (SIFW) and filters," *IEEE Microwave wireless compon. Lett.*, Vol. 15, No.12, pp.829-831, Dec. 2005.

[16] B. Sanz Izquierdo, and P. R. Young, N.Grigoropoulos, J. C. Batchelor and R. J. Langley, "Substrate Integrated Folded Waveguides (SIFW) slot antenna," *Pro. IEEE Int. Workshop Antenna Technology,* pp. 307-309, Mar. 2005.

[17] Guo Hua Zhai, Wei Hong, Ke Wu, Ji Xin Chen, Peng Chen, and Hong Jun Tang, " Substrate Integrated Folded Waveguide (SIFW) narrow-wall directional coupler, " *International Conference on Microwave and Millimeter Wave Technology,* vol.1, pp.174-177, 2008.

[18] Shry-Sann Liao, Hsien-Ku Chen, Hsien-Yuan Liao, and Yin-Cheng Chang, "Novel Compact Narrowband CPW Bandpass Filter Using an Efficient Loaded Structure," *Microwave Opt. Technol. Lett.*, Vol. 42, No. 3, August 5 2004.

[19] Nikolaos Grigoropoulos, "Novel substrate integrated waveguides and components," *PhD thesis to the University of Kent*, September 2005.

[20] Guo Hua Zhai, Wei Hong, Ke Wu, Ji Xin Chen, Peng Chen, Jing Wei, and Hong Jun Tang, "Folded Half Mode Substrate Integrated Waveguide 3 dB Coupler, " *IEEE Microwave wireless compon. Lett.,* vol. 18, no. 8, pp.512-514, 2008.

4. Planar half-mode substrate integrated waveguide

The substrate integrated folded waveguide (SIFW) has been introduced in previous chapter, and it has a further reduction on the transverse size of the SIW. However, for the multilayer folded waveguide, the total metallic cross section area is not reduced [1], which means the conductive loss keeps the same level as SIW. Recently, a half mode substrate integrated waveguide (HMSIW) has been demonstrated, which has further width and metallic surface reduction when compared to SIW. For the dominant mode of a SIW, it has the maximum E-field value in the symmetric central plane along the transmission direction. Thus, if the waveguide is cut into half along the vertical middle direction, the cutting plane can be considered as a magnetic wall. With the large width-to-height ratio (WHR), the half part can still keep the original field distribution in order to support the propagation modes. Each half part can propagate the half guided waves [2]. This improved new structure is called "half mode substrate integrated waveguide (HMSIW)". Figure 4.1 shows the fundamental mode E-field of these two kinds of waveguide. It is clear that HMSIW keeps almost half field distribution and the open side works as an equivalent magnetic wall.

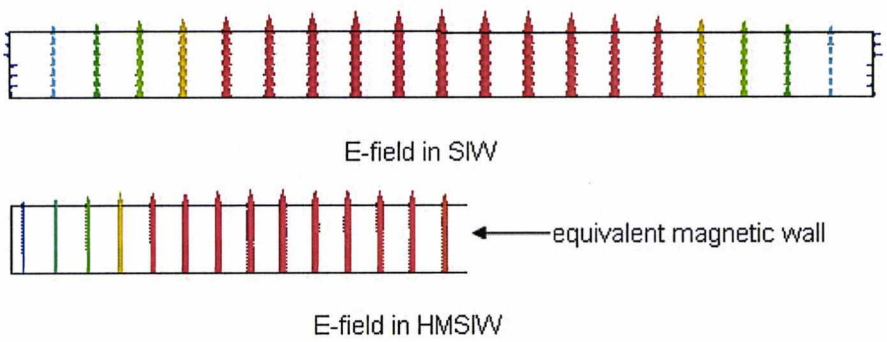

Figure 4.1. Fundamental mode E-fields in SIW and HMSIW

While keeping most advantages of SIW, the size of the HMSIW is almost reduced by half and the bandwidth becomes much wider [3]. Many applications have been designed based on this new technique, such as antennas [4] [5], couplers [6][7], filters [8-11], and power dividers [12] etc. Furthermore, half-mode waveguides can be easily integrated with other planar circuits [13] or components [14].

In this chapter, a new planar half-mode substrate integrated waveguide is presented. This new type HMSIW can easily integrate with other electric components and the bandwidth can be well controlled by the slot on the top.

4.1 The design of planar half-mode substrate integrated waveguide

In this section, we present a new waveguide based on the HMSIW. Figure 4.2 shows the process of the planar half mode substrate integrated waveguide. A metal plane has been added on the right side which was the open side in HMSIW. On the top layer, a new plane is added. Because of the plane on the top layer of the HMSIW, we call it as "planar-HMSIW". In PCB fabrication, components are hard to integrate between the top and bottom layers on the open side of the HMSIW. In our design, a metal part is put on the top layer of the open side in order to integrate other components along the slot.

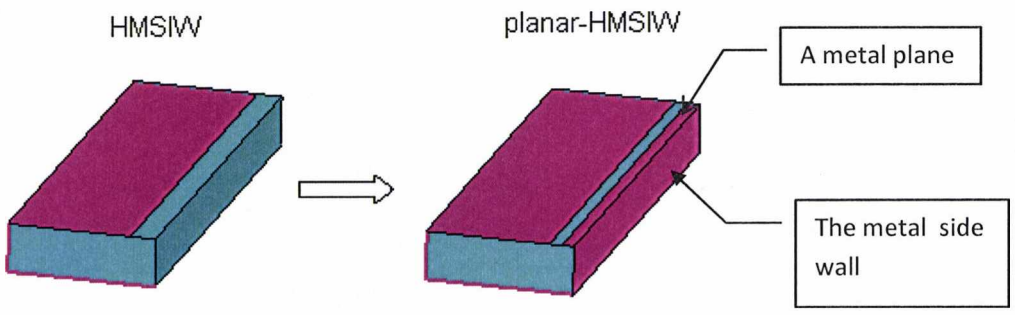

Figure 4.2. Process of the new planar-HMSIW

By adding this planar slot on the top, a very low capacitance exists along the air gap. Additionally, even with this metallic surface, the field distribution is still very similar to that of the HMSIW. We use HFSS to simulate the waveguide modes, and figure 4.3 shows the port E-field comparison.

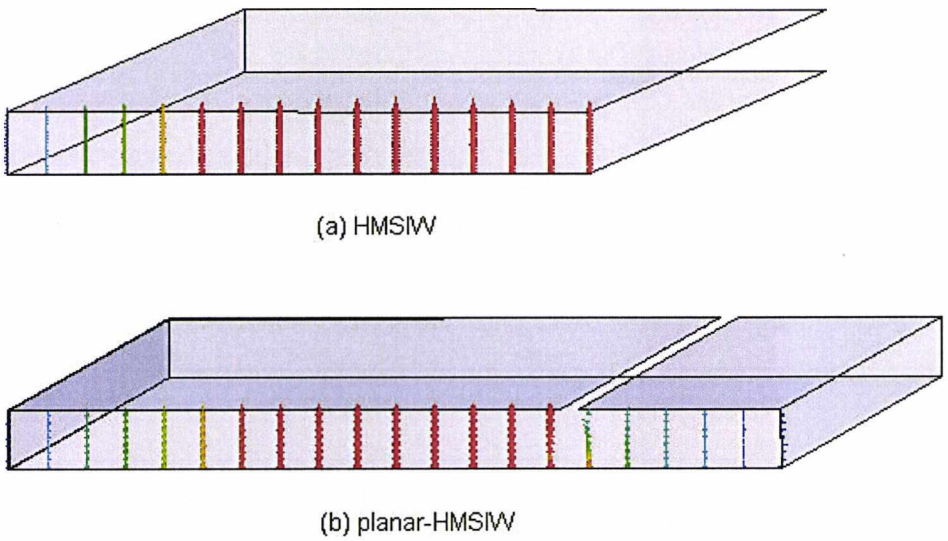

Figure 4.3. E-field comparison between HMSIW and planar-HMSIW

For the HMSIW, the maximum E-field is at the right edge of the waveguide, which is considered as a magnetic wall. For the planar-HMSIW, the E-field plot is very similar to the HMSIW, with the addition of fields under the planar part, which have little affect on the fundamental propagation. Figure 4.4 shows the dominate mode with the transition.

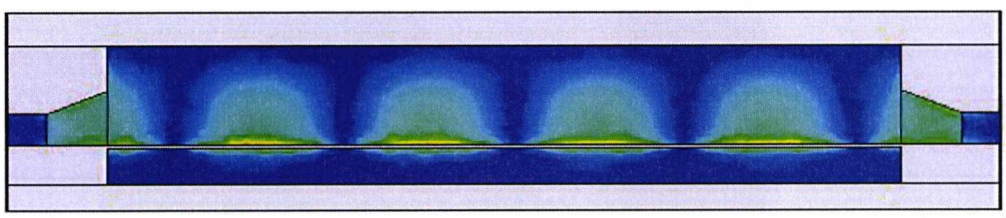

Figure 4.4. Dominate mode with the transition

The total width of the waveguide is a, and the height is b. The geometry of planar half-mode SIW is shown in figure 4.5.

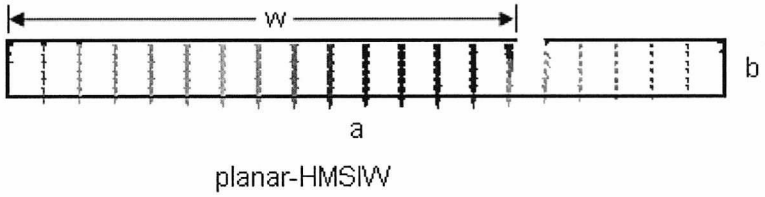

Figure 4.5 Geometry of planar-HMSIW

According to the actual port field plot (figure 4.5), the dominant field distribution is very similar to the traditional HMSIW. Because the planar part has little affect on the fundamental mode propagation, we can approximately consider the effective width of the planar-HMSIW is $a_{eff} = 2w$. Thus, the cut off frequency of the fundamental mode can be calculated approximately by:

$$f_c = \frac{c}{2a_{eff}\sqrt{\varepsilon_r}} \tag{4.1}$$

Here the effective width a_{eff} is the width of the full mode waveguide which has the same dispersion curve as the half-mode SIW with the width of a.

We use the microstrip with 50Ω port characteristics at the operating frequency as the feeding transmission line. A well-designed taper integrates the microstrip to the waveguide. Furthermore, the magnitude of the electric field only propagates half in the guide. Therefore, the taper must be designed as the half model.

Figure 4.6 shows the difference of magnitude of the electric field on the top layer between the full and half mode taper. These two kinds of taper all spread E field very well to match the fields in the waveguides.

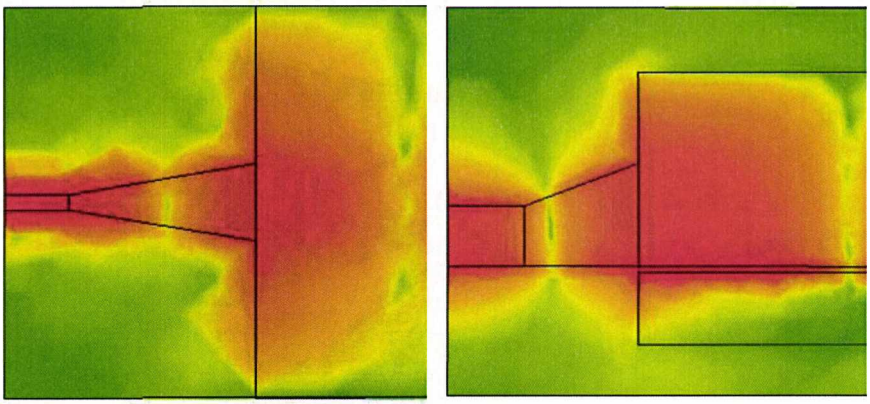

Figure 4.6. E-field comparison between full and half mode taper

4.1.1 Planar half-mode SIW simulation

The layout and dimensions are shown in figure 4.7.

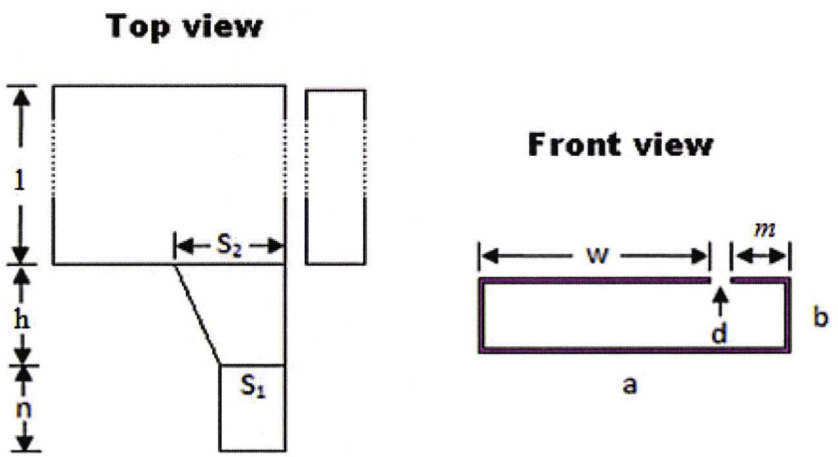

l	h	n	S_1	S_2	a	b	w	m	d
120	9	6	4.6	8	21	1.57	15	5.5	0.5

Figure 4.7. The layout and dimensions (unit: mm) of planar half-mode SIW

Here we use the dielectric material with the permittivity 2.33, the effective width is $2w$. Thus, the fundamental mode f_c is:

$$f_c = \frac{c}{2a_{eff}\sqrt{\varepsilon_r}} \approx 3.27GHz \tag{4.2}$$

The Ansoft HFSS is used to design and optimize and the structure. The dispersion figure of β from HFSS is shown in figure 4.8.

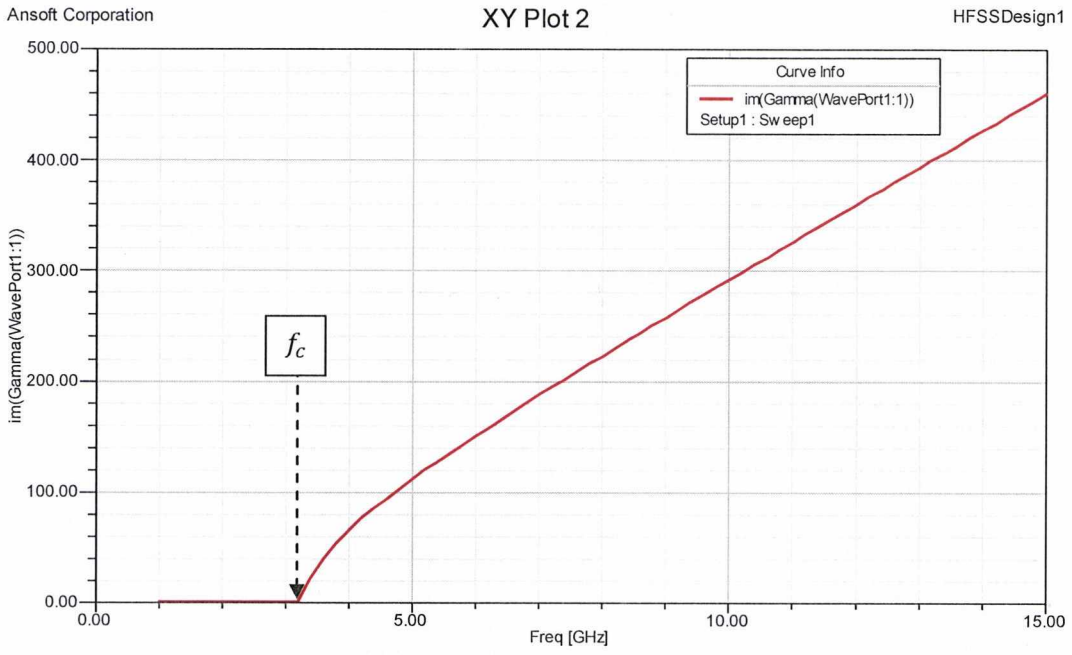

Figure 4.8. Simulated phase constant dispersion figure of the fundamental mode

This figure shows the imaginary part of the Gamma. The cut off frequency is approximately at 3.2GHz, which is the same as the calculated result. The S parameter result is shown in figure 4.9.

The simulation is set in a perfect environment without any conductive and dielectric losses. All the metallic surfaces are perfect electric planes, and the PML boundary is set to absorb any leaky waves. We see from figure 4.9 that S_{21} has very little insertion loss during the

propagation, and its cut off frequency is about 3.2GHz. The reflection S_{11} is almost below -20dB over the entire band.

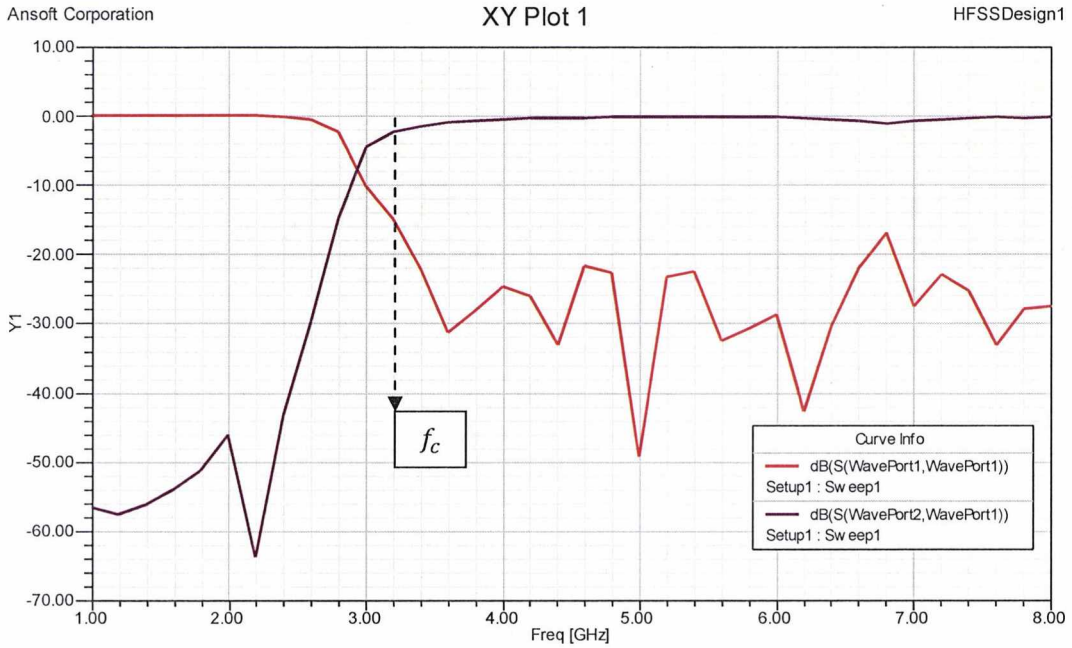

Figure 4.9. Simulated S parameters (dB) of planar half-mode SIW

4.1.2 Fabrication and measurements

The convertional PCB fabrication technique is used to build up this waveguide in the mechanical workshop. The material we use is Rogers RT Duriod 5870 with dielectric constant ε_r =2.33 and 1.57mm thickness. The drilling machine is used to drill series holes on both sides, through which the copper vias could form the conducting walls. The vias' diameter is 0.5mm and the distance between adjacent vias is 1mm. In the end, a 50Ω impendence SMA connector is soldered on each port. Figure 4.10 shows the picture of the fabrication.

The length of the structure is three times of the wavelength at 5GHz. That is because we try to put components on the top for further researches.

Figure 4.10. Pictures of fabricated structure

The structure is measured by the Anritsu 37397C vector network analyzer. The frequency range we use is from 1GHz to 8GHz. Figure 4.11 shows the S parameter measurement results compared with the simulation results.

The measured results and simulated results compared very well. Both cut off frequencies of these two S_{21} are around 3GHz, the insertion loss of measured one has about -1~2dB during the fundamental mode and increases to -3dB above 6.5GHz. The manual fabrication method and dielectric material and conductor loss may cause this problem.

The measured reflection S_{11} are all below -20dB in the fundamental mode, except two reflection points reach to -17dB.

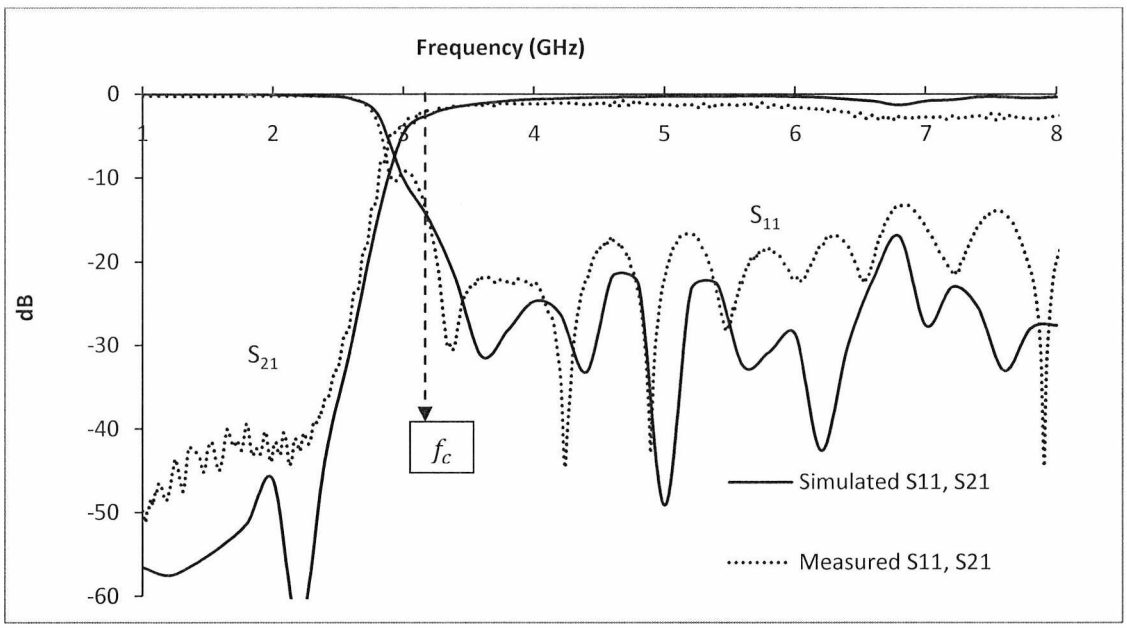

Figure 4.11. Comparison between simulated and measured S parameters

4.1.3 Propagation modes discussions of the planar HMSIW

Conventional half-mode waveguide propagates half the guided $TE_{1,0}$ mode as the fundamental mode, which is called the $TE_{0.5,0}$ mode. In the second order mode, which is $TE_{1.5,0}$, the relative cut off frequency is three times that of $TE_{0.5,0}$.

Figure 4.12 is the field plots of these two modes in the typical half-mode waveguide. The dominant mode has the maximum E-field near the magnetic wall which is the open side. The $TE_{1.5,0}$ mode varies with two maxima. This mode has one peak near the left edge and another half peak on the open edge.

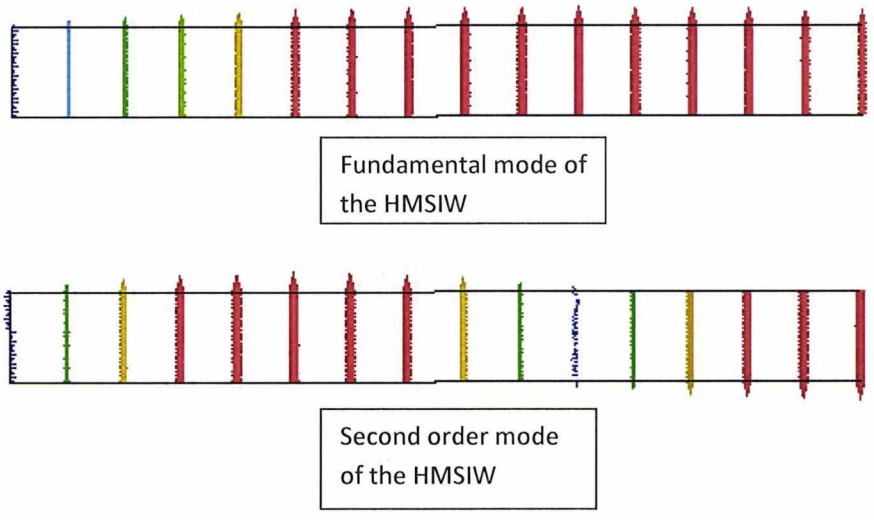

Figure 4.12. Simulated E-vector plots for the fundamental and second order modes for the conventional half-mode SIW

In the planar half-mode SIW, we have the planar part on the right edge of the guide. Thus, the field distributions are different from the conventional half-mode SIW. We found the second order mode occurs at 6.2GHz, and the E-field has a maximum on the right edge. Figure 4.13 shows the phase constant dispersion curves for three modes. Fig4.14-4.16 shows the E-field distribution on the port of each mode.

At the end of this chapter, we will have a theoritical discussion about the propagation constant of this new planar half-mode SIW.

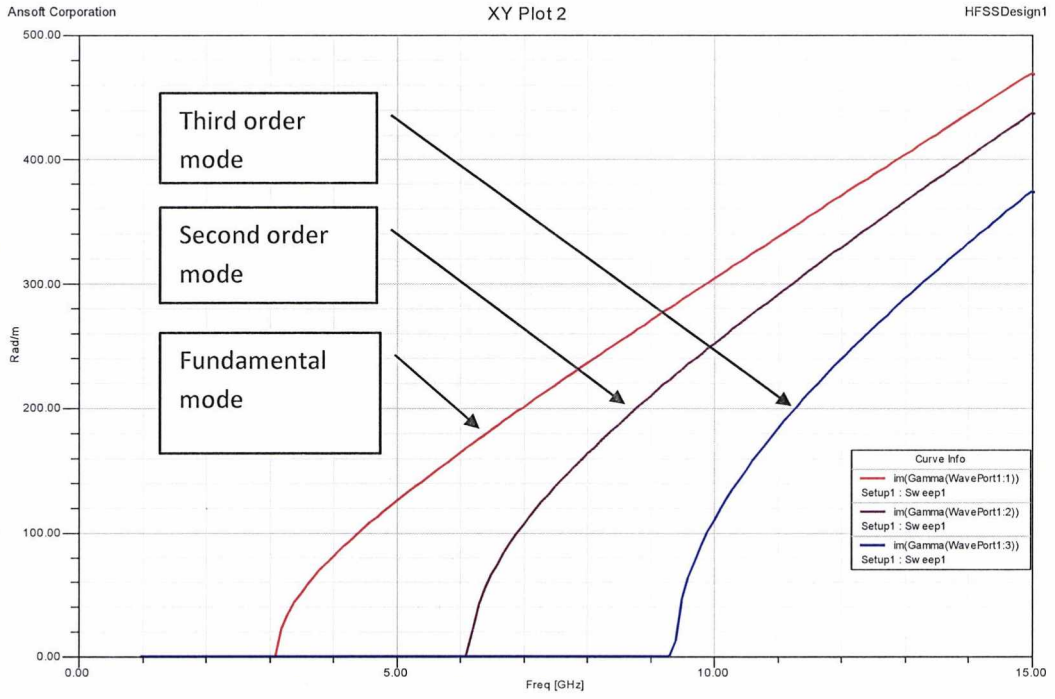

Figure 4.13. Simulated phase dispersion curves for the fundamental, second and third order mode for the planar half-mode SIW

Figure 4.13 shows the phase constant of the first three modes. The operating frequency is 10GHz. In fact, if they are the actual propagation modes, they should all converge to the lightline, which is $\sqrt{\epsilon_r}k_0$.

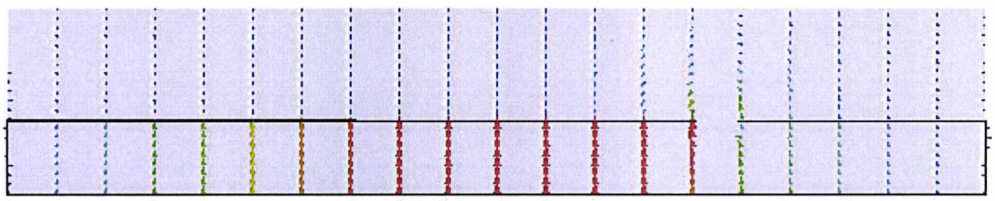

Figure 4.14. Simulated E-vector plot for the fundamental mode of planar half-mode SIW

Figure 4.14 shows the dominant mode, and the field distribution is exactly the same as the conventional HMSIW. The cut-off frequency of the fundamental mode is 3.2GHz.

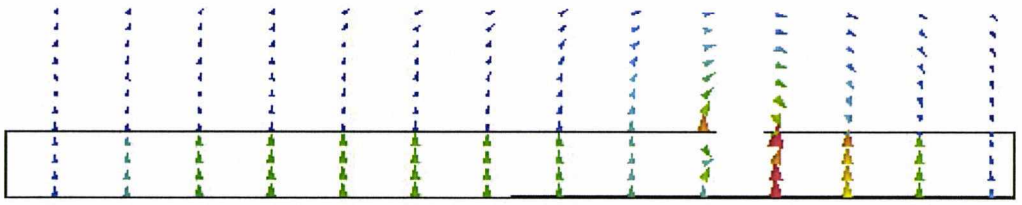

Figure 4.15. Simulated E-vector plot for the second order mode of planar half-mode SIW

The second order mode has a maximum E-field at the right edge of the waveguide. We consider it is a propagating mode, and its cut-off frequency is 6.2GHz.

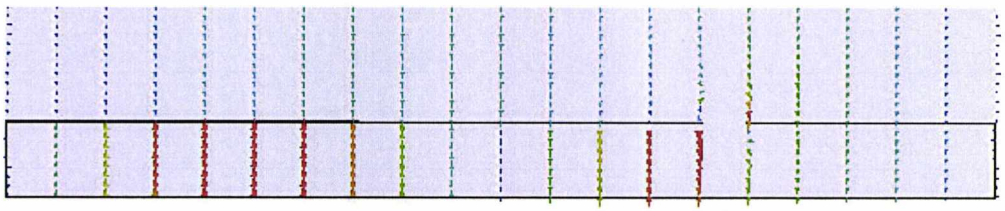

Figure 4.16. Simulated E-vector plot for the third mode of planar half-mode SIW

The third order mode matches with the $TE_{1.5,0}$ mode of the conventional HMSIW. The cut off frequency is 9.4GHz, which is about three times that of the fundamental mode.

4.2 Optimization and loss discussions

In this section, the attenuation of the planar HMSIW has been investigated. The loss tangent and the conductivity of the metal will be added into the model.

On the top layer of the design, there is an air slot. The size of the slot and the position will have some affect on the characteristics of the waveguide. By changing the slot width and

the position, we are about to see how the attenuation and bandwidth change. All the attenuation plots are based on the fundamental mode.

4.2.1 Conductive loss and the dielectric loss

The original simulation in HFSS has no loss in the materials. Actually, the material, RT/duriod 5870, has a dielectric loss tangent $\tan\delta = 0.0012$, and the copper foils have the conductivity σ=5.8×10^7 S/m. The loss plot is shown in figure 4.17.

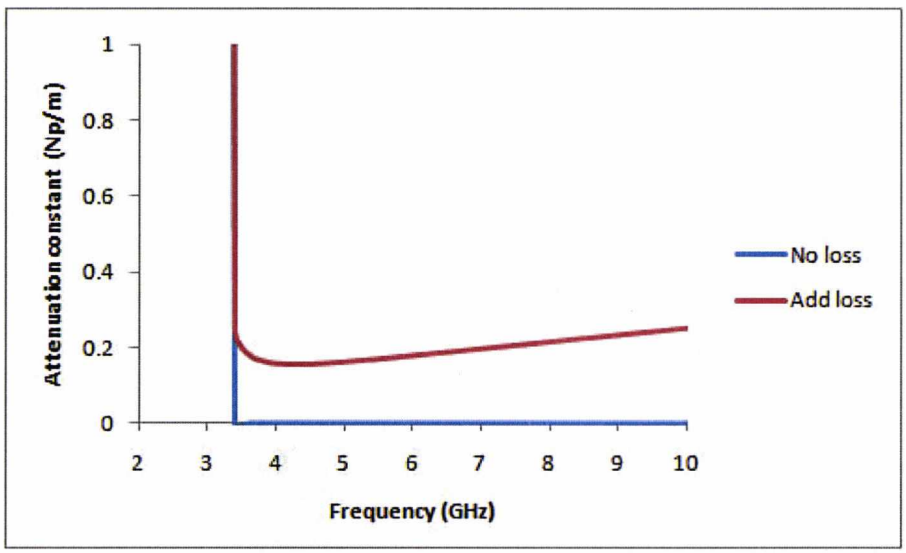

Figure 4.17. Plot of attenuation constant (Np/m) versus frequency (GHz)

This figure is the comparison of the loss. The blue line is the attenuation constant α of the half-mode waveguide without any loss. We can see that the radiation loss does not exist in our structure.

The red line is the attenuation constant of the guide with dielectric and conductive losses. The attenuation constant of the corresponding waveguide with the losses is less than 0.2Np/m at 3.4GHz, which is 1.7dB/m, and then at the higher frequency range, it increases a bit.

4.2.2 Changing the slot width

In this section, we will simulate the half-mode SIW to get the attenuation constants. The first one is to change the slot width *d*, and another one is to change *w* and *m* while keeping the width *d* constant. Geometry is shown in figure 4.18.

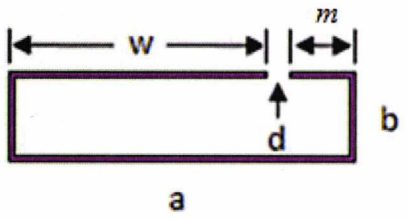

Figure 4.18. Geometry of planar half-mode SIW

The electric field near to the gap relates to the width of the slot. If *d* decreases, the E-field will get more concentrations on the slot. By changing the slot width *d*, the various attenuation constants are plotted in figure 4.19. In this simulation, the six slot widths of 0.1mm, 0.2mm,0.3mm,0.4mm,0.5mm and 1.5mm are applied to the half-mode SIW.

In this figure, as the width increases, the attenuation reduces. However, if the width keeps increasing, the attenuation will not vary much. At *d*=0.5mm, the loss is the lowest.

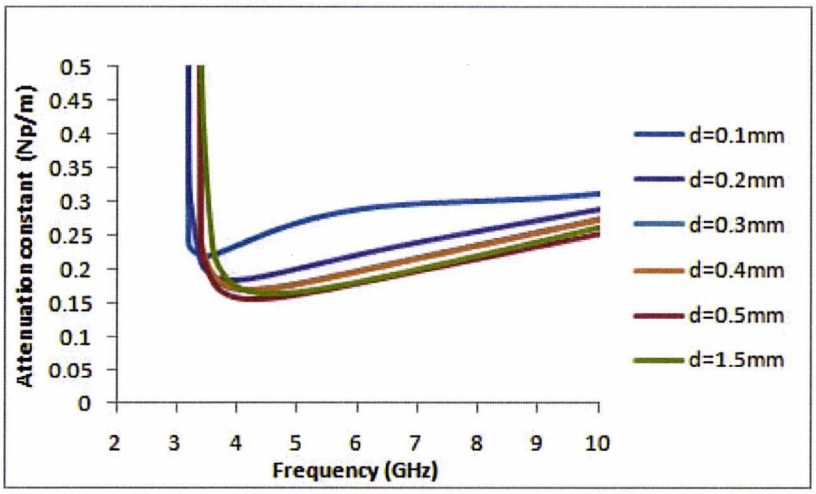

Figure 4.19. Plots of attenuation constants (Np/m) versus frequency (GHz) in different d. Dielectric material: RT/duriod 5870 ($\varepsilon_r = 2.33,\ \tan\delta = 0.0012$).

4.2.3 Changing the slot position

In this simulation, the width of the slot remains as 0.5mm and its position shifts. The total width of the waveguide a is 21mm. The width of the top layer is w, and we choose series of w/a ratios from 0.57 to 0.8 for the test. The attenuation constants versus frequency are plotted in figure 4.20.

The variable w relates to the effective width of the half mode waveguide. The cut off frequency increases while the effective width decreases. During the lower frequency range up to 4GHz, the loss has the lowest value when the w/a ratio is 0.8. At the higher frequency range above 4GHz, the w/a ratio of 0.76 has the lowest loss. However, the attenuation value does not vary much except the case of w/a=0.57. Therefore, as long as the slot position is not too close to the center, it has little affect on the attenuation constant.

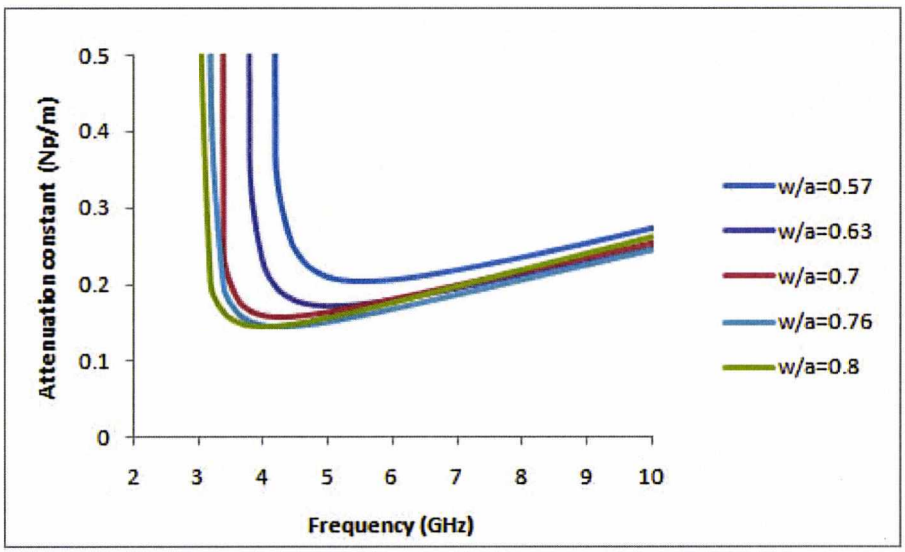

Figure 4.20. Plots of attenuation constants (Np/m) versus frequency (GHz) in different w/a ratios. Dielectric material: RT/duriod 5870 ($\varepsilon_r = 2.33,\ \tan\delta = 0.0012$).

4.2.4 Relative bandwidth

The bandwidth of a waveguide is one of the most important issues. Figure 4.21 shows the relative bandwidth plot in different situations. It is clearly to see that with a slot width 0.1mm and the *w/a* ratio of 0.76, the relative bandwidth f_{c2}/f_{c1} reaches the maximum of 3.83. However, according to the figure 4.19, at d=0.1mm, the attenuation constant is greater than the other cases.

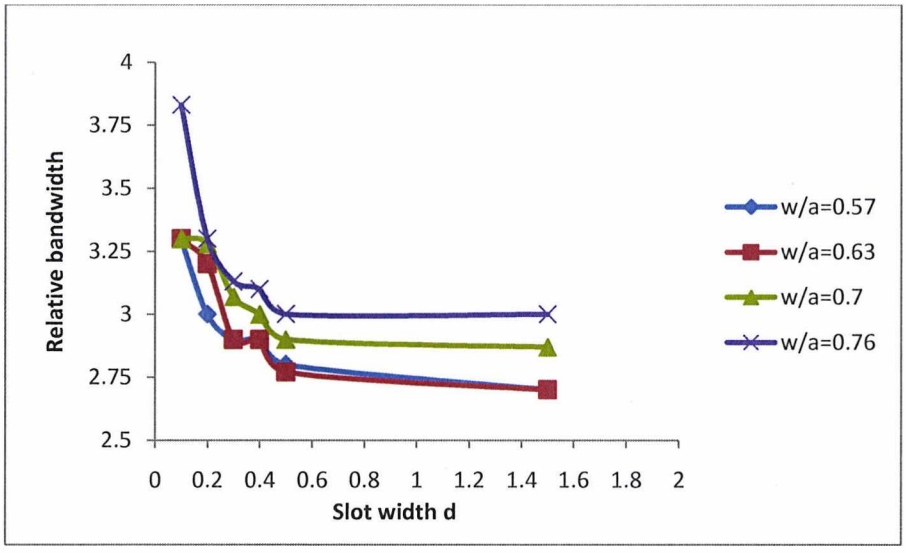

Figure 4.21. Relative bandwidth (f_{c2}/f_{c1}) versus d

4.3 Transverse resonance technique and propagation constants analyses

In this section, we will introduce a method to determine the cut off frequency for the waveguide which has the complex impedance components in the circuit. This method is based on the transverse resonance technique (TRT). The TRT is a wave equation solution, which is easy and direct to determine the cut-off frequency. The propagation constant can be easily solved by analyzing the transmission line equivalent circuit [15].

4.3.1 Conventional rectangular waveguide

In the normal propagation, the wavevector in the waveguide is:

$$|\boldsymbol{k}| = \omega\sqrt{\mu\epsilon} = \sqrt{\beta^2 + k_x^2} \tag{4.3}$$

At the cut off, β=0. The wave bounces back between the two side walls (figure 4.22).

And therefore,

$$|\boldsymbol{k}| = k_x = \omega\sqrt{\mu\epsilon} \tag{4.4}$$

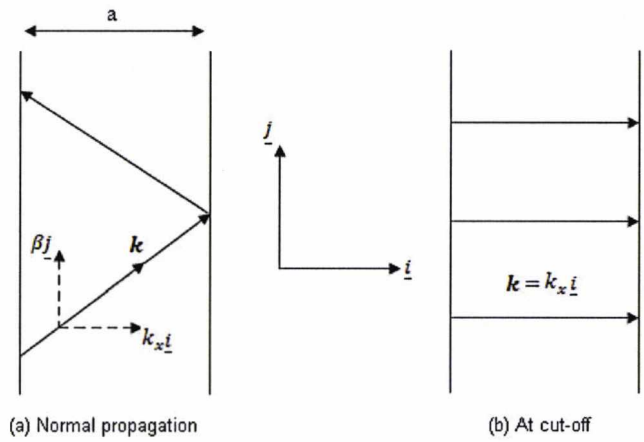

Figure 4.22. Wavevector at (a) normal propagation, (b) cut-off

In this case, we could consider the waveguide as a parallel plate transmission line which is terminated by short circuits (figure 4.23).

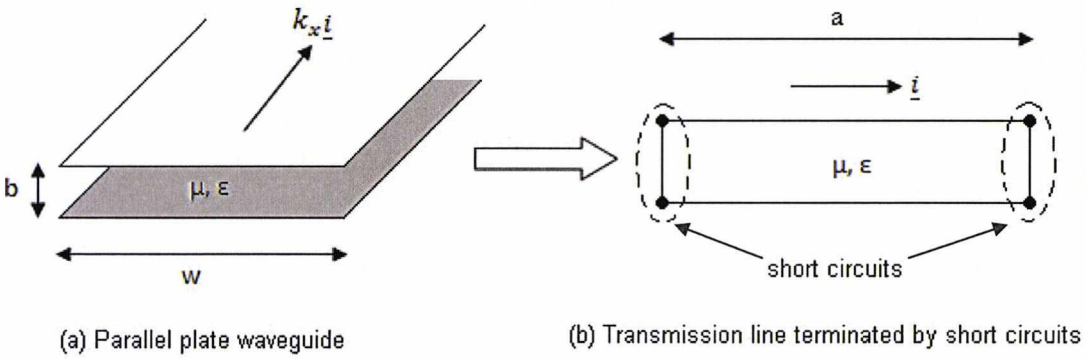

Figure 4.23. (a) geometry of parallel plate waveguide, (b) equivalent circuit of the transmission line terminated by short circuits.

η is the intrinsic impedance of the medium between the parallel plates:

$$\eta = \sqrt{\frac{\mu}{\epsilon}} \tag{4.5}$$

Therefore, the characteristic impedance in the waveguide with the length of w is:

$$Z_0 = \frac{bV}{wI} = \frac{b}{w}\sqrt{\frac{\mu}{\epsilon}} \tag{4.6}$$

To determine the cut-off frequency, we need to find the resonant frequency of the terminated transmission line. If a point along the line has been taken, then the resonance occurs when the value of the impedance in both directions are equal (but opposite in sign) (figure 4.24) [15].

$$Z_{in1} = -Z_{in2} \tag{4.7}$$

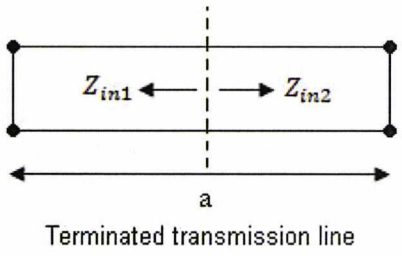

Figure 4.24. The impedances at the resonant point

The input impedance of a terminated transmission line with the load end Z_L (figure 4.25) is:

$$Z_{in} = Z_0 \frac{Z_L + jZ_0 \tan k_x l}{Z_0 + jZ_L \tan k_x l} \tag{4.8}$$

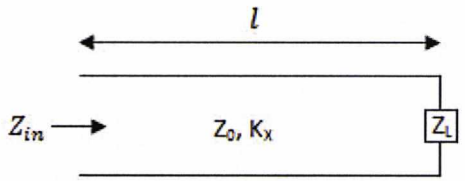

Figure 4.25. Terminated transmission line with the load end Z_L

In our case, the load end is the short circuit. So $Z_L = 0$.

And therefore,

$$Z_{in} = jZ_0 \tan k_x l \tag{4.9}$$

If we choose the point at the end, the width of the transmission line is a, then

$$Z_{in1} = jZ_0 \tan k_x a \tag{4.10}$$

And $Z_{in2} = 0$. So we make Z_{in1} and Z_{in2} equal,

$$jZ_0 \tan k_x a = 0 \tag{4.11}$$

Hence

$$k_x a = n\pi \qquad n = 1, 2, 3 \ldots. \tag{4.12}$$

$$k_x = \frac{n\pi}{a} \tag{4.13}$$

At the cut-off, from equation (4.4) we get $k_x = \omega_c\sqrt{\mu\epsilon}$, where ω_c is the cut off frequency in rad.

And

$$f_c = \frac{\omega}{2\pi} \tag{4.14}$$

So

$$k_x = 2\pi f_c\sqrt{\mu\epsilon} = \frac{n\pi}{a} \tag{4.15}$$

$$f_c = \frac{n}{2a\sqrt{\mu\epsilon}} \qquad n = 1, 2, 3 \ldots. \tag{4.16}$$

And

$$\epsilon = \epsilon_0\epsilon_r, \;\; \epsilon_0\mu_0 = \frac{1}{c^2} \tag{4.17}$$

Where ε_r is the relative static permittivity and c is the light speed in the free space. Equation (4.16) can be reform as:

$$f_c = \frac{nc}{2a\sqrt{\epsilon_r}} \quad n = 1, 2, 3 \ldots. \tag{4.18}$$

which is the familiar result for rectangular waveguides [15].

4.3.2 Cut-off frequency of planar half-mode SIW

In our design, the waveguide has a slot on the top. We can represent the slot by impedance in the transverse resonant circuit (figure 4.26).

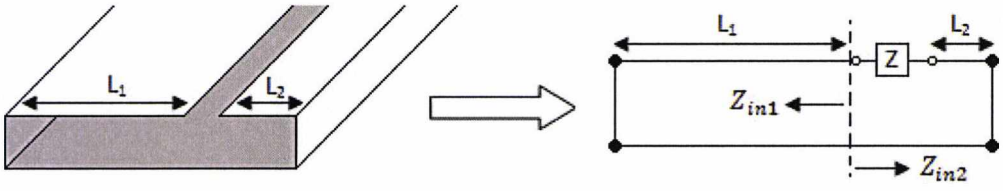

Figure 4.26. The equivalent circuit of planar half-mode SIW

As the slot is quite narrow, it could generally be considered as a capacitor. C is the capacitance value.

$$Z = jX = \frac{1}{j\omega C} \tag{4.19}$$

$$X = -\frac{1}{\omega C} \tag{4.20}$$

Therefore, based on the results above, two impedance expressions are:

$$Z_{in1} = jZ_0 \tan k_x L_1 \tag{4.21}$$

And

$$Z_{in2} = Z + jZ_0 \tan k_x L_2 \tag{4.22}$$

At resonance,

$$Z_{in1} = -Z_{in2} \tag{4.23}$$

This gives:

$$\tan k_x L_1 = -\frac{X}{Z_0} - \tan k_x L_2 \tag{4.24}$$

where $k_x = \omega\sqrt{\mu\epsilon}$, and for capacitor, $X = -\frac{1}{\omega C}$. So

$$\tan \omega\sqrt{\mu\epsilon} L_1 = \frac{1}{\omega C Z_0} - \tan \omega\sqrt{\mu\epsilon} L_2 \tag{4.25}$$

We could solve this equation to determine ω_c, then f_c can be solved.

Now, the characteristic impedance with length of w is:

$$Z_0 = \frac{b}{w}\sqrt{\frac{\mu}{\epsilon}} \tag{4.26}$$

where b is the height of the waveguide and w is its longitudinal length.

If we define C' as the capacitance per unit length, then in a length of w, $C = C'w$. So

$$Z_0 C = C' b\sqrt{\frac{\mu}{\epsilon}} \tag{4.27}$$

Therefore,

$$\tan \omega\sqrt{\mu\epsilon} L_1 = \frac{1}{\omega C' b\sqrt{\frac{\mu}{\epsilon}}} - \tan \omega\sqrt{\mu\epsilon} L_2 \tag{4.28}$$

Let us reorganize the equation.

$$\tan \omega\sqrt{\mu\epsilon} L_1 + \tan \omega\sqrt{\mu\epsilon} L_2 = \frac{\epsilon}{\omega\sqrt{\mu\epsilon} C' b} \tag{4.29}$$

At the cut off, $k_x = \omega\sqrt{\mu\epsilon}$, so the equation can be written as:

$$\tan k_x L_1 + \tan k_x L_2 = \frac{\epsilon}{k_x C' b} \tag{4.30}$$

Let us say the left part is $\tan k_x L_1 + \tan k_x L_2$, and the right part is $\frac{\epsilon}{k_x C' b}$. If we plot the both parts of the equation, the cross point in each region will be the cut off frequency of each mode. Figure 4.27 is an example of this method.

The data used in this example is from the designed planar half-mode SIW. The width of the slot is 0.5mm, L_1 is 15mm and L_2 is 5.5mm. By using the method to measure the capacitance between two metal planes in chapter 2, the slot capacitance C' is calculated as 20.1pF per meter. The rest of the data are constant numbers in different units.

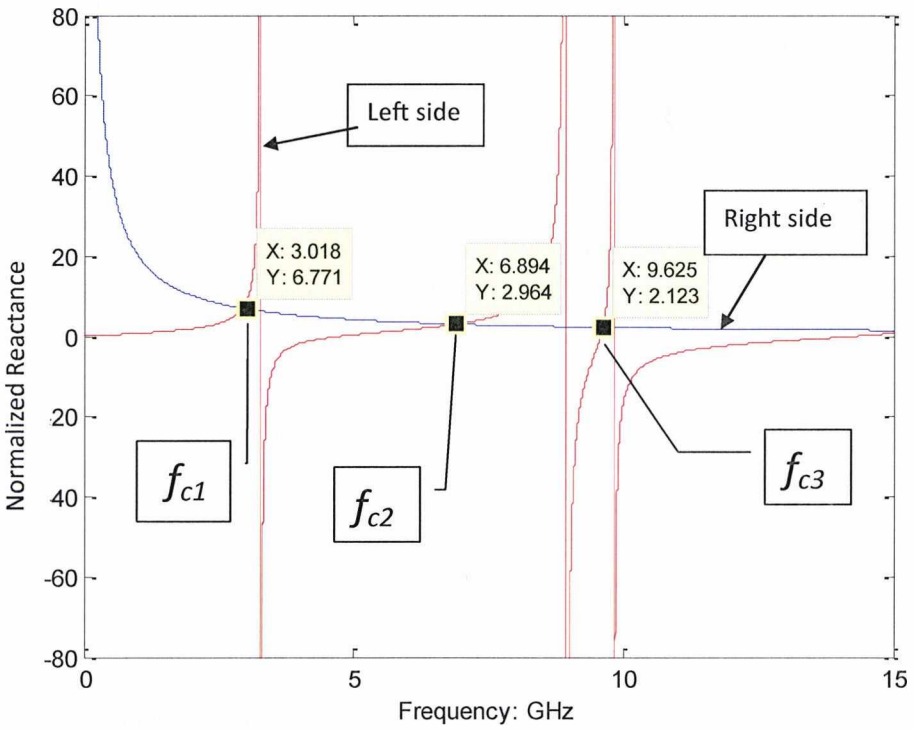

Figure 4.27. Plot of equation (4.30) versus frequency (GHz) in theory

There are two colour lines in the plot, the red one is the left part, which is a typical tangent function; the blue line is the right part. The cross points shown in the plot give the cut off frequency of the different modes. The cross points on the vertical lines of left part are not the real solutions.

The cut off frequency of the fundamental mode f_{c1} is at about 3GHz, f_{c2} is approximately 6.9GHz and f_{c3} is 9.6GHz. Compared with the simulated results in figure 4.13, the cut off frequencies of each mode compared reasonably well. However, the second and third modes have higher cut-off frequencies in the theoretical results. The curves from theoretical equations are very sensitive to the input capacitance and the difference between theoretical and simulated results is due to the value of C'.

4.3.3 Phase constant dispersion curve of half-mode SIW

From the equation (4.30)

$$\tan k_x L_1 + \tan k_x L_2 = \frac{1}{\omega C Z_0} \tag{4.31}$$

Because at the cut-off, $k_x = \omega_c \sqrt{\mu\epsilon}$. The cut off frequency ω_c of each TE mode can be determined by k_x. When we get the value of k_x in each mode, we could plot the phase constant for every mode.

The frequency dependence β can be expressed by

$$\beta = \sqrt{\epsilon_r k_0^2 - k_x^2} \tag{4.32}$$

Where k_0 is the free space wave-number.

$$k_0 = \frac{\omega}{c} = \frac{2\pi f}{c} \tag{4.33}$$

Here c is the speed of light in the free space and f is the operating frequency. Due to the frequency dependent Z, strictly speaking, k_x is not constant and changes by the frequency. However, in the planar half-mode waveguide, the capacitance of the slot is very small, for small C, k_x is almost a constant number.

Take the example of the planar half-mode SIW in this chapter. The slot capacitance is 20.1pF/m. According the results of figure 4.27, we know the cut-off frequencies of each

mode, and then the phase dispersion plot for the waveguide is shown in figure 4.28. The lightline is added. It is clear that the dispersion curves of each mode are all converged to the lightline, and they compare very well with the simulated curves in figure 4.13.

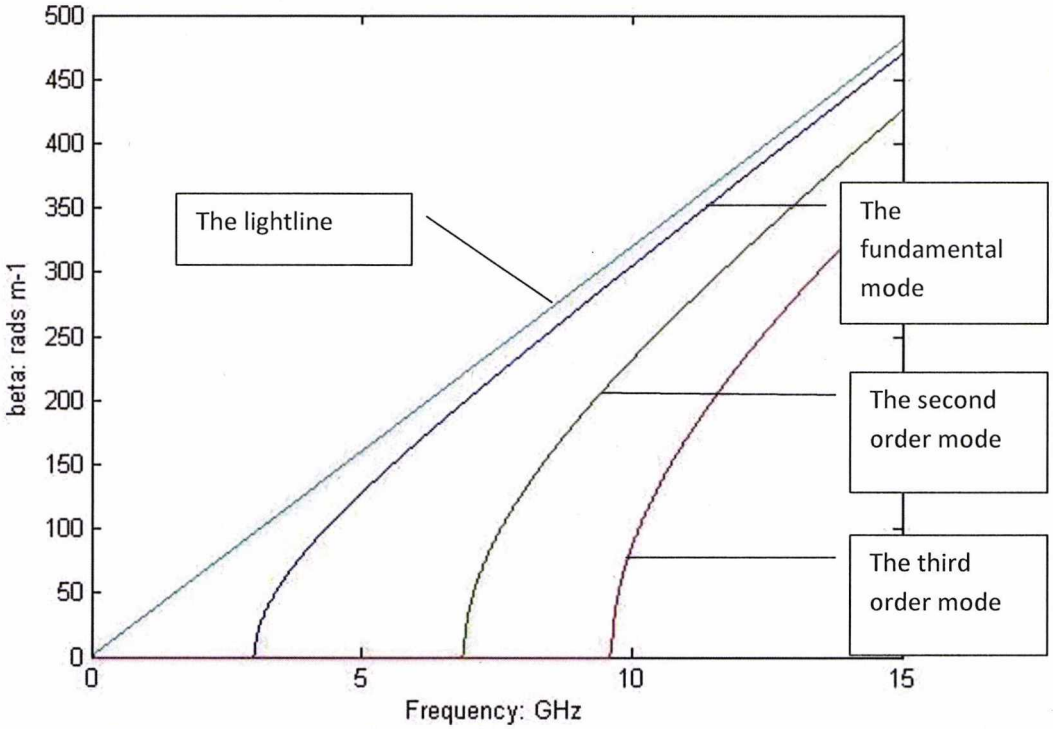

Figure 4.28. Phase dispersion curves of theoretical results

Figure 4.29 shows the field lines of the three modes, and the line colour corresponds to figure 4.28. Actually, the right part (green line shown in figure 4.29) could be considered to support another half mode signals in the waveguide (referred to section 4.1.3).

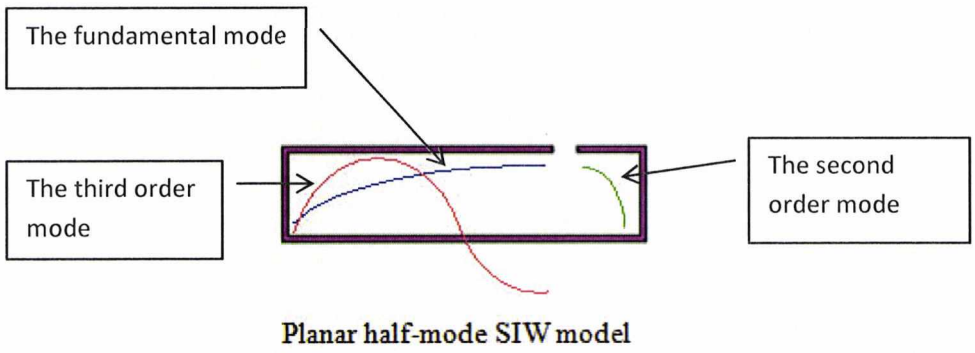

Figure 4.29. E-field trend plots of three modes

4.4 Summary

In this chapter, we introduced a new planar half-mode substrate integrated waveguide. This novel design provides the original propagation characteristics of half guided waves and keeps the advantage of the cross-sectional size reduction, bandwidth enhancement, low cost etc. Furthermore, compared with the conventional half-mode waveguide, the open side is closed, in which case, no radiation loss in our design.

The open slot has been moved to the top layer in our design. We also presented the changes is the loss and bandwidth by changing the slot width and position. This is quite important in the procedures of waveguide design and optimization.

At the end, the transverse resonance technique has been introduced and used in defining the propagation constant and the cut off frequency of the planar half-mode waveguide. This theoretical method can present how the characteristics of the waveguide are affected by loading different components accurately. The theoretical results have great matching with that of simulation and measurement.

References

[1] Qinghua Lai, Fumeaux C., Wei Hong, Vahldieck R., "Characterization of the Propagation Properties of the Half-Mode Substrate Integrated Waveguide," *IEEE Trans. Microw. Theory Tech.*, vol 57, no. 8, Aug 2009

[2] W. Hong, B. Liu, Y. Q. Wang, Q. H. Lai, and K. Wu, "Half mode substrate integrated waveguide: a new guided wave structure for microwave and millimeter wave application," in *Proc. Joint 31st Int. Conf. Infrared Millim. Waves 14th Int. Conf. Terahertz Electron*, pp.219, Sep. 2006.

[3] Wei Ma, Ke Wu, Wei Hong, and Yu-Jian Cheng, "Investigations on Half-Mode Substrate Integrated Waveguide for High-Speed Interconnect Application," *IEEE MTT-S International Microwave Workshop Series on Art of Miniaturizing RF and Microwave Passive Components*, pp. 120 – 123, 2008.

[4] J. F. Xu, W. Hong, H, J. Tang, Z. Q. Kuai, and K. Wu, "Half-mode substrate integrated waveguide (HMSIW) leaky-wave antenna for millimeter-wave applications," *IEEE Antennas and Wireless Propag. Lett.*, vol. 7, pp. 85-88 , 2008.

[5] Qing Hua Lai, Wei Hong, Zhen Qi Kuai, Ying Song Zhang, and Ke Wu, "Half-mode substrate integrated waveguide transverse slot array antennas," *IEEE Trans. Antennas Propag.*, vol. 57, no. 4, Apr 2009

[6] B. Liu, W. Hong, Y.Q. Wang, Q. H. Lai, and K. Wu, "Half mode substrate integrated waveguide (HMSIW) 3-dB coupler," *IEEE Microw. Wireless Compon. Lett.*, vol. 17, no. 1, pp. 22-24, Jan. 2007.

[7] B. Liu, W. Hong, Y. Zhang, H. J. Tang, X. X. Yin, and K. Wu, "Half mode substrate integrated waveguide 180 3-dB directional couplers," *IEEE Trans. Microw. Theory Tech.*, vol. 55, no. 12, pp. 2586–2592, Dec. 2007.

[8] Y. Q. Wang, W. Hong, Y. D. Dong, B. Liu, H. J. Tang, J. X. Chen, X. X. Yin, and K. Wu, "Half mode substrate integrated waveguide (HMSIW) filter," *IEEE Microw. Wireless Compon. Lett.*, vol. 17, no. 4, pp. 265–267, Apr. 2007.

[9] Y. Cheng, W. Hong, and K.Wu, "Half mode substrate integrated waveguide (HMSIW) directional filter," *IEEE Microw. Wireless Compon. Lett.*, vol. 17, no. 7, pp. 504–506, Jul. 2007.

[10] X.-C. Zhang, J. Xu, Z.-Y. Yu, and Y.-L. Dong, "C-band half mode substrate integrated waveguide (HMSIW) filter," *Microw. Opt. Tech. Lett.*, vol. 50, no. 2, pp. 275–277, Feb. 2008.

[11] Cuilin Zhong; Jun Xu; Zhiyuan Yu; Maoyan Wang; Junhong Li, "Half mode substrate integrated waveguide broadband bandpass filter using photonic band gap structures," in *International Conference on Microwave and Millimeter Wave Technology*, pp. 22-24, 2008.

[12] Z.-Y. Zhang and K. Wu, "Broadband half-mode substrate integrated waveguide (HMSIW) Wilkinson power divider," in *IEEE MTT-S Int. Microw.* Symp. Dig., Atlanta, GA, pp. 879–882, Jun. 2008.

[13] Y. Dong and T. Itoh, "Composite right/left-handed substrate integrated waveguide and half-mode substrate integrated waveguide," in *IEEE MTT-S Int. Microw. Symp. Dig.*, Boston, USA, pp. 49-52, 2009.

[14] Lin Sheng Wu, Xi Lang Zhou, Wen Yan Yin, Chun Tian Liu, Liang Zhou, Jun Fa Mao and Hong Li Peng, "A New Type of Periodicly Loaded Half-Mode Substrate Integrated Waveguide and Its Applications," *IEEE Trans. Microw. Theory Tech.*, vol. 58, no. 12, pp. 882-893, Apr. 2010.

[15] David M. Pozar, "*Microwave Engineering*" third edition, John Wiley & Sons, Inc, ISBN 0-471-44878-8

5. Switchable substrate integrated waveguide

The diode control system has been developed since 1955[1]. The diode switch which is one of the most important components in microwave engineering has been widely applied to the radar systems, communication and instrumentation systems, antenna systems etc. The diode switch has the advantage of fast switching time, great isolation period and high power handling capability [2].

The pin diode is an ideal component for signal selection system and can be applied in the switches [3] [4], attenuators [5] [6], photo-detectors [7], limiters [8] and amplifiers [9]. Furthermore, in the digital phase shift area [10], the diode switch is used to toggle the signal between sections of microwave transmission lines [11].

In this section, a novel switch has been presented by embedding pin diodes with the planar half-mode substrate integrated waveguide (HMSIW). This design performs good switching properties, and has achieved >50dB of isolation up to 4GHz.

5.1 Model of the structure and equivalent circuits

5.1.1 Model design

This design is based on the planar HMSIW, which has been introduced in the previous chapter. On the top layer of the planar HMSIW, there is a slim air slot. The slot forms an effective magnetic wall to make the waveguide operate in the half mode. If this slot is shorted, the magnetic wall will disappear and the characteristics of this HMSIW will change to a normal full mode waveguide. Because of the different cut off frequencies of these two kinds of waveguide, there will be an isolation area between two frequencies,

where the HMSIW configuration will propagate but not the full mode. It could be used as a switch. This is the fundamental idea of this chapter.

By using the performance of the pin diode, we can switch between these two configurations. A series of pin diodes can be put on the slot to couple the two parts of the top layer. Then, a power supply can control the working status of the pin diodes. Under the zero voltage condition, pin diodes only have very low capacitances and therefore except very little affect on the half mode transmission. Under the working voltage condition, pin diodes become very good RF conductors and short the air gap to force the waveguide to propagate in full mode configuration. Figure 5.1 shows the model of this design.

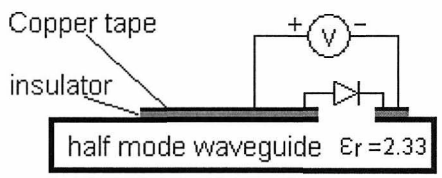

Figure 5.1. Geometry of the switch design

Along the slot, a high temperature insulator is put in order to avoid short circuiting of the bias power supply. The reason of applying the high temperature insulator is to prepare for the solder work on the structure. The diodes are then capacitively coupled to the slot via copper tape plates. Following the right diode bias rule, the power supply connects to the copper tape by using copper wires. A series resistor is put in the circuit, which protects the pin diodes and the power supply. The bias resistance value is 1kΩ.

Infineon BAR64-02V silicon pin diodes are chosen in this design. It is a two pin RF component. The reverse capacitance above 1GHz is very low and the forward resistance is low as well.

5.1.2 Equivalent circuits and components

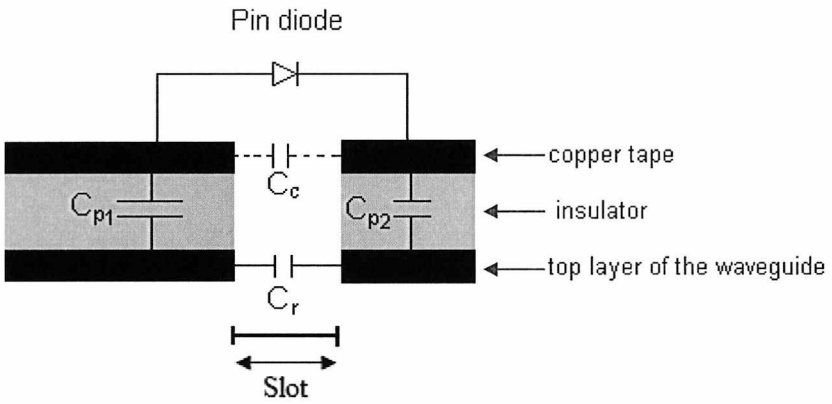

Figure 5.2. Geometry of the circuit components around the slot

An important thing we need to think about is that there will be parallel capacitances C_{p1}, C_{p2} exists in the insulator between the copper tape and the waveguide (figure 5.2). While the pin diode is forward biased, the capacitances in both sides are series coupled. As long as the active values of capacitances are very high, these two capacitors are shorted. In this case, the magnetic wall created by the open slot will disappear, and the E-field distribution will become that of the full mode. To calculate the plate capacitance, we use:

$$C = \frac{\varepsilon_r \cdot \varepsilon_0 A}{D} \tag{5.1}$$

Here ε_r is the dielectric constant of the insulating material, A is the overlapping surface area of the plates and D is the distance between the plates. The permittivity of the insulator ε_r is about 2.1 and its thickness is 60μm in this design. Through the calculation, a size 3mm×3mm copper tape could create 2.66pF capacitance. In the real fabrication, the size may be much bigger, which will create a much larger capacitance.

Another important potential component is the slot capacitor C_r (figure 5.2), which is created by the top two parts of the waveguide. The width of the slot is 0.5mm. However,

the top metallic surface is quite thin and the slot is only an air gap, so the value of capacitance C_r is very low. It is only 20.1 pF/m (result is referred to Chapter 4).

The gap between the copper tapes also may have various low capacitances C_c, which is marked by the dash line in the figure. However, due to the actual PCB fabricating situation, the thickness of the insulator and the copper tape on both sides can not be matched perfectly. Also the value of C_c is very small, and only has little effect on the circuit.

5.2 Analyses of Biased conditions of pin diodes

The equivalent circuit of the pin diode is shown in figure 5.3. In the datasheet of the Infineon BAR64-02V pin diode [12], L is 0.6nH, C_T is 0.2pF, R_P is 3000Ω and R_s is 2Ω. When the pin diode connects to the waveguide, it will combine with the insulator capacitances and the slot capacitance of the waveguide. The impedance of the whole section (figure 5.2) will change based on the different biased condition. By analysing the actual equivalent circuits, it will help us to understand the impedance changes and how the pin diode affects the substrate waveguide.

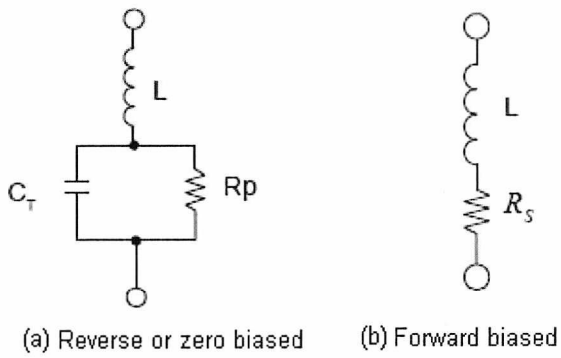

Figure 5.3. Equivalent circuits of the pin diode. (a) reverse or zero biased condition, (b) forward biased condition. (R_P: Reverse parallel resistance; R_S: Forward resistance; C_T: Diode capacitance; L: Forward inductance)

5.2.1 Reverse or zero biased condition

It is well known that the pin diode acts as a low value capacitance C_s when it reverse or zero biased. Considering the capacitance C_r exists in the slot of the waveguide, we could draw a simplified equivalent circuit of one diode section as in figure 5.4.

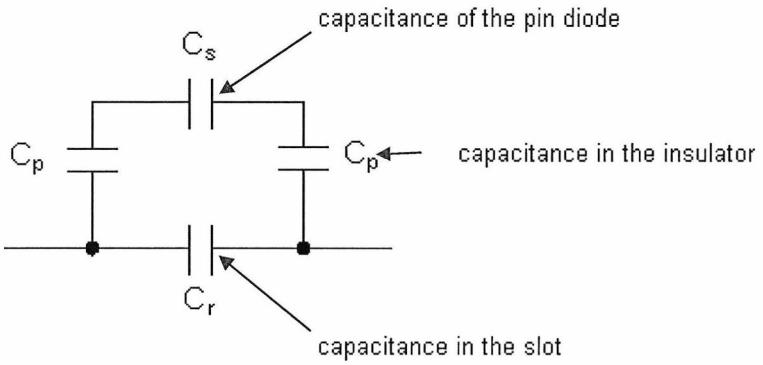

Figure 5.4. Simplified equivalent circuit on the slot under reverse biased condition

The total capacitance C can be written as:

$$C = C_r + (\frac{1}{C_p} + \frac{1}{C_p} + \frac{1}{C_s})^{-1} = C_r + \frac{C_p C_s}{C_p + 2C_s} \tag{5.2}$$

The pin diode has a very low capacitance C_s at zero bias, which is below 0.5pF from the datasheet. The insulator capacitance C_p relates to the size of the copper tape, but definitely the value will be much greater than C_s. So in the case of:

$$C_s \ll C_p \tag{5.3}$$

Therefore:

$$C \approx C_r + C_s \tag{5.4}$$

From the previous chapter, we know that the capacitance in the slot C_r is very small. Therefore, the slot circuit could be considered as a small capacitance when the pin diode is zero biased. It means the waveguide will still remain as a half mode waveguide.

Using the actual equivalent circuit of the pin diode, a more accurate zero biased equivalent circuit of one pin diode section could be drawn in figure 5.5.

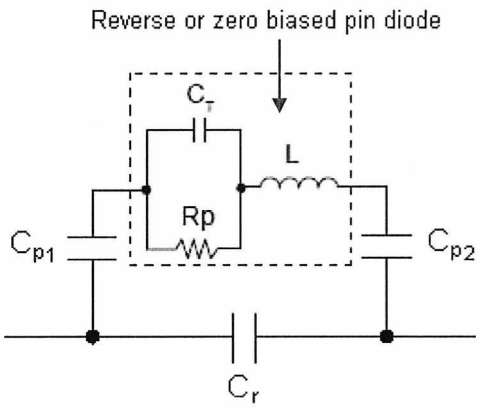

Figure 5.5. Actual equivalent circuit on the slot under the reverse biased condition

With reference to figure 5.5, the total impedance Z across the slot can be written as:

$$Z_1 = \frac{1}{j\omega C_r} \tag{5.5}$$

$$Z_2 = \frac{R_P \times \frac{1}{j\omega C_T}}{R_P + \frac{1}{j\omega C_T}} + j\omega L \tag{5.6}$$

$$Z_3 = \frac{1}{j\omega C_{p1}} + \frac{1}{j\omega C_{p2}} + Z_2 \tag{5.7}$$

$$Z = \frac{Z_1 \times Z_3}{Z_1 + Z_3} \tag{5.8}$$

where

$$\omega = 2\pi f \tag{5.9}$$

We plan to use the Infineon BAR64-02V pin diode in the design. The pin diode has R_P=3000Ω, C_T=0.2pF and L=0.6nH at the reverse biased condition [12]. The C_{p1} and C_{p2}

are much higher, we set more than 10pF for each. With all these values we have, the impedance figure from 1GHz to 6GHz in figure 5.6.

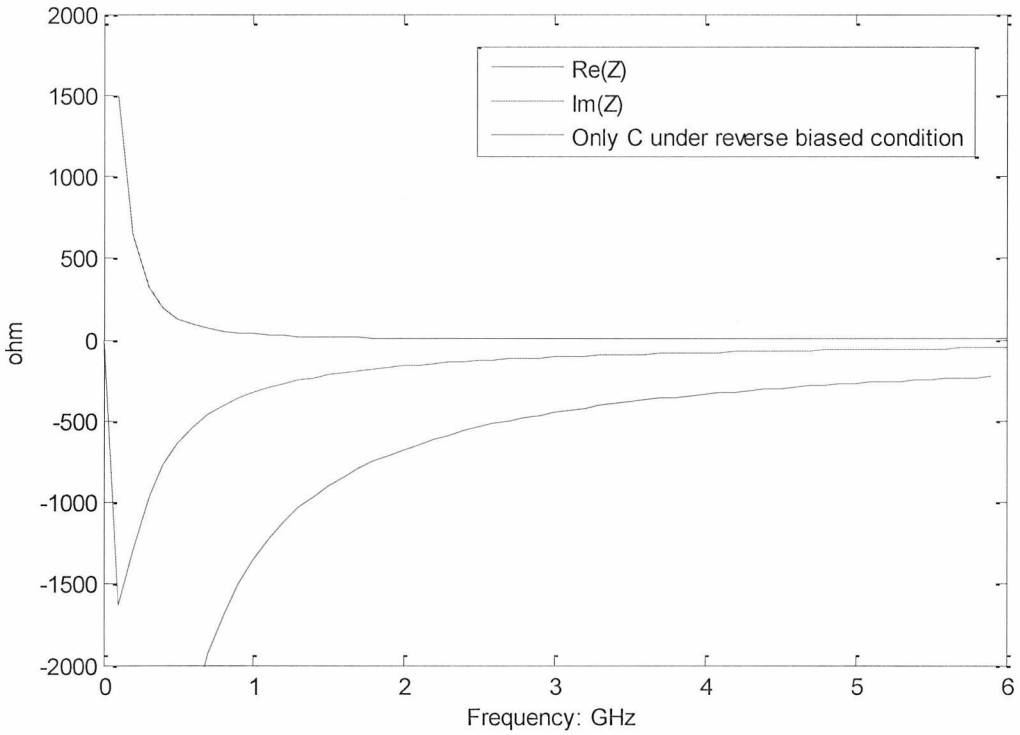

Figure 5.6. The plot of equation (5.8) - Impedance contributions figure under reverse biased condition

The blue line is the real part of Z, and green line is the imaginary part. As the frequency increases, the real part goes down rapidly and nearly reaches zero. In the mean time, the imaginary part reduces as well, but it still has a small negative value at the high frequency. It means that the reversed circuit can be simplified as a small value capacitance, and it will not affect the half mode guide propagation.

In this figure, we also plot the approximate capacitance C of equation (5.4) in theory. This plot does not include any inductance or resistance. In this case, the circuit of the slot is a pure capacitor.

Therefore, when the pin diode is zero biased (off condition), it can be considered as a low capacitance bridge over the gap (figure 5.7). It has very little affect on the half-mode guided waves propagation.

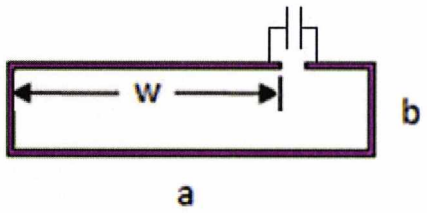

Figure 5.7. Geometry under diode-off condition

As we discussed in chapter 4, the half mode folded waveguide keep half of the original field distribution and the effective width of the waveguide is approximate $2w$. w here is 15mm, and the dielectric constant is 2.33. Thus, under the diode-off condition, the cut off frequency is:

$$f_{c1} = \frac{c}{2a_{eff}\sqrt{\varepsilon_r}} = 3.27GHz \tag{5.10}$$

5.2.2 Forward biased condition

The pin diode will become a good RF conductor when forward biased, and it provides a small resistance. We could assume it turns to a short circuit. A simplified equivalent circuit is created in figure 5.8.

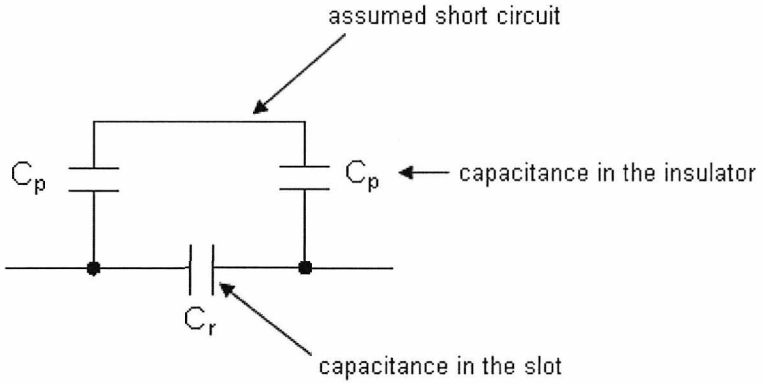

Figure 5.8. Simplified equivalent circuit on the slot under forward biased condition

Hence, the total impedance C is:

$$C = \frac{C_p}{2} + C_r \tag{5.11}$$

C_p is quite large, and the slot can be considered as a short circuit under the forward biased condition. For the whole waveguide, as the gap has been shorted, the guide switches from half mode to full mode.

We can simulate a more accurate equivalent circuit with the actual forward biased circuit of the pin diode. Figure 5.9 shows the circuit mode while forward biased.

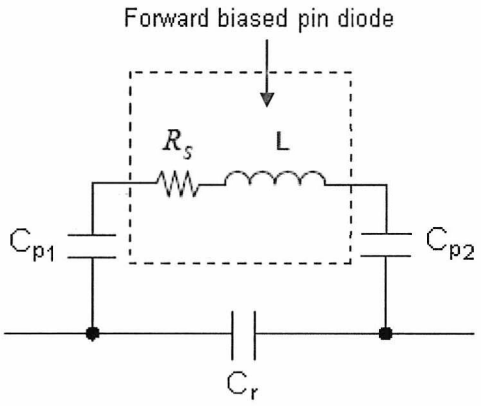

Figure 5.9. Actual equivalent circuit on the slot under the forward biased condition

The total impedance Z can be written as:

$$Z_1 = \frac{1}{j\omega C_r} \tag{5.12}$$

$$Z_2 = \frac{1}{j\omega C_{p1}} + \frac{1}{j\omega C_{p2}} + R_s + j\omega L \tag{5.13}$$

$$Z = \frac{Z_1 \times Z_2}{Z_1 + Z_2} \tag{5.14}$$

At the forward biased condition, the series R_s is about 2Ω and L is 0.6nH. C_{p1}, C_{p2} keep the same values. The impedance Z plot is shown in figure 5.10.

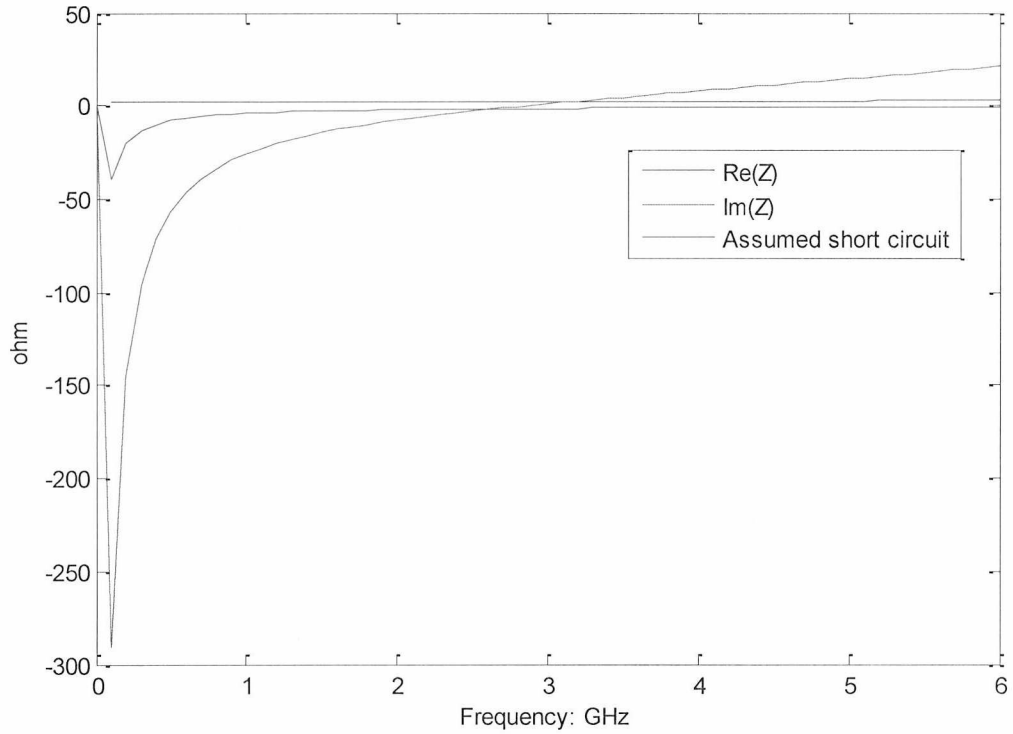

Figure 5.10. The plot of equation (5.14) - Impedance contributions figure under forward biased condition

The real part of impedance Z is the blue line. It has a constant small value in the frequency range. The imaginary part (Green line) has a negative value before 3GHz, and then turns to a positive value. Therefore, the equivalent components in the circuit after 3GHz could be considered as a small resistor and an inductor. In this case, above 3GHz, the diode section works as a short circuit over the slot.

There is another red line in the figure, which shows the approximate calculation in equation (5.11). As the frequency increases, it turns to zero very rapidly.

Therefore, when the pin diode is forward biased (on condition), it becomes a good RF conductor (figure 5.11) and effectively shorts the top layers. It makes the gap closed and the waveguide propagates in the full mode.

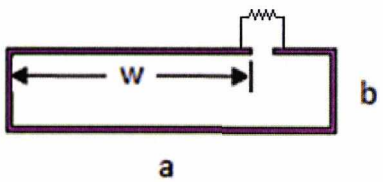

Figure 5.11. Geometry under diode-on condition

Therefore, the effective width of the waveguide is a. Here a is 21mm, so under the forward biased condition, the cut off frequency is:

$$f_{c2} = \frac{c}{2a\sqrt{\varepsilon_r}} = 4.68GHz \tag{5.15}$$

Theoretically, the isolation frequency range should be:

$$f_{c2} - f_{c1} = 1.41GHz \tag{5.16}$$

5.3 Simulations

We use the silicon PIN diode (BAR64-02V). The diode capacitance at 0V is 0.2pF; the forward resistance is about 2Ω at the high voltage and the series inductance is 0.6nH.

In HFSS, we set the design into a perfect situation without dielectric and conductive losses. We defined the lumped RLC boundary condition in the slot of the top layer (figure 5.12). Then, we could simulate the different diode status by changing the type of the boundary condition.

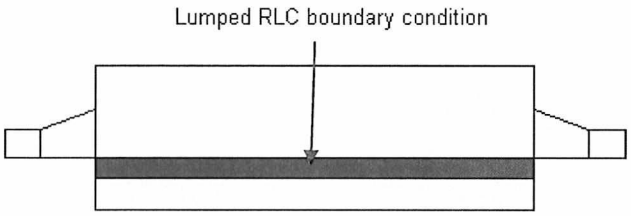

Figure 5.12. Lumped RLC boundary condition (HFSS)

5.3.1 Reverse or zero biased condition result

The equivalent circuit of the pin diode shows that there is always a series inductance. We assume that the diodes are pure capacitances under zero biased, and the boundary we set includes the capacitance and the inductance.

The diode capacitance at 0V and the inductance are applied to the condition. Based on the dimensions of the structure, we set C_T=0.2pF (1.7pF/m) and L=0.6nH (0.072nH•m). There is also a reverse resistance R_s=3000Ω (360 Ω•m). Figure 5.13 shows the S parameter results. From the results, the cut off frequency is still around 3GHz, and the return losses are all below -20dB in the fundamental mode.

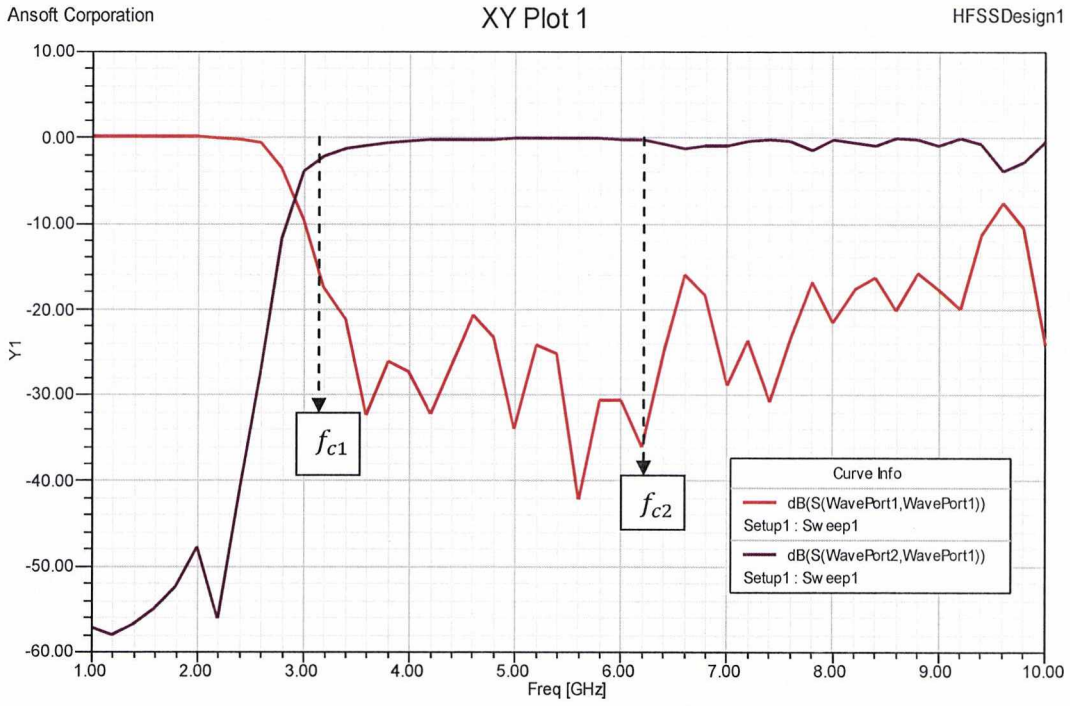

Figure 5.13. Simulated S parameters (dB) under reverse or zero bias condition

5.3.2 Forward biased condition result

Under forward biased, we assume the diodes are low value resistors. The boundary only has the resistance and the inductance.

When the voltage is added to the pin diode, it turns to the *R*, *L* condition. We set the forward resistance R_s=2Ω (0.24Ω•m) and *L*=0.6nH (0.072nH•m). Figure 5.14 shows the simulation results. It is clear to see that the cut off frequency increase to 4.9GHz. Actually, the propagation starts at about 4.6GHz, at which point the S11 already begins to go down. The insertion loss is a little higher than the *C*, *L* condition. That is mainly caused by the resistance of the diode. Over 3~4.6GHz ranges, the isolation is mostly above 50dB.

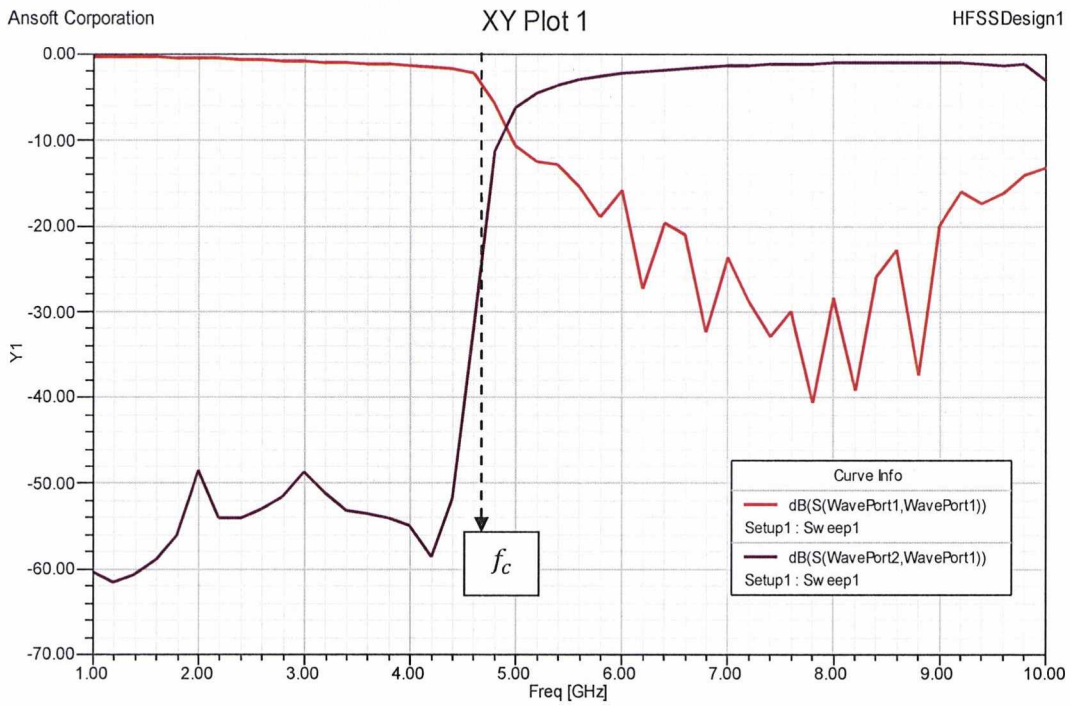

Figure 5.14. Simulated S parameters (dB) under forward bias condition

5.4 Design with Continuous copper plane and measurements

We designed the pin diode switch with a continuous copper tape plate first. We use two pieces of copper tape to cover the top layer except the slot. Above that, six pin diodes are soldered on the copper tape at a spacing of 2.5mm. Figure 5.15 shows the picture of this design.

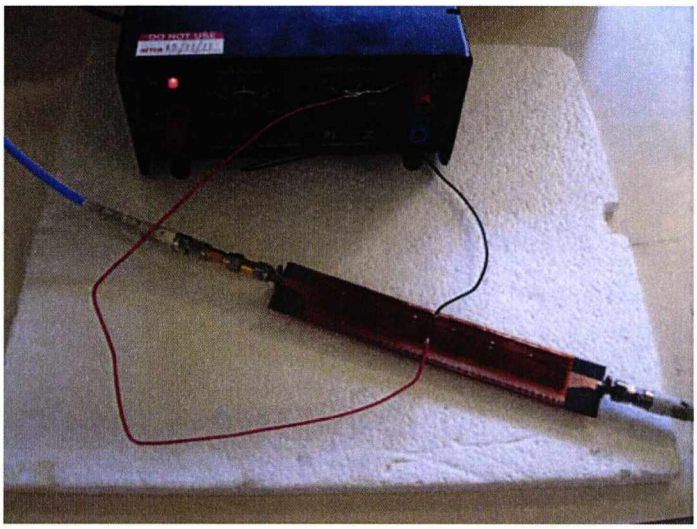

Figure 5.15. The picture of design with Continuous plate

We use the Anritsu 37397C vector network analyzer to measure the structure. The pin diodes are controlled by a dual 35V power supply.

Figure 5.16 shows the S parameter results, when the diodes are reverse biased.

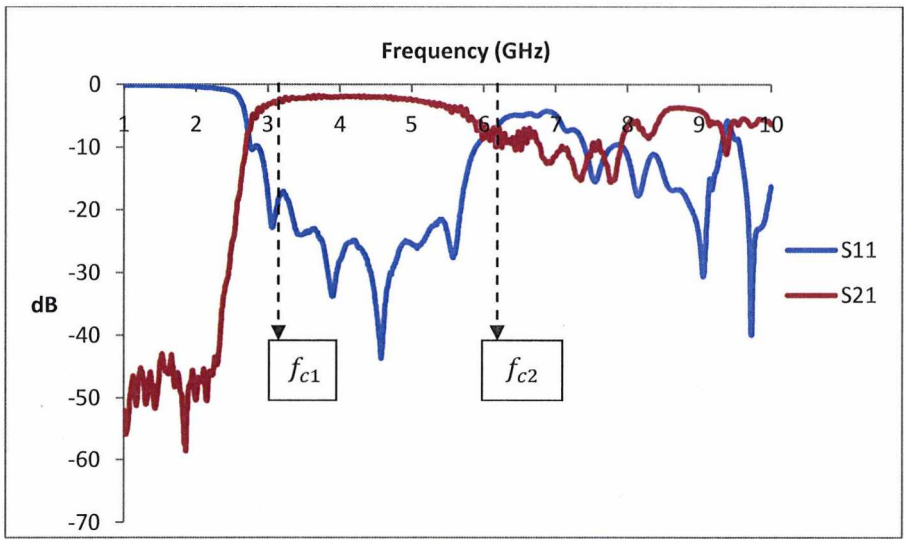

Figure 5.16. Measured S parameters under reverse biased condition

Figure 5.17 shows the S parameter results, when the diodes are forward biased.

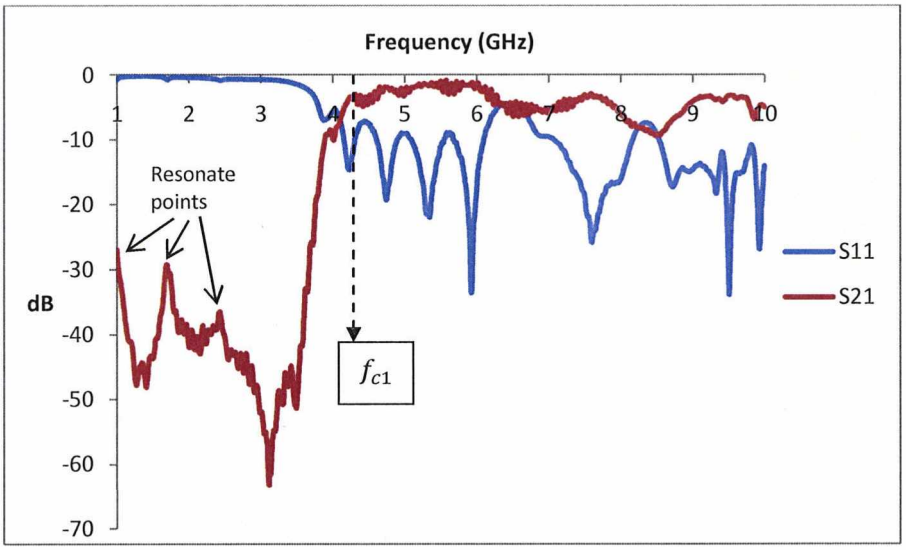

Figure 5.17. Measured S parameters under forward biased condition

In this case, the cut off frequency has been pushed up to about 4.2GHz. The return loss is below -10dB in the fundamental mode.

This structure generally follows the purpose of our design. However, this is not the ideal situation we expected. Firstly, there are a few resonant points in the isolation area, which are shown in figure 5.17. Secondly, the isolation range is shorter than the calculation result. Additionally, a great deal of noise is present on the S_{21} plot.

The resonance is caused by the length of copper tape. If the length of the copper tape is larger than $\lambda/2$ of the waveguide, it can cause resonance in the insulator. This can be solved by reduce the size of the copper tape.

The noise can be reduced by adding inductors in the bias circuit. After lots of improvements, finally we achieve our design with discontinuous copper tape.

5.5 Improved design with discontinuous copper tapes and measurements

5.5.1 Model design and fabrication

Figure 5.18 shows the top view of the final design with discontinuous copper tape. In this figure, there are four sets of the copper tape in the centre. On each set, there are three diodes.

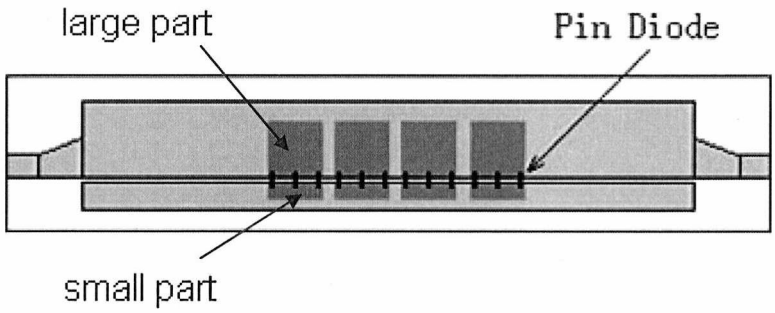

Figure 5.18. Geometry of the design with discontinuous tapes biased

There are two copper parts in each set. The area of the large plate is 7.5mm×9mm, and the small plate is 7.5mm×3mm. The distance between each set is 2.5mm. The distance between each diode is also 2.5mm. The whole structure is symmetrical on the top of the waveguide.

By using the formula (4.1), the values of two parallel capacitances can be calculated approximately. The C_{p1} at the large part is 19.9pF and C_{p2} at the small part is 6.64pF. Both of them are quite large capacitances. While the pin diodes are forward biased, C_{p1} and C_{p2} are shorted.

The length of each copper tape is 7.5mm, which is much shorter than $\lambda/4$ at the middle frequency. This will avoid the resonance when the diodes are switched on. To reduce the noise, the ferrite chokes are soldered at the end of the copper wire. See figure 5.19. The dominate part of this design is much smaller than the previous one (only takes 1/3 length of the waveguide). On each copper set, we have the ferrite choke to connect the biasing wire.

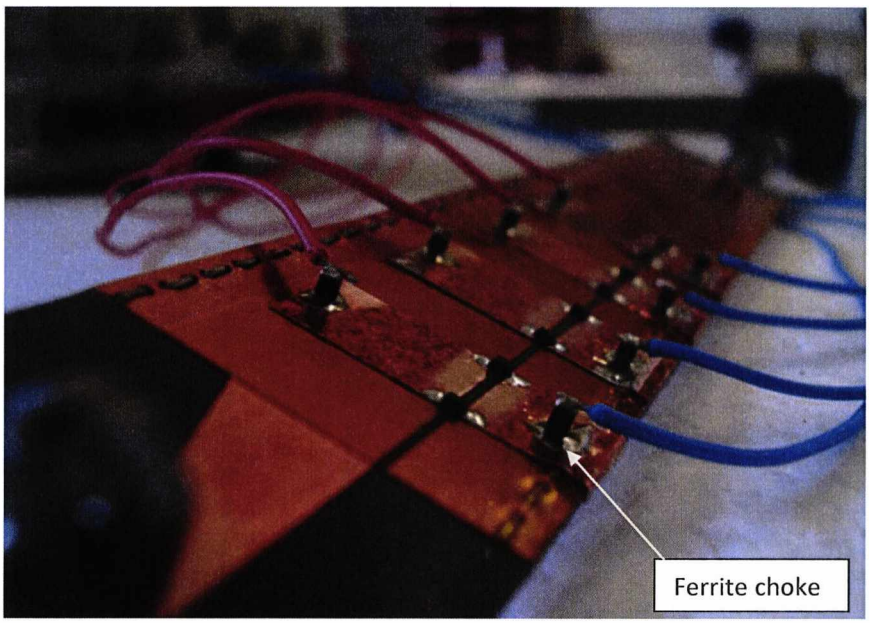

Figure 5.19. Solder work with ferrite chokes

We use the traditional PCB fabrication technique to manufacture the structure in the workshop. The insulator and the copper tape have sticky sides, which is the benefit of easy reconfiguration. Figure 5.20 shows the final structure.

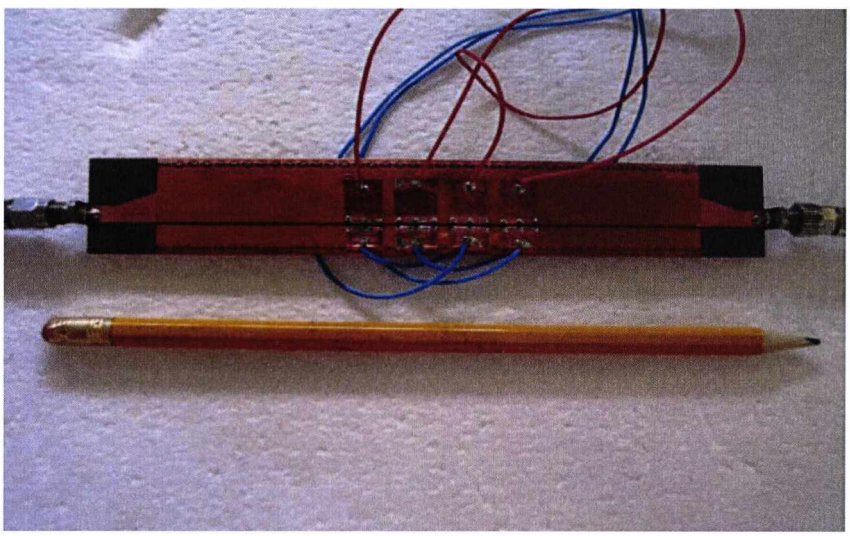

Figure 5.20. The picture of the structure

5.5.2 Measurements

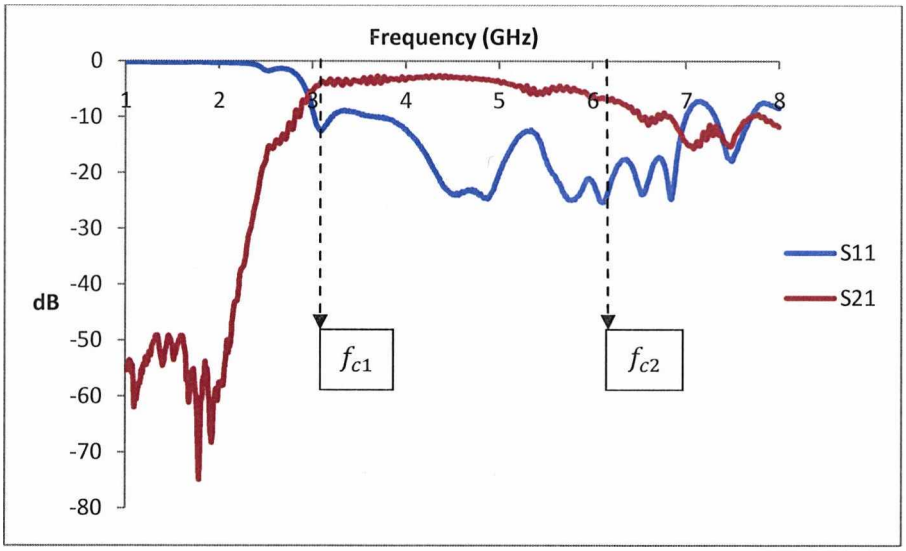

Figure 5.21. Measured S parameters under reverse biased condition

Under reverse biased condition, measured S parameters are shown in figure 5.21. The cut off frequency is at about 3.2GHz, which is approximately the same as the planar HMSIW. The S_{21} works well in the fundamental mode with some losses. After 6GHz, S_{21} is affected by the higher mode propagation.

The S_{11} is below -10dB at 3~4GHz range, and then goes down to below-20dB until 5GHz. The insertion loss is about 3dB in the whole fundamental mode range. The main reason for the increase in the loss is because of the resistance of the pin diodes. A further discussion about the loss will be shown in the next section.

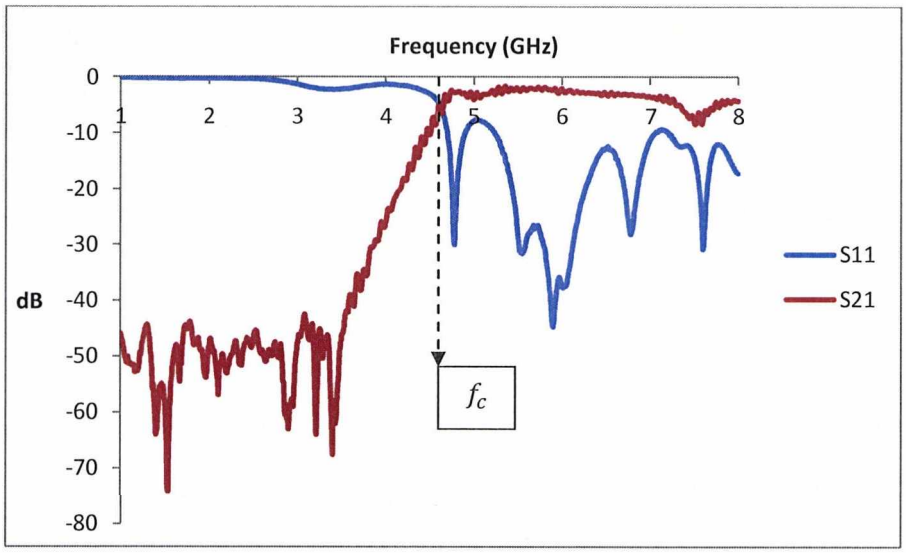

Figure 5.22. Measured S parameters under forward biased condition

When the pin diodes are forward biased, measured S parameters are shown in figure 5.22. The cut off frequency is increased to 4.6GHz. The measured result shows a very good agreement with the calculation. Compared with the first design, the resonance points have disappeared at the low frequency. Before 4GHz, the isolation are all below -40dB, which is necessary for a switch.

The S_{11} is below -10dB, and from 5.4GHz to 6.5GHz, it goes down below -20dB. The insertion loss is about 2~3dB.

We put the S_{21} under different biased conditions together. Figure 5.23 shows the comparison. The design has achieved -40dB of isolation up to 3.7GHz. The resonance has disappeared and the noise reduced. The switching range is up to 4GHz.

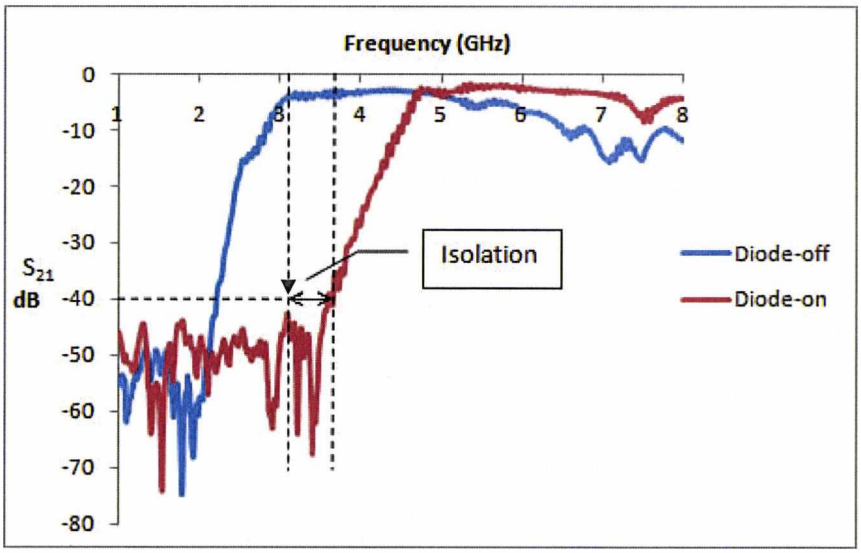

Figure 5.23. Comparison of measured S_{21} between reverse and forward biased conditions

5.5.3 Losses

From the S parameters of the measurements, we realize that the insertion loss increased if we add the diodes on the waveguide. Furthermore, under different biased conditions, the losses vary. Figure 5.24 shows the plots of the insertion losses in different conditions of the guide.

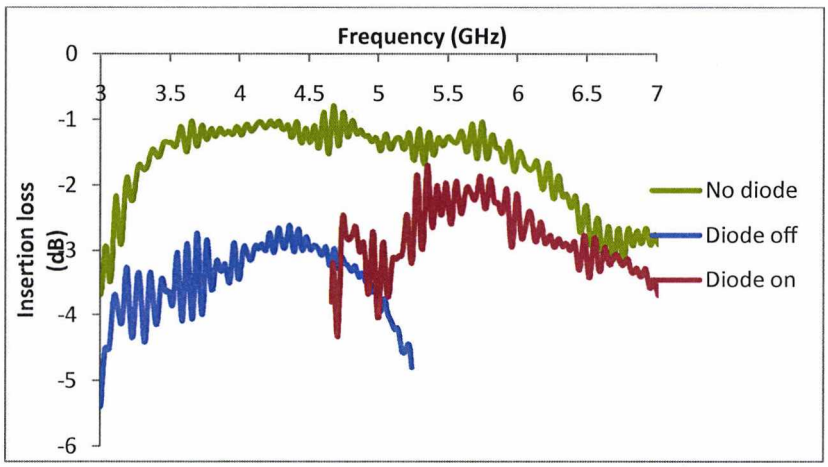

Figure 5.24 Comparison of measured insertion losses under different conditions

The green line shows the loss when there is no diode on the planar HMSIW. This loss includes the dielectric and conductive loss, and it has average -1.5dB insertion loss in the fundamental mode. The loss increases as the frequency increases.

The blue line shows the insertion loss when the diodes are reverse biased (off condition) and it is about -3~4dB. The red line shows the insertion loss when the diodes are forward biased (on condition), and it is about -2~3dB. In both conditions, it has not only the dielectric and conductive loss, but also the diode resistance and insulating loss.

Also we found that the loss under forward biased condition is larger than that of reversed biased. One possible reason is that when diodes are active, the resonant loss may occur among the diodes by the operating current.

There is no radiation loss in these three conditions (referred to chapter 4), and the crude fabrication technique can cause more loss. Figure 5.25 shows the HFSS results of the attenuation constants in different conditions. It matches well with the measured one.

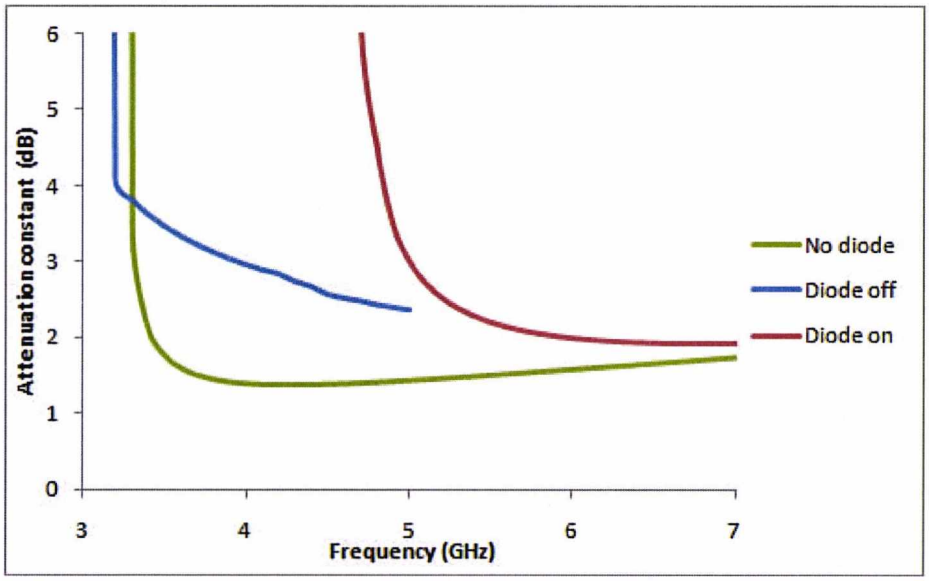

Figure 5.25. Comparison of simulated attenuation constants (dB) under different conditions

5.5.4 An analysis for the different number of copper tapes

In the design above, there are four copper tapes on the top of the waveguide. In the measurement, those tapes are connected to the power supply at the same time. If we choose different number of the tapes to switch on each time, for instance, only connecting one tape at the first time and two tapes at the second time, the active length of the structure will be different (referred to figure 5.20). If we plot the S_{21} parameters of every change, the affect near cut-off is shown in figure 5.26. It is clear to see that as the number of the tapes increases, the angle φ will become smaller.

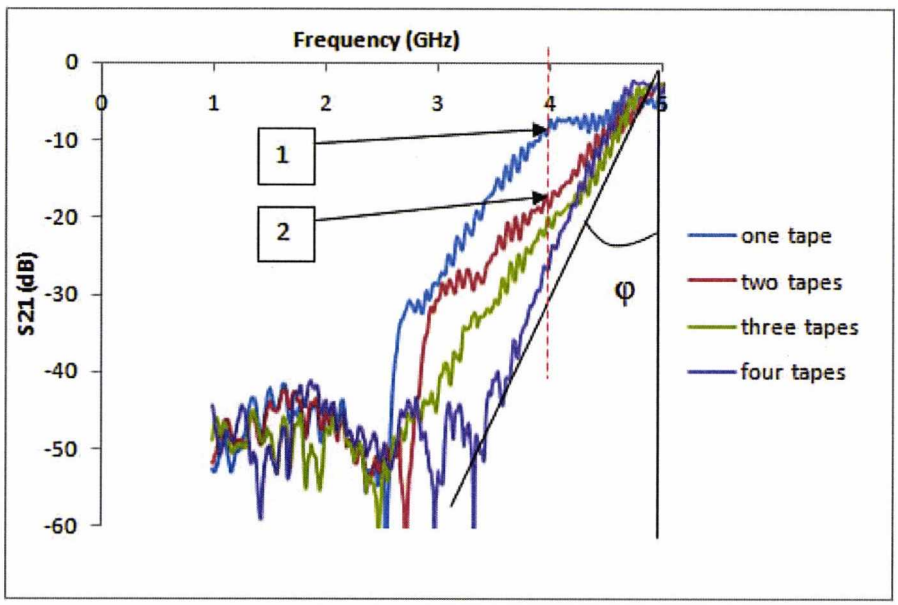

Figure 5.26. The curves of S_{21} below cut-off frequencies with different tape numbers

This figure shows the loss in dB before the cut off. The attenuation constant below cut off expressed as loss is:

$$Loss = e^{-\alpha l} \tag{5.17}$$

Where we assume each tape has the length of l. Transfer the loss to dB/m expression is:

$$Loss(dB/m) = 20\log_{10} e^{-\alpha l} = -8.686\alpha l \tag{5.18}$$

Therefore, if the length *l* becomes double, the loss will be double. At 4GHz, the loss of point 2 is approximately -20dB which is the double value of point 1, which is -10dB.

5.6 Summary

The diode switch is applied widely in the microwave signal selection area. In this chapter, a novel pin diode switch has been presented. The device is based on the planar half-mode substrate integrated waveguide. The propagating mode of the waveguide can be switched between two types of mode via the biasing of integrated pin diodes.

We analyze the affects of the equivalent circuits to the waveguide by changing the diode biased condition. Although the design with continuous plate achieves the frequency switching, we improve the structure by using discontinuous copper tape to remove the resonance. In the range of 3.2 ~3.7 GHz, the isolation is approximately 40dB.

The loss has been discussed. The insertion loss increased while the diodes are added and it attributes to the dielectric loss of the top insulator and the diode resistance. The affect of diode numbers was also discussed in the end.

This work has been accepted by IEEE microwave wireless component letter.

References

[1] Rober V. Garver, "*Microwave Diode control Devices*", Artech House, Inc, 1976.

[2] Egor Alekseev, Delong Cui, and Dimitris Pavlidi, "Power-Handling Capability of W-Band InGaAs Pin Diode Switches", *10th Intern. Conf. on Indium Phosphide and Related Materials*, pp. 199 – 202, May 1998.

[3]Chang B.C.C., Qian. Y., Itoh, T., "A reconfigurable leaky mode/patch antenna controlled by PIN diode switches ," *IEEE Antennas and Propagation Society International Symposium*, vol. 4, pp. 2694-2697, 1999.

[4] Sang Won Yoon, Le Huu Truong, Hyun Seok Lee, Park, E.J., Hyung Moo Park, Jin Koo Rhee, Hyun Chang Park, "UWB antenna with frequency diversity characteristics using PIN-diode switches", *11th International Conference on Advanced Communication Technology*, vol. 1, pp. 344 – 346, 2009.

[5] K. Kobayashi, A.K. Oki, D.K. Umemoto, S. Claxton and D.C. Streit, "GaAs HBT PIN diode attenuators and switches ", *IEEE Microwave and Millimeter-Wave Monolithic Circuits Symposium*, pp. 151 - 154, 1993.

[6] Byung-Jun Jang, "Voltage-controlled PIN diode attenuator with a temperature-compensation circuit," *IEEE Microw. Wireless Compon. Lett.*, vol. 13, no. 1, pp. 7-9, 2003.

[7] Ciric M., Friese J., Korner H.J.and Maier M.R., "Low cost pulse shaper for use with silicon PIN diodes," *IEEE Nuclear Science Symposium and Medical Imaging Conference*, vol.1, pp. 372 – 374, 1992.

[8] Koreyasu M., Takashima T. and Kashiwa T., "X-band PIN Diode Limiter with Low Spike Leakage Performances using Re-entrant Coaxial Cavity," *EuMC 2008 38th European Microwave Conference*, pp. 1735 – 1738, 2008.

[9] Kobayashi K.W., Oki A.K., Tran L. and Streit D.C., "A novel baseband-1.5 GHz monolithic HBT variable gain amplifier with PIN diode gain control ," *IEEE MTT-S International Microwave Symposium Digest*, vol. 1, pp. 201-204, 1995.

[10] Z. Jin, S. Ortiz, and A. Mortazawi," Design and performance of a new digital phase shifter at X-band," *IEEE Microwave Wireless Comp. Lett.*, vol.14, no.9, pp.428-430, 2004.

[11] S. Eom, "Broadband 180^0 bit phase shifter using /2coupled line and parallel /8 stubs," *IEEE Microwave Wireless Comp. Lett.*, vol. 14, no. 5, pp. 228-230, 2004.

[12] http://www.farnell.com/datasheets/81435.pdf

6. Theoretical analyses and applications of circuits with loaded components

In the first part this chapter, the transverse resonance technique (TRT) is used to analyze the planar half-mode substrate integrated waveguide (SIW) with embedded components. Lots of the studies based on the full-mode SIW integrated with periodic components are proposed [1] in antennas [2]-[5], filters [6]-[8], transverse electromagnetc (TEM) waveguides [9], metamaterial structures [10], miniaturized waveguides and antennas [11] [12], high quality resonators [13] [14], etc. However, the research for integration of half-mode waveguide is rare [15] [16]. Till now, very little theoretical method has been developed to simulate the characteristics of the guided modes. We introduce the mathematics model to get the affects of non-periodic and periodic loaded components. The theoretical and measured results have been presented.

In the second part, the applications of non-periodic loaded capacitance and periodic loaded varactor diodes are introduced. Finally, a novel phase shifter is presented that is shown to have up to 60 degrees phase shift in the 5.3 – 6 GHz range with insertion loss better than 3 dB and return loss generally better than 20 dB.

6.1 Embedding components with planar half-mode SIW

In this section, we will try to change the performance of the half-mode substrate integrated waveguide by adding different components along the slot of the top layer of the SIW. The expression of the phase constant can be written as: $\beta = \sqrt{\epsilon_r k_0^2 - k_x^2}$, where due to the frequency dependent loading impedance, k_x is a function of frequency.

From the Chapter 4, we consider a SIW with a slot that is loaded with an impedance Z. The equivalent transverse resonance circuit mode is shown in figure 6.1.

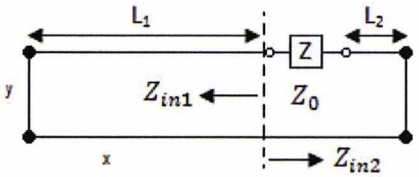

Figure 6.1. The equivalent transverse resonance circuit

And the resonance condition we need satisfy Z_{in1}=Z_{in2} [17], which is:

$$jZ_0 \tan k_x L_1 = -(Z + jZ_0 \tan k_x L_2) \tag{6.1}$$

When considering TE problems using the transverse resonance technique the characteristic impedance is given by $Z_0 = E_y/H_z$ [17] and the equivalent voltage and current are set equal to the electric and magnetic fields respectively. However, because we will later embed discrete components into the waveguide we need to ensure that the equivalent waveguide voltage and current value (and therefore Z_0) are compatible with the voltage and current presented to the embeded impedance Z. If the electric field is independent of y then the voltage at the impedance will be $E_y b$, where b is the height of the waveguide. The surface current density (per unit length) at the embedded impedance is $J_x = H_z$. Hence we choose

$$Z_0 = \frac{bV}{I} \tag{6.2}$$

Therefore, above cut-off

$$Z_0 = \frac{b\omega\mu}{k_x} \tag{6.3}$$

where k_x is now unknown, b is the height of the waveguide. As we have introduced, at the resonant point of our new waveguide,

$$\tan k_x L_1 + \tan k_x L_2 = \frac{1}{\omega C Z_0} \tag{6.4}$$

must hold, where C is the capacitance per unit length,

Hence

$$\frac{1}{\omega C Z_0} = \frac{k_x}{\omega^2 \mu b C} \tag{6.5}$$

and we set

$$\theta = k_x L_1, \qquad T = \frac{L_2}{L_1} \tag{6.6}$$

here $L_2 < L_1$, thus $T< 1$.

If we let

$$N = -\frac{1}{\omega^2 \mu b L_1 C} \tag{6.7}$$

Then equation (6.4) becomes:

$$\tan\theta + \tan T\theta = -N\theta \tag{6.8}$$

Our task, therefore, is to solve for θ (and thus k_x) for a given frequency ω.

6.1.1 Solutions of propagation modes

Figure 6.2 shows plots of the left and right hand side of equation (6.8). In this figure, the red line is the left part ($\tan\theta + \tan T\theta$); and the blue line is the right part ($-N\theta$). The x axis is theta (θ).

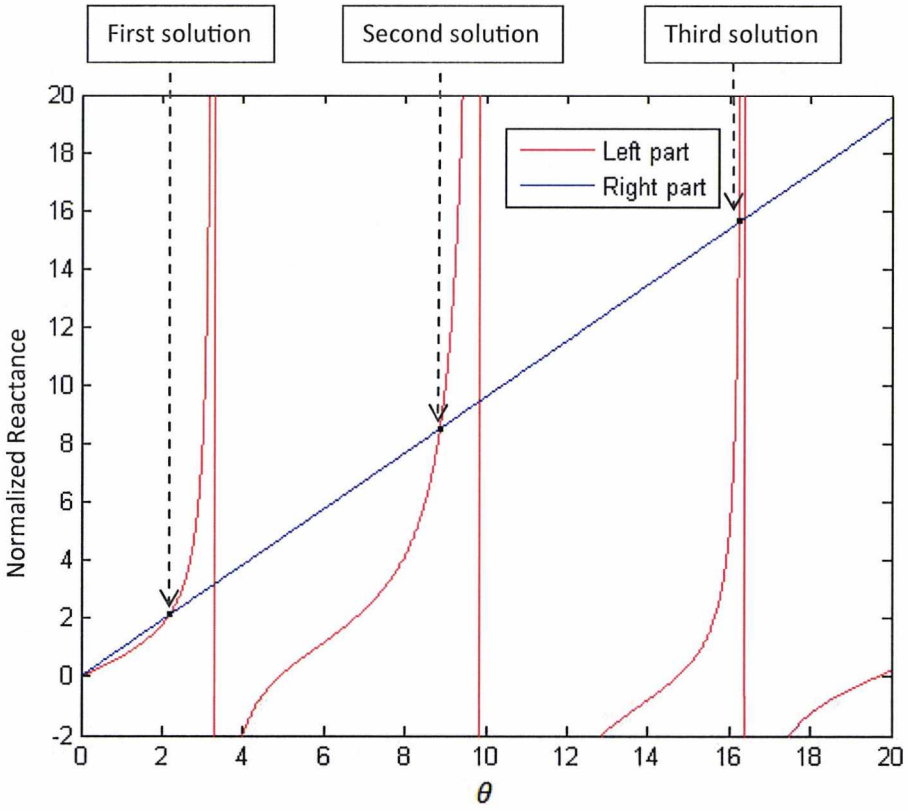

Figure 6.2. Plots of the equation (6.8) with the first solution

We see that, as expected, there are a number of solutions to equation (6.8) (modes). The first solution only occurs if $-N$ is sufficiently large. In the figure, we can see that the slope of the $-N\theta$ line will become small if $-N$ is small. The value of $-N$ is determined by C, which is the capacitance per unit length. It means if the capacitance we add on the half-mode SIW is too large, the fundamental mode will disappear; and when we decrease the capacitance, the fundamental mode will come back.

At the fundamental mode, the value of the x axis, which is θ, is quite small. So for the small θ, we can approximate $\tan\theta$ as:

$$\tan\theta \approx \theta \tag{6.9}$$

So the left part of equation (6.8) is:

$$\tan\theta + \tan T\theta \approx \theta + T\theta = \theta(1+T) \tag{6.10}$$

If we want to have the first cross point in the figure, this condition needs to be satisfied:

$$\theta(1+T) < -N\theta \qquad (6.11), which\ is \quad -N > 1+T \tag{6.12}$$

Substituting (6.6) and (6.7) into (6.12), we get

$$C < \frac{1}{\omega^2 \mu b(L_1 + L_2)} \tag{6.13}$$

Therefore, the fundamental mode only occurs under a limited capacitance range. If the capacitance is above this value, we will not have the first root (figure 6.3).

For the half-mode SIW we designed, T=1/3. Thus if we let $-N = 1$ which is less than 1+T, in this case, there will have no root for the fundamental mode. Figure 6.3 shows the example plot without the first solution.

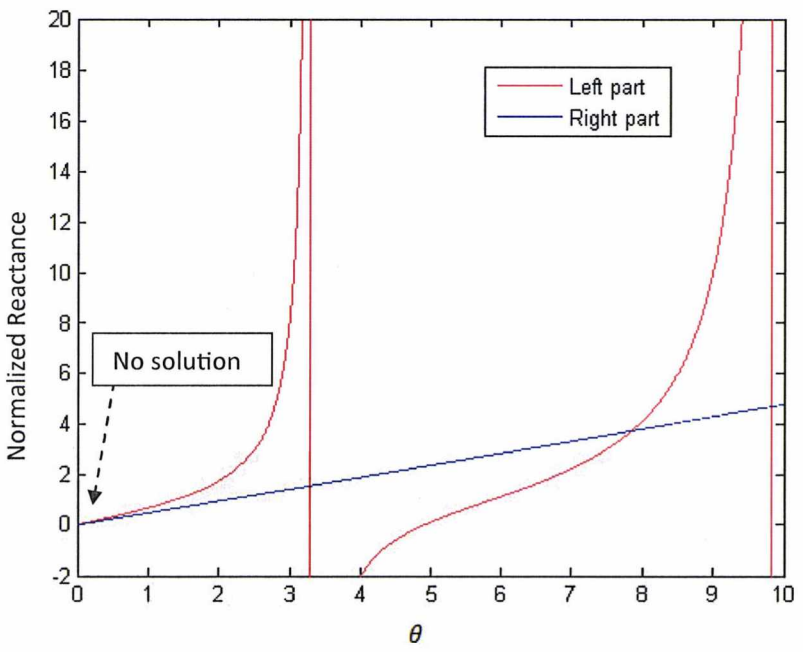

Figure 6.3. Plot of equation (6.8) without the first solution

In HFSS, the lumped RLC boundary is set by different capacitance values to verify with the theoretical results.

This is the phase dispersion figure and E-field distribution of small capacitance applied on the slot. The operating frequency is 10GHz for the field plot.

Under the small capacitance case, the fundamental mode keeps the half-mode performance according to the port E-field plot. The higher order mode is like the TE_{20}. These two modes match with the two roots in figure 6.4.

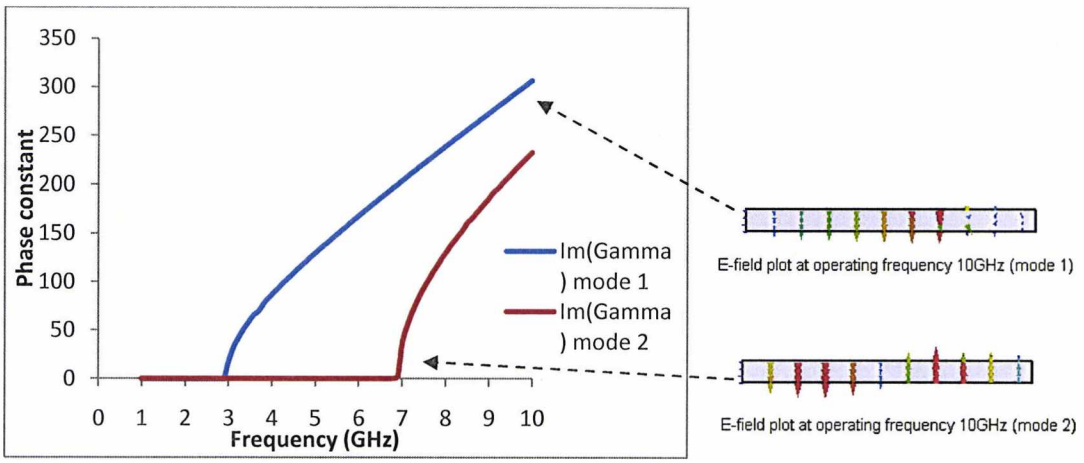

Figure 6.4. Phase constant dispersion curves and E-field plots with the first solution

Under the large capacitance, the waveguide will lose the half-mode transmission, and at the low frequency, the electric field has a maximum around the slot. As the frequency increases, only the full-mode transmission occurs. Thus, in this case, the condition (6.13) is not met then the first mode occurs in the higher order mode range (figure 6.5).

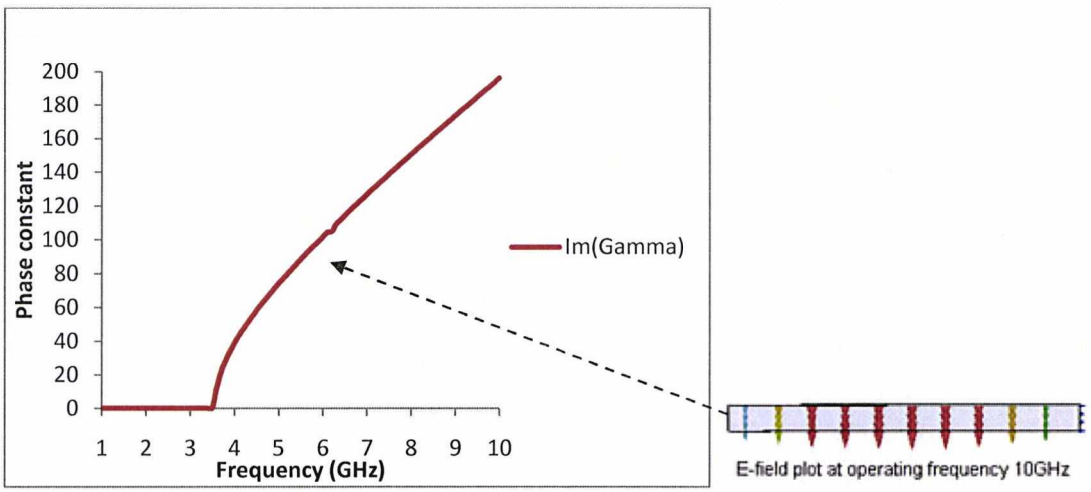

Figure 6.5 Phase constant dispersion curves and E-field plots without the first solution

6.1.2 Fast and slow mode propagations

In figure 6.1, if $\gamma_x$is the propagation constant in the x direction, $\gamma_x = \alpha_x + jk_x$. It leads to two types of propagation which can be categorised as fast and slow modes, where fast and slow are defined with respect to the velocity of propagation in the substrate material.

For fast mode propagation, $\gamma_x = jk_x$ is the priority and α_x becomes the loss part. In fast mode propagation, the field varies sinusoidally across the waveguide cross section, as is the case in conventional waveguide. Referred to the chapter 4, it is easy to determine, where the solutions lie by solving:

$$\tan\theta + \tan T\theta + N\theta = 0 \tag{6.14}$$

where we let $\theta = k_x L_1$.

The phase constant is related to k_x:

$$\beta = \sqrt{\epsilon_r k_0^2 - k_x^2} \tag{6.15}$$

The slow mode propagation is another class of solution that is unusual. For slow mode propagation, $\gamma_x = \alpha_x$ is the priority and jk_x becomes the loss part. Then the fields will vary as combinations of exponential functions. Under this condition equation (6.14) becomes:

$$\tan(-j\theta') + \tan(-jT\theta') + jN\theta' = 0 \tag{6.16}$$

where we let $\theta' = \alpha_x L_1$.

Therefore, the slow mode solution is governed by the equation

$$\tanh\theta' + \tanh T\theta' + N\theta' = 0 \tag{6.17}$$

Using the method discussed before, for hyperbolic tangent function, the solution only occurs if the condition

$$1 + T > -N \tag{6.18}$$

is satisfied.

That is impedance Z must be capacitive with

$$C > \frac{1}{\omega^2 \mu b(L_1 + L_2)} \tag{6.19}$$

The phase constant is given by:

$$\beta = \sqrt{\epsilon_r k_0^2 + {\alpha_x}^2} \tag{6.20}$$

From the analyse above, we know that the fast mode solution only occurs if the condition

$$C < \frac{1}{\omega^2 \mu b(L_1 + L_2)} \tag{6.21}$$

is met (C is the capacitance per unit length). Combining with the expression (6.19), the transition point between slow and fast is

$$f_t = \frac{1}{2\pi\sqrt{\mu C b(L_1 + L_2)}} \tag{6.22}$$

Thus, in the fundamental mode, theoretically, the fast mode propagates below f_t and above frequency f_t, the propagation will be in the slow mode region.

We compare the phase constant dispersion graphs by using theoretical analyses and HFSS. The impedance Z we used is purely capacitive with value of 60pF/m. The dispersion curves and field variations at different frequency points are shown in figure 6.6. The structure with periodic boundary conditions is shown in the figure as well.

In the dispersion figure, the solid lines are the theoretical results, and the dash lines are the HFSS results. A light line is added.

In the fundamental mode of both results, the fast mode propagates below the light line. By checking the fields in figure 6.6, it is clear that the E-field keeps the half mode distribution, which is like the sinusoidal function.

Above the light line, the slow mode propagation occurs, and the electric fields start to concentrate around the slot like the hyperbolic sine function.

We can see that the higher order modes compare very well in both methods. The fundamental mode however does not compare very well. In the theoretical analysis, we consider the component Z in the circuit as a capacitance of 60pF/m. But in HFSS, there are other unavoidable affects to the circuit, such as the capacitance exists in the slot, and the vertical capacitances of the waveguide. These will slightly change the actual capacitance contributed to the waveguide. That is a reason why the curves in this mode have different slopes.

Another reason is that in the simulation environment, the electric field of slow mode does vary along Y direction. In the field distribution, it is clear to see this variation. However, in the theory of TRT, we assume that the E-field has no variation with Y. Even though, both solution curves in the fundamental mode follow the same shape and demonstrate slow mode propagation.

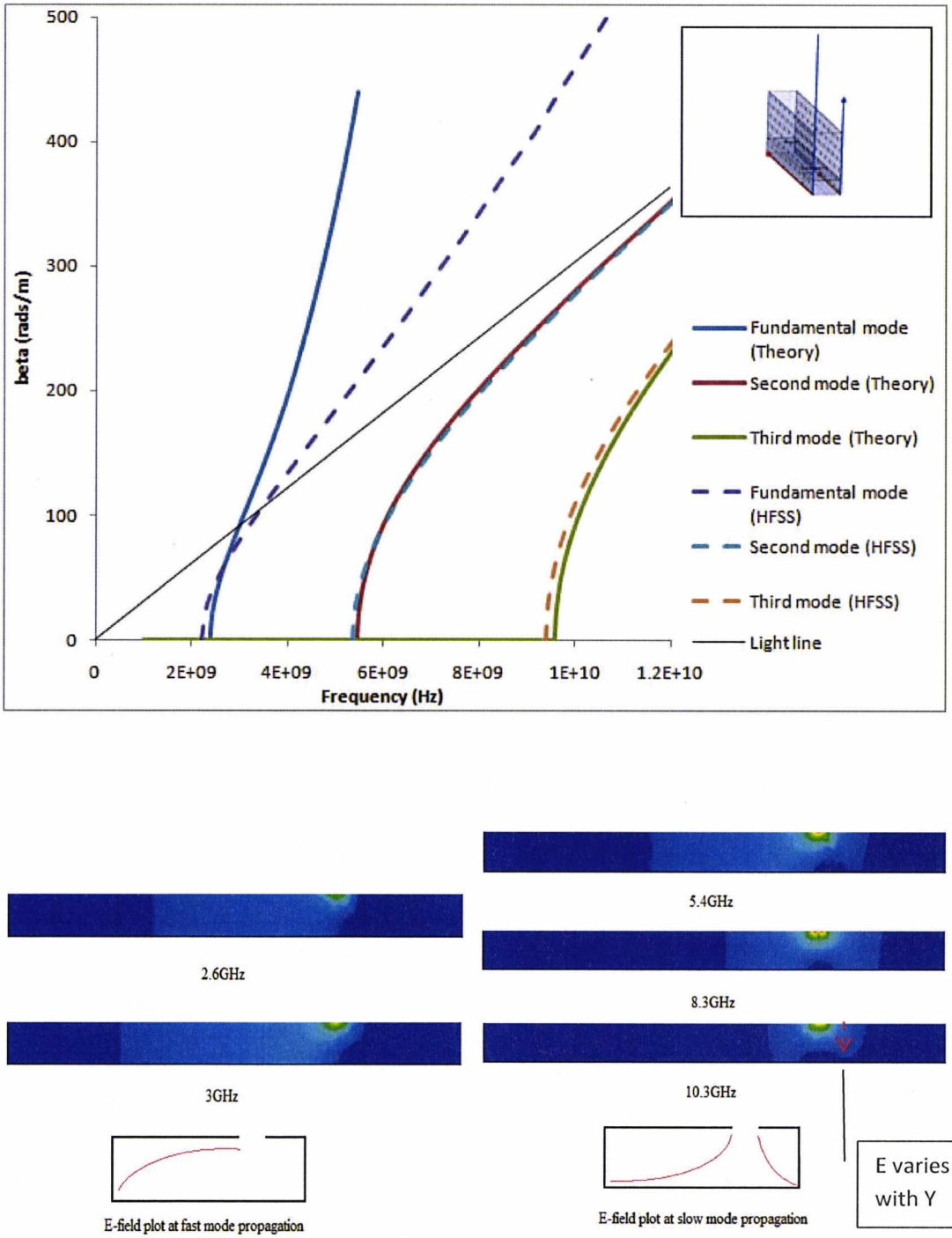

Figure 6.6. The dispersion curves and E-field variations at different frequency points (solid line- theoretical results based on equation (6.15) and (6.20), dash line-HFSS results)

Using the equation (6.22) to calculate the transition point between slow and fast mode is:

$$f_t = \frac{1}{2\pi\sqrt{\mu Cb(L_1 + L_2)}} \approx 3.2GHz \tag{6.23}$$

This approximately matches with the theoretical result. In HFSS result, this point is a bit higher than the calculated.

6.1.3 Losses

The loss is mainly caused by the resistance of component Z in the circuit. Especially in the slow mode propagation, the loss is much higher than that of fast mode. In this section, we introduced the theoretical method to calculate the loss of the circuit.

We let the component Z include the series resistor r and reactance X. Therefore, written as the impedance form, Z is complex.

$$Z = r + jX \tag{6.24}$$

The equation is

$$jZ_0 \tan k_x L_1 = -(Z + jZ_0 \tan k_x L_2) \tag{6.25}$$

with $Z_0 = \frac{b\omega\mu}{k_x}$.

Thus,

$$\frac{1}{k_x}(\tan k_x L_1 + \tan k_x L_2) = -\frac{Z}{jb\omega\mu} \tag{6.26}$$

Let

$$f(k_x) = \frac{1}{k_x}(\tan k_x L_1 + \tan k_x L_2) \quad (6.27) \, . and \; Z' = \frac{Z}{b\omega\mu}, r' = \frac{r}{b\omega\mu}, X' = \frac{X}{b\omega\mu}$$

So

$$f(k_x) = -\frac{Z}{jb\omega\mu} = jZ' = j(r' + jX') \tag{6.28}$$

Because Z is complex, so k_x must also be complex. Then we replace k_x with k_x-$j\alpha_x$. Now,

$$f(k_x - j\alpha_x) = j(r' + jX') = jr' - X' \tag{6.29}$$

If α_x is small, we can use the Taylor series to expand this function as:

$$f(k_x - j\alpha_x) \approx f(k_x) - j\alpha_x f'(k_x) + higher\ order\ terms \tag{6.30}$$

Where $f'(k_x)$ is the derivative of $f(k_x)$.

If we only take the first term as the approximate value of the k_x function, we will get:

$$f(k_x) - j\alpha_x f'(k_x) = jr' - X' \tag{6.31}$$

Hence, equating the real and imaginary parts yields:

$$f(k_x) = -X' \tag{6.32}$$

And

$$\alpha_x = -\frac{r'}{f'(k_x)} \tag{6.33}$$

So

$$f(k_x) = \frac{1}{k_x}(\tan k_x L_1 + \tan k_x L_2) = -X' \tag{6.34}$$

Now,

$$f'(k_x) = -\frac{1}{k_x^2}(\tan k_x L_1 + \tan k_x L_2) + \frac{1}{k_x}(L_1 \sec^2 k_x L_1 + L_2 \sec^2 k_x L_2) \tag{6.35}$$

So if we set

$$X'' = \frac{X'}{L_1}, r'' = \frac{r'}{L_1}, T = \frac{L_2}{L_1}$$

then

$$f'(k_x) = \frac{1}{k_x}(X' + L_1 \sec^2 k_x L_1 + L_2 \sec^2 k_x L_2) \tag{6.36}$$

Substituting with (6.33), we get

$$\alpha_x = -\frac{r' k_x}{(X' + L_1 \sec^2 k_x L_1 + L_2 \sec^2 k_x L_2)} = -\frac{r'' k_x}{(X'' + \sec^2 k_x L_1 + T \sec^2 k_x L_2)} \tag{6.37}$$

Now the phase constant is:

$$\beta(k_x) = \sqrt{\epsilon_r k_0^2 - k_x^2} = \sqrt{\epsilon_r} k_0 \left(1 - \frac{k_x^2}{\epsilon_r k_0^2}\right)^{\frac{1}{2}} \tag{6.38}$$

If we include the loss, then let the phase constant with the loss to be $\beta(k_x - j\alpha_x)$

$$\beta(k_x - j\alpha_x) = \beta(k_x) - j\alpha_x \beta'(k_x) + higher\ order\ terms \tag{6.39}$$

And

$$\beta'(k_x) = \frac{\sqrt{\epsilon_r} k_0}{2}\left(\frac{-2k_x}{\epsilon_r k_0^2}\right)\left(1 - \frac{k_x^2}{\epsilon_r k_0^2}\right)^{-\frac{1}{2}} = -\frac{k_x}{\beta(k_x)} \tag{6.40}$$

So

$$\beta(k_x - j\alpha_x) = \beta(k_x) + j\frac{\alpha_x k_x}{\beta(k_x)} \tag{6.41}$$

And the propagation constant $\gamma = \alpha + j\beta$, then

$$\beta = -j\gamma + j\alpha \tag{6.42}$$

Let the phase constant be $\beta(k_x)$, when the loss is zero, then:

$$\gamma = j\beta(k_x) \tag{6.43}$$

Thus, including the loss, the phase expression will be:

$$\beta(k_x - j\alpha_x) = \beta(k_x) + j\alpha \tag{6.44}$$

So equalling (6.41) and (6.44), the attenuation constant will be:

$$\alpha = \frac{\alpha_x k_x}{\beta(k_x)} \tag{6.45}$$

For the slow mode case, a similar analysis yields:

$$k_x = -\frac{r''\alpha_x}{(X'' + \sec^2 \alpha_x L_1 + T \sec^2 \alpha_x L_2)} \tag{6.46}$$

and the phase constant is

$$\beta = \sqrt{\epsilon_r k_0^2 + \alpha_x^2} \tag{6.47}$$

The attenuation constant of slow mode propagation becomes

$$\alpha = \frac{\alpha_x k_x}{\sqrt{\epsilon_r k_0^2 + \alpha_x^2}} \tag{6.48}$$

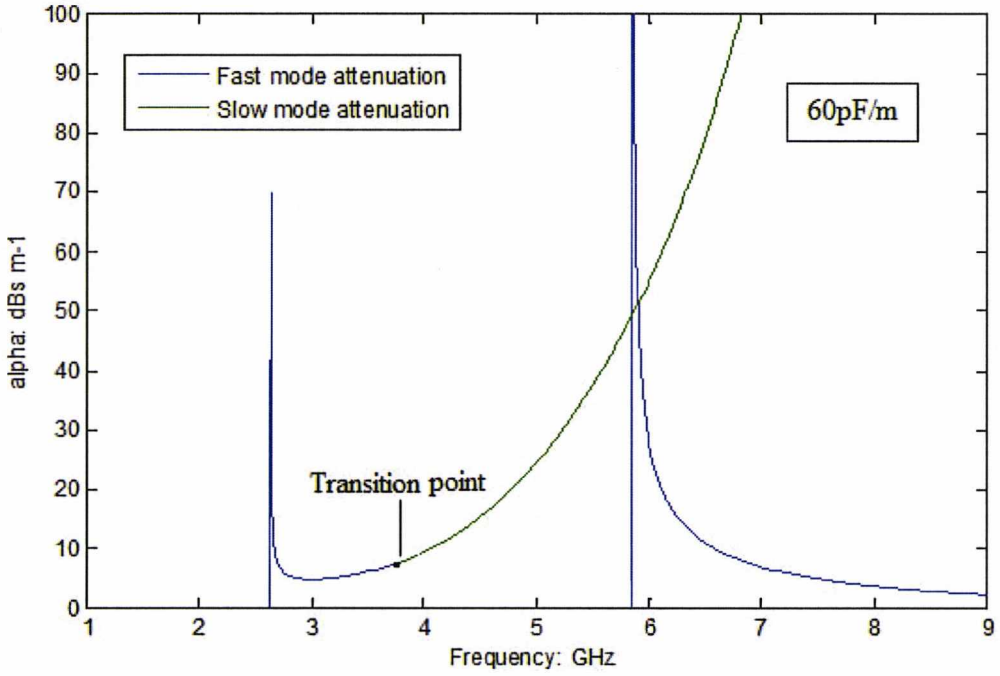

Figure 6.7. The theoretical attenuation constants (dB/m) including fast and slow modes (series resistance r=0.01125Ω•m)

Here is the theoretical attenuation plot in figure 6.7. The series resistance is 0.01125Ω•m.The unit of the Y axis is dBs/m. The loss in the fundamental mode is slightly larger than the second one's. The blue lines are the fast modes, and the green line is the slow mode. It is clear that the attenuation constant increased rapidly in the slow mode range above the transition frequency point. It will cause a dip between the first and second mode. At 3GHz, the fundamental mode has about 5dB/m loss; the second mode has about 3dB/m loss at 8GHz. Those results relate to the perfect condition, which has no dielectric loss or conductive loss.

In HFSS, we use the periodic boundary condition to simulate the waveguide contributed by 60pF/m capacitance. The quality factor Q is related to the attenuation constant [18].

$$\alpha = \frac{V_p}{V_g} \times \frac{\beta}{2Q} \tag{6.49}$$

Where the phase velocity is $V_p=\omega/\beta$ and the group velocity is $V_g=\Delta\omega/\Delta\beta$.

The unit of attenuation constant from HFSS is Nepers (Np) per meter. Transformed from dB/m to Np/m is

$$Np/m = dB/m \div 8.686 \tag{6.50}$$

Therefore, the attenuation constant comparison between theoretical and HFSS results is plotted in figure 6.8.

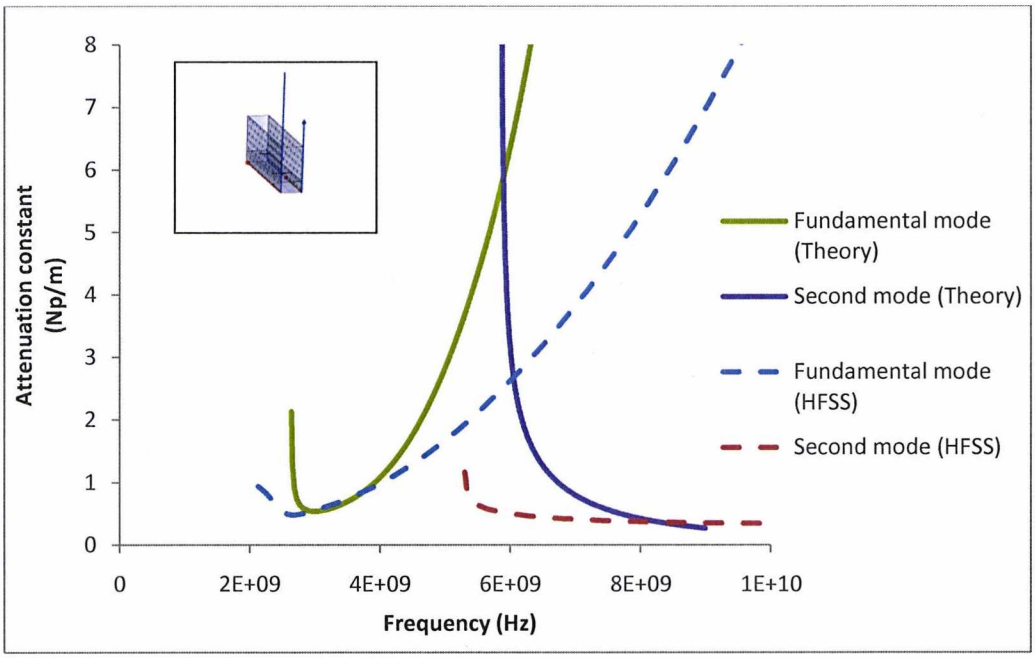

Figure 6.8. Comparison of attenuation constants (Np/m) between theoretical and simulated results

Compared with the theoretical result, the simulated slope of the attenuation constant curve is smaller in slow mode range. Referred to section 6.1.2, that is the same reason as in the phase dispersion figure (figure 6.6). However, the attenuation constants of both results at the fast mode compare reasonably well.

At the second order mode, the simulated result has much less attenuation at the cut-off frequency. The theoretical attenuation dropped very quickly and converged with simulated curve at 8GHz.

6.2 Distributed capacitance and periodically loaded components to planar half-mode SIW

6.2.1 Distributed capacitance

In this design, the purely capacitance C is added to the planar half-mode substrate integrated waveguide (the waveguide is referred to chapter 4). At cut off frequency ω_c, the expression on the resonant point needs to be satisfied as:

$$Z_0 \tan k_x L_1 + Z_0 \tan k_x L_2 = \frac{1}{\omega_c C} \tag{6.51}$$

Here C is the capacitance per unit length.

As the value C increases, the cut off frequency ω_c needs to be decreased. Therefore, this can be used to decrease the cut off frequency of the SIW.

We use the planar half-mode substrate integrated waveguide as the foundation. The purpose of our first design is to increase the capacitance of the slot. In order to avoid the effect of periodic structures, we put a continuous PTFE material along the slot on the top. Then, a piece of copper tape with the same length fully covers the slot above the PTFE. This design acts like a capacitor. The model of the structure is shown in figure 6.9.

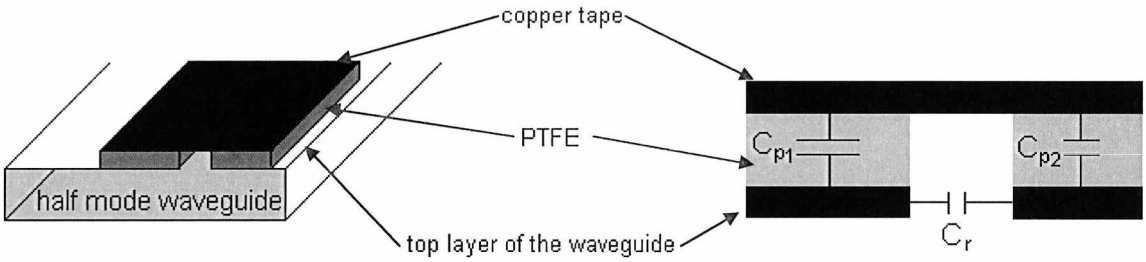

Figure 6.9. Geometry of the structure with non-periodic capacitance

The parallel capacitors C_{p1}, C_{p2} are created inside the PTFE material, and they are series connected by the copper tape. C_r is the capacitance inside the slot of the top layer, and its value is very small. Therefore the total capacitance of this circuit C is:

$$C = C_r + (\frac{1}{C_{p1}} + \frac{1}{C_{p2}})^{-1} = C_r + \frac{C_{p1}}{2} \quad if\ C_{p1} = C_{p2} \tag{6.52}$$

The widths of the PTFE material on each side are the same, so the C_{p1} is almost equal to C_{p2}. For a parallel capacitor, its capacitance is determined by:

$$C_p = \frac{\varepsilon_r \varepsilon_0 A}{D} \tag{6.53}$$

Where ε_r is the relative permittivity of the material, A is the overlapping surface area of the plates and D is the distance between the plates. For the PTFE material, its thickness is about 0.6mm, and the dielectric constant is approximately 2.07.

We select the width of the PTFE material on each side as 2mm. the total length of the half-mode SIW is 120mm. So the area on each side is then 2mm×120mm=240mm^2. Thus, the capacitance on each side is:

$$C_{p1} = C_{p2} = 7.08pF \tag{6.54}$$

The added value of the capacitance will be half, which is 3.54pF. Converting to the same unit of equation (6.51), it is 29.5pF/m.

Figure 6.10 is the simulated results in HFSS. The cut off frequency of the fundamental mode now is about 2.6GHz. There is a significant dip in S_{21} approximately from 5.5GHz to 7GHz caused by the higher order mode. We suspect that the transition can couple for both modes. In the fundamental mode, most of the S_{11} are just below -10dB; the S_{21} has small insertion loss because the PTFE material has very low loss. In our particular case, the PTFE excited the microstrip mode during the transmission, and it may reduce the bandwidth of the waveguide.

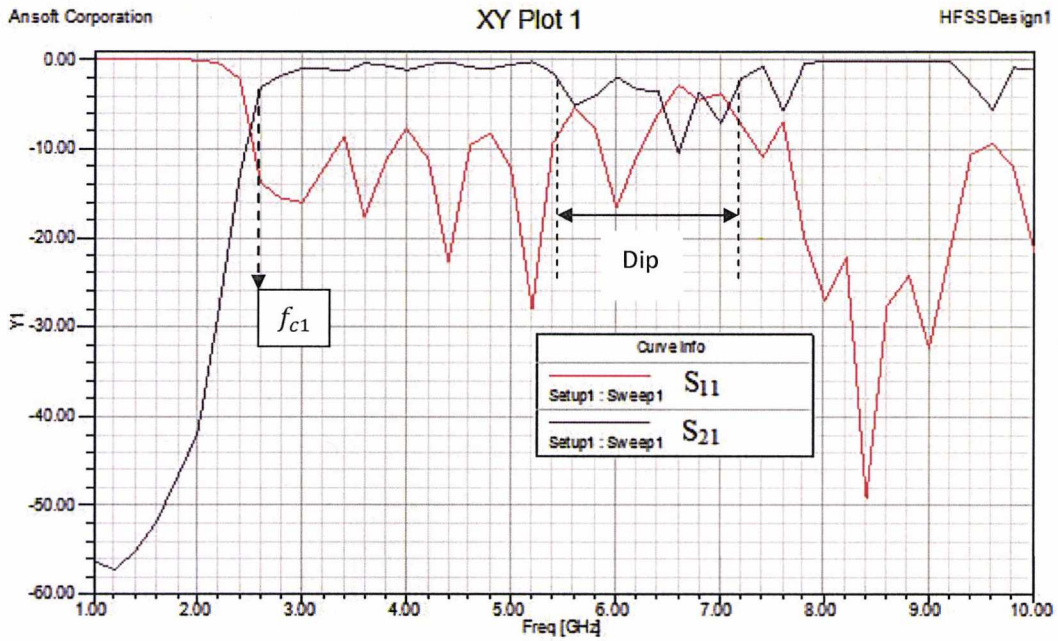

Figure 6.10. Simulated S parameters (dB) with non-periodic capacitance

The fabricated structure is shown in figure 6.11. The size of the PTFE material is a bit larger in the practical work. However, the coverage area of the copper tape which consists of the added capacitance remains the same as the simulation.

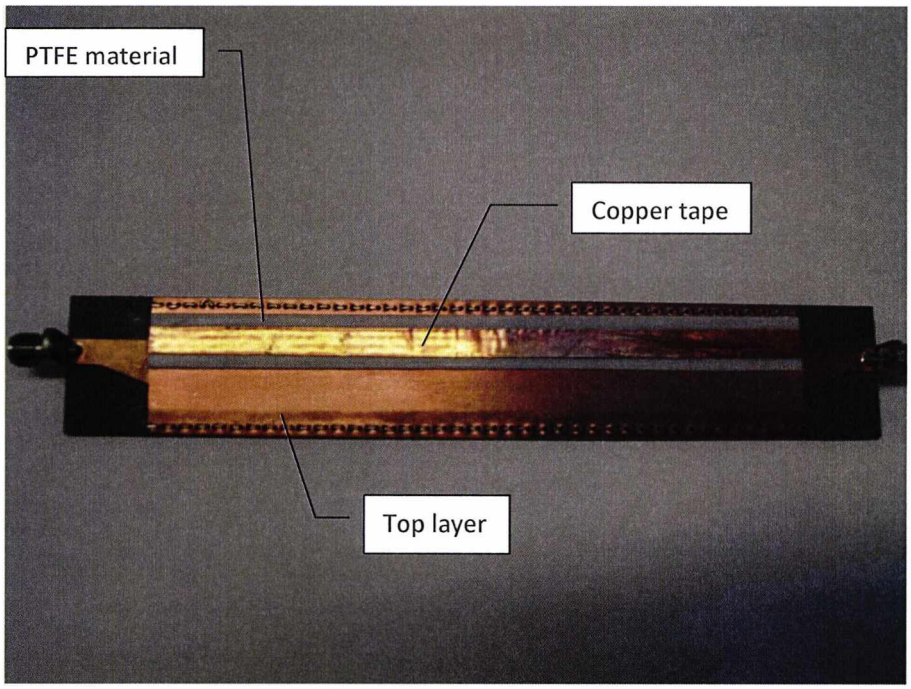

Figure 6.11. The picture of fabricated structure

The measurement is performed using an Anritsu 37397C vector network analyzer. The result is shown in figure 6.12.

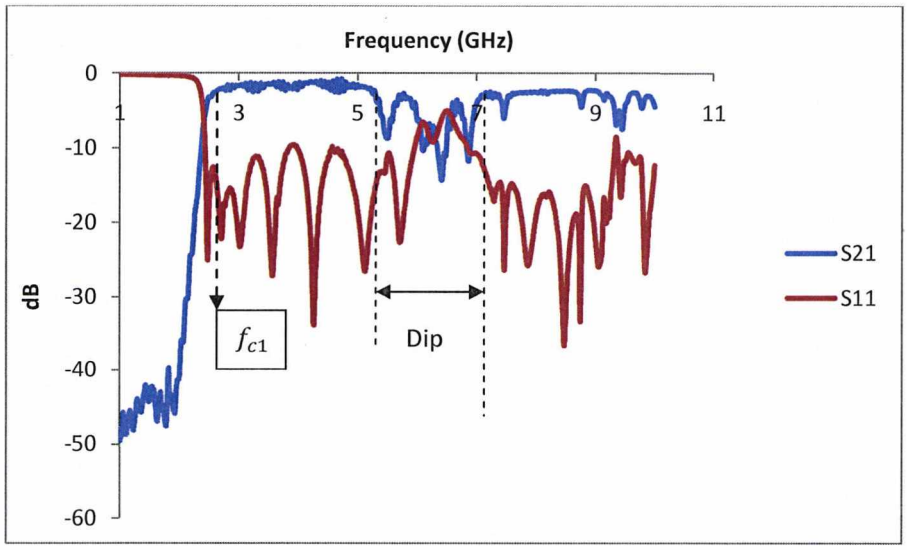

Figure 6.12. Measured S parameters with non-periodic capacitance

It is clear to see that the cut off frequency of the fundamental mode matches with the simulated result of 2.6GHz. The return loss of S_{21} is quite small from 2.6GHz to 5GHz, less than 3dB. There is a dip from 5GHz to 7GHz because of the higher order mode interruption. The second order mode has the normal propagation around 7GHz. The S_{11} is below -10dB, except the region between 6 to 7GHz. Compared with the simulated result, every frequency point and the shapes of the S parameters are compared well.

Figure 6.13 shows the plot of the two S_{21}. One is from the structure with the added capacitance and the other one is from the original planar half-mode waveguide.

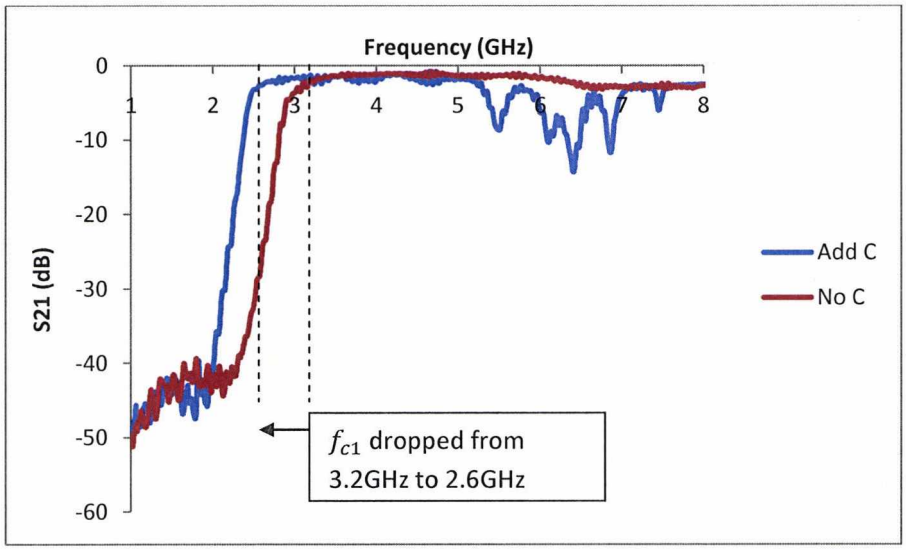

Figure 6.13. Measured S_{21} comparison between original and loaded capacitance waveguides

The original half-mode waveguide starts to propagate at 3.2GHz. The cut off frequency is significantly dropped from approximately 3.2GHz till 2.6GHz by adding additional capacitance. When we add about 29.5pF/m capacitance on the slot, the cut off frequency reduces to 2.6GHz.

As we introduced in chapter 4, the cut off frequency of each mode can be solved in this equation below:

$$tan\, k_x L_1 + tan\, k_x L_2 = \frac{\epsilon}{k_x C' b} \tag{6.55}$$

where $k_x = \omega\sqrt{\mu\epsilon}$.

Now in this design, C' consists of the slot capacitance paralleled with the PTFE capacitances. The plot for the cut off frequency is shown in figure 6.14. The red line is the left part of the equation (6.55), the blue line is the right part, and the slope of the blue line (right part of the equation) is very sensitive to the input capacitance.

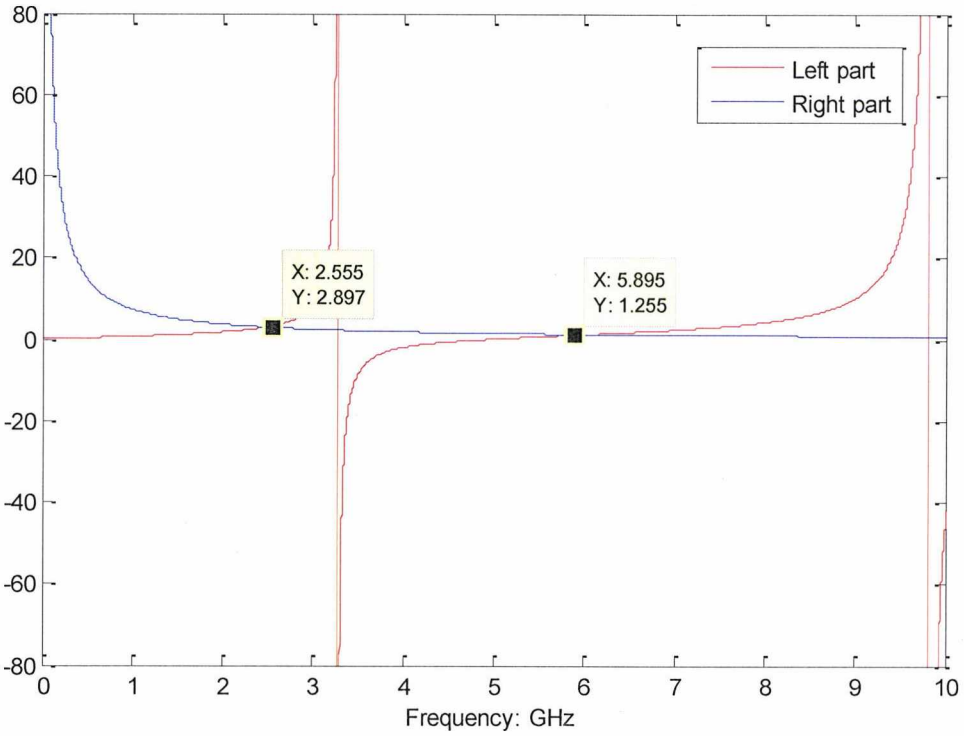

Figure 6.14. Cut-off frequency plot of theoretical equation

According to the plot, the cut off frequency is approximately at 2.5GHz. Around 5.89GHz, the second order mode starts to propagate. However, the cut off frequency of the second order mode is difficult to tell from the measured result. Now we plot the phase dispersion figure in HFSS to compare the theoretical result.

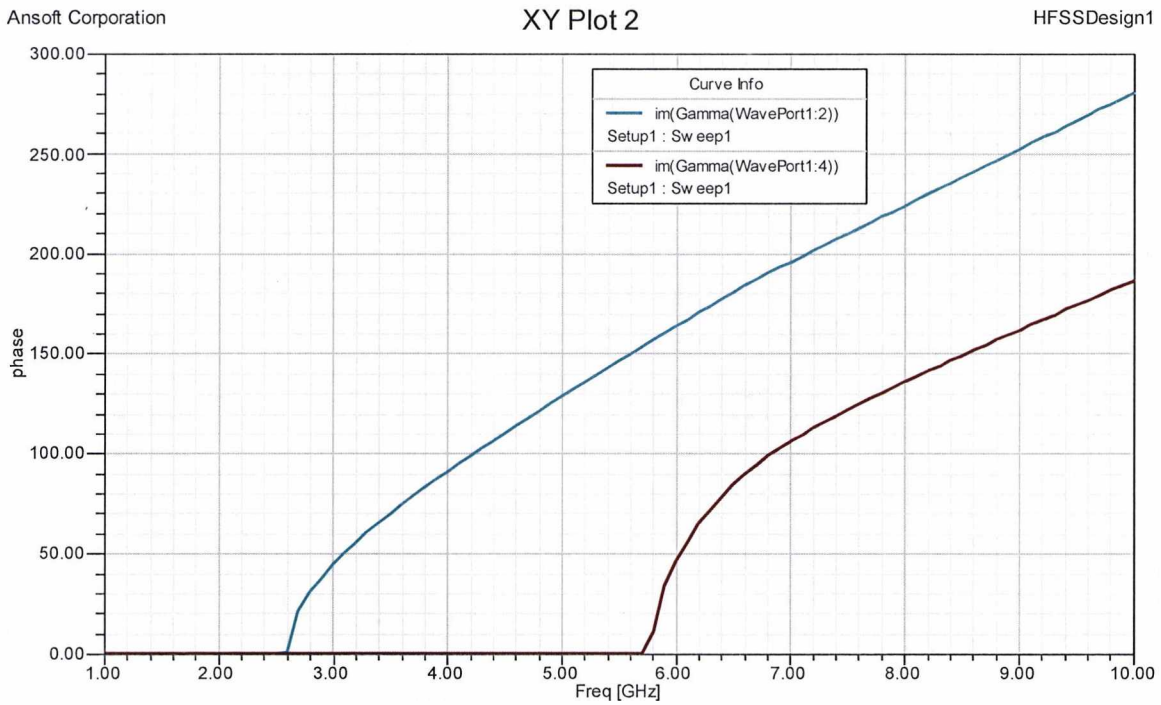

Figure 6.15. Simulated phase constant dispersion figure

Figure 6.15 is the phase constant dispersion figure in HFSS. In the simulation, there are some spurious modes, such as the microstrip mode caused by the added copper foil and the box mode. These modes were shown but not be considered, and have been removed from the dispersion figure. Comparing the simulated result with the theory, the fundamental mode and the higher order mode are well matched. In both results, at 5.8GHz, the higher order mode starts to affect the propagation, and that is how the dip occurs in the S parameter figure.

We can not see any slow mode propagation in the non-periodic structure. That is because the TRT only can analyse the current vector on the surface, which is the x direction in

figure 6.16. For the periodic structure, each unit is very narrow and has very little current flow in z direction, thus there is only x directed current. In our present design, the continuous copper foil allows current to flow in the z direction, and the transverse resonance rules break down.

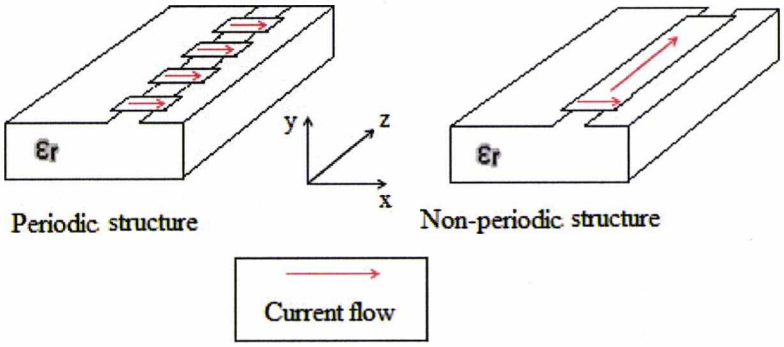

Figure 6.16. Current flow in periodic and non-periodic structures

6.2.2 Periodically added varactor diodes

The next research based on the half-mode waveguide is to apply the varactor diodes over the slot periodically. The structure model is quite similar to the pin diode which has been introduced in the chapter 4. The varactor diode can provide different capacitances under the working voltage. These different capacitances can greatly affect the performance of the half-mode waveguide. Figure 6.17 shows the cross sectional geometry of the structure.

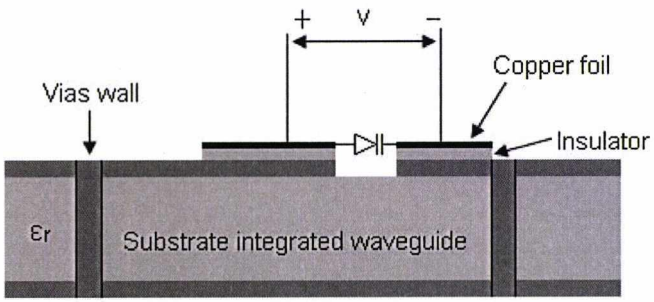

Figure 6.17. Geometry of the SIW added varactor diodes

The equivalent circuit of varactor diode is a bit more complex. Figure 6.18 (a) shows a simple model of a package 2-feet varactor diode. The components in the circuit basically include a junction capacitor C_T, a series inductor L_S and a series variable resistor R_S. BB857 SAT-TV varicap diode is used in this design. On average, the BB857 SAT-TV varicap diode has the junction capacitor C_T with the value of 6.6pF at 1V, and reduced to 0.52pF at 28V (figure 6.18 (b)) [19]. The series inductance is 0.6nH, and the series resistor is about 1.5Ω at 5V.

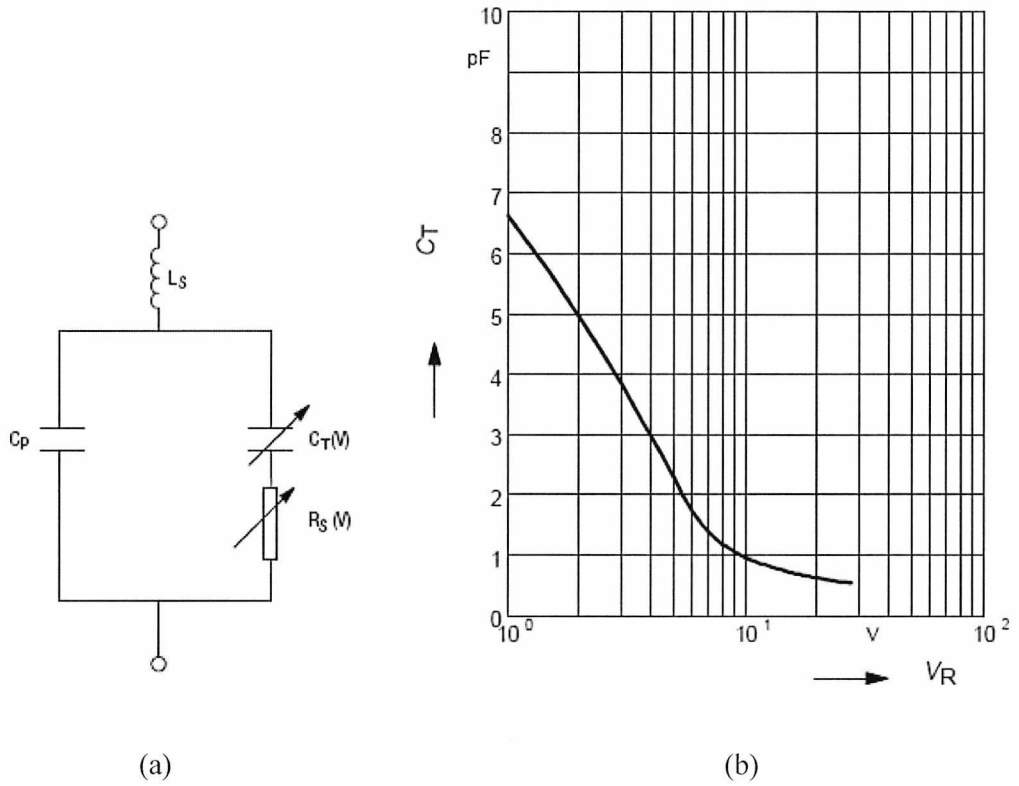

(a) (b)

Figure 6.18. BB857 SAT-TV varicap diode datasheet [19]: (a) Equivalent circuit of the varactor diode, (b) capacitance versus voltage figure

We add six varactor diodes on the slot; each one has been soldered on a single copper tape. They are parallel connected to the power supply and integrated to the half-mode waveguide. The space between each diode is 7.5mm. Figure 6.19 shows the picture of the fabrication.

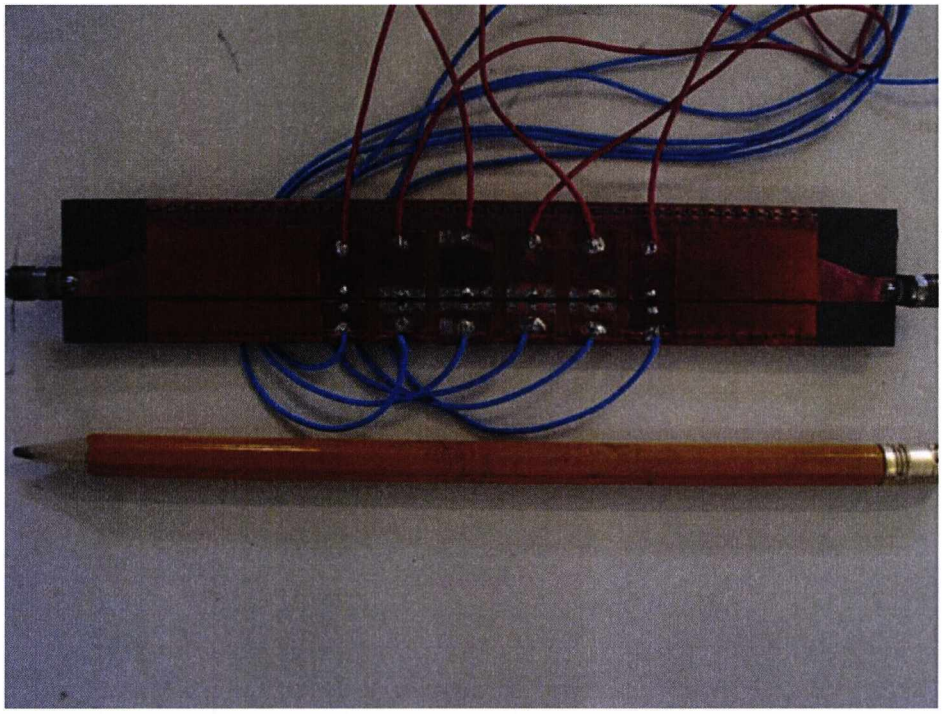

Figure 6.19. The picture of structure with six varactor diodes

During the measurement, we test the structure under four voltages – 1V, 10V, 20V and 30V, which correspond to the capacitances of 960pF/m, 133.3pF/m, 93.3pF/m and 60pF/m. The capacitance values are from the datasheet of the diode and the unit length is based on the dimensions of the design. Figure 6.20 – 6.23 shows S parameters of measured results, phase dispersion curves of simulated results.

There are kinds of lines in the simulated dispersion plot. The first one is the light line, the second kind is the phase constant lines in different modes and the third one is the special line which shows the slow mode above the light line. Corresponding to the transition point, a dip occurs in the slow mode in measured S parameters. Thus we could not see the slow mode transmission; however, it keeps propagating till a certain frequency according to the dispersion curves. This is because the transition of the waveguide may not be excited in the slow mode, and the energy concentrates mostly on the slot. Therefore, there is very little energy flow in the slow mode and hard to analyse in the S parameter plots.

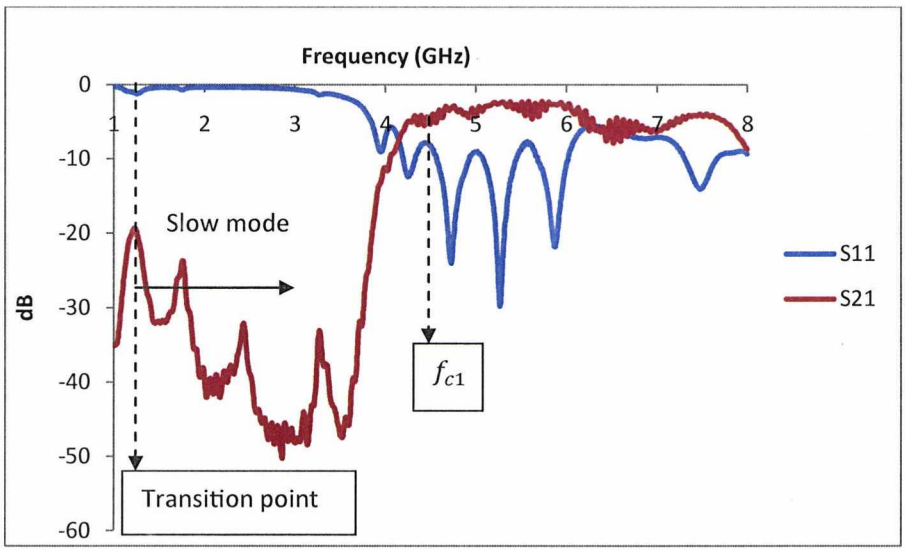

(a)

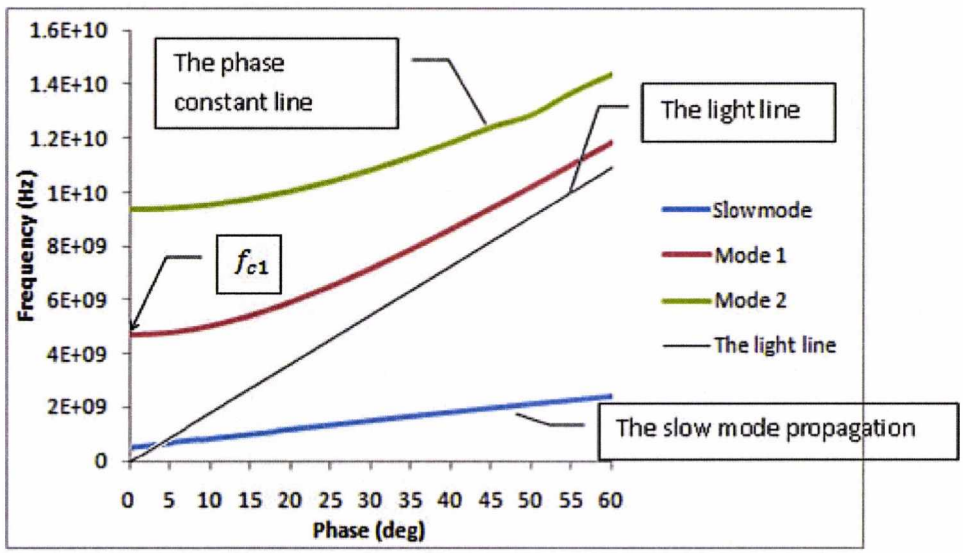

(b)

Figure 6.20. The structure by applying 1v voltage (input capacitance: 960pF/m).
(a) measured S parameters, (b) simulated dispersion curves.

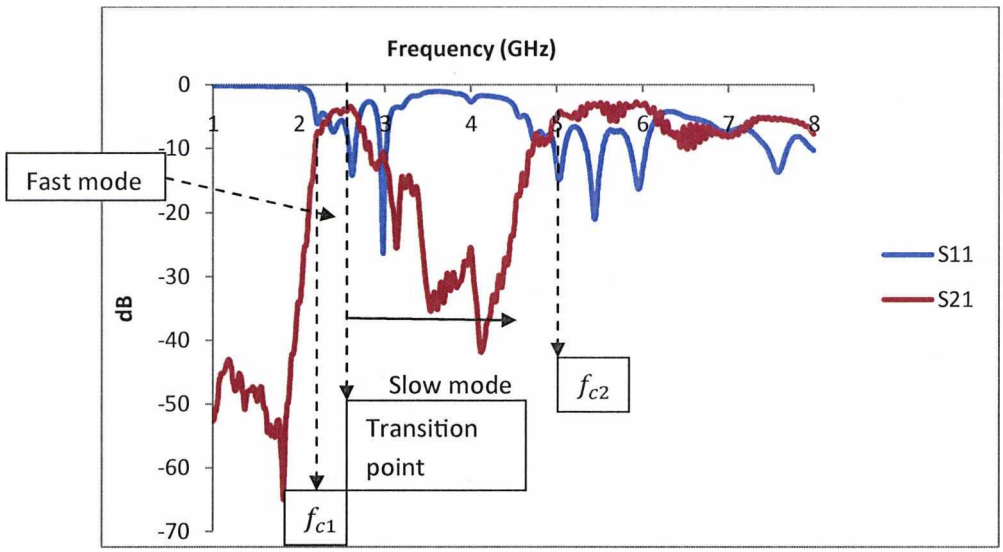

(a)

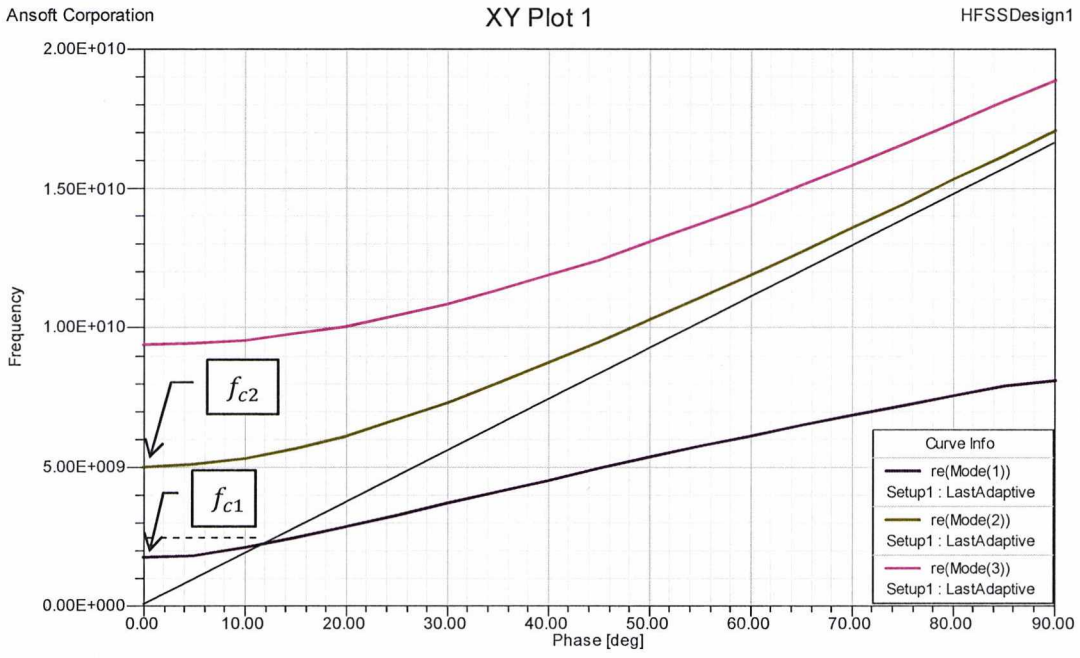

(b)

Figure 6.21. The structure by applying 10v voltage (input capacitance: 133.3pF/m). (a) measured S parameters, (b) simulated dispersion curves.

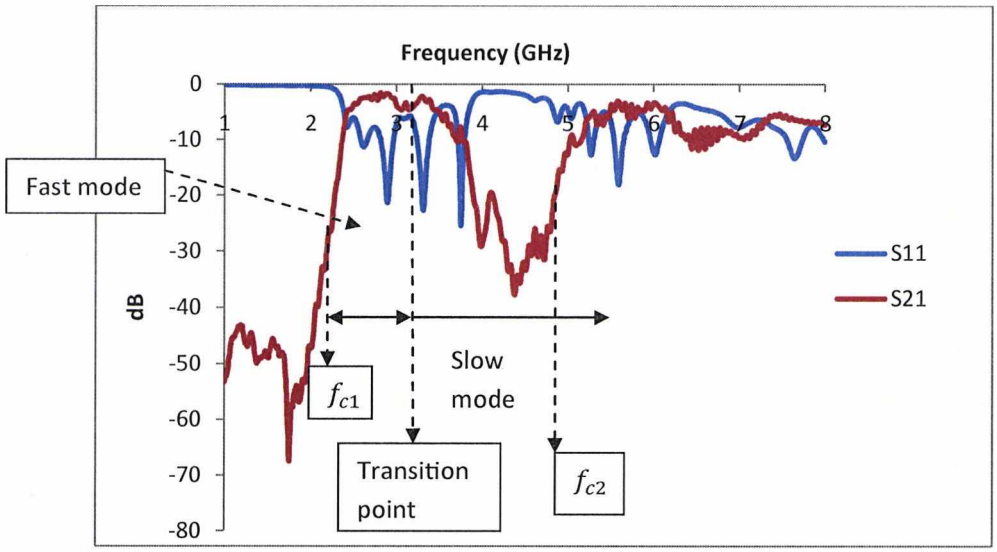

(a)

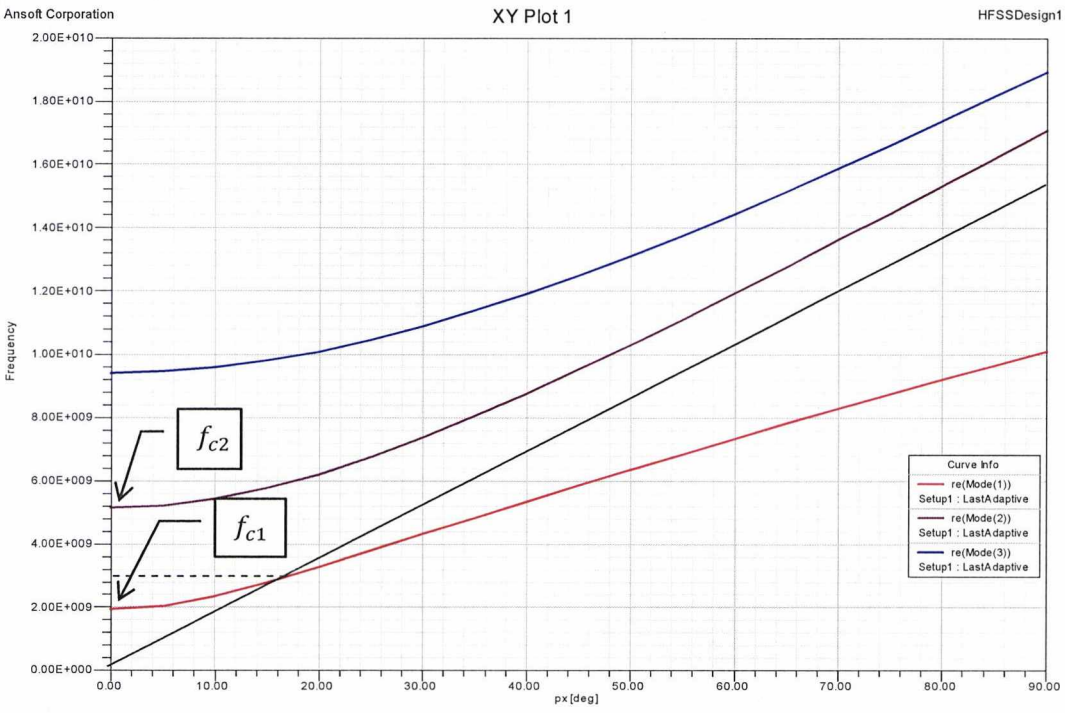

(b)

Figure 6.22. The structure by applying 20v voltage (input capacitance: 93.3pF/m).
(a) measured S parameters, (b) simulated dispersion curves.

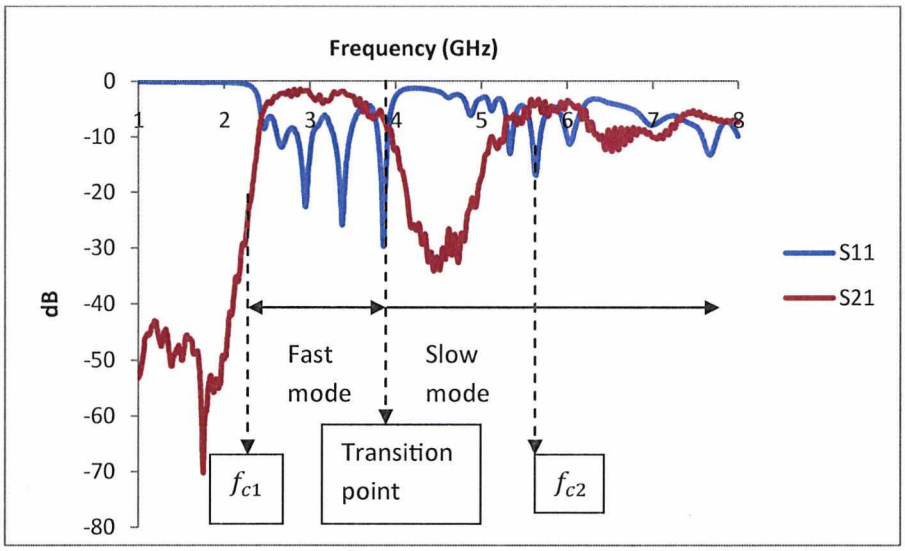

(a)

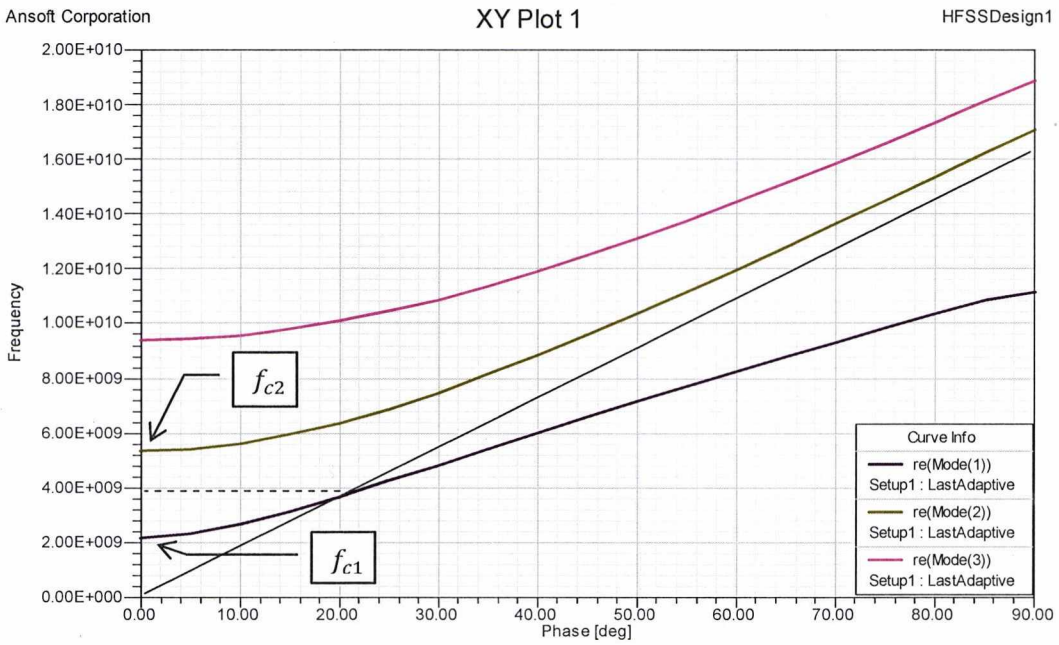

(b)

Figure 6.23. The structure by applying 30v voltage (input capacitance: 60pF/m). (a) measured S parameters, (b) simulated dispersion curves.

The balanced equation at each cut off point is:

$$\tan\theta + \tan T\theta = -N\theta \tag{6.56}$$

where $\theta = k_x L_1, N = -\frac{1}{\omega^2 \mu b L_1 C}$.

The fundamental mode has solution in the range $0<\theta<\pi/2$ for certain value of N. According to the analysis of section 6.1.1, if the slope of $-N$ is very small (means C is very large), the line will not cross the tan function and there will be no solution apart from the trivial solution $\theta=0$.

In figure 6.20, the varactor diodes provide capacitance of 960pF/m to the waveguide. In this case, the element $-N$ in the right part of the equation (6.56) becomes quite small. Thus, because of the small slope of $-N\theta$ line, there is no fast mode solution at the fundamental mode except the slow mode above the light line. The second mode starts at about 4.6GHz.

In figure 6.21, the varactor diodes provide capacitance of 133.3pF/m to the waveguide. As the capacitance decreases, the slope of $-N\theta$ line increases. The fundamental mode of waveguide starts to have the fast mode solution. However, the fast mode range is quite narrow that only last 0.3GHz and then the slow mode start to propagate at 2.2GHz.

In figure 6.22, the varactor diodes provide capacitance of 93.3pF/m to the waveguide. The fundamental mode propagation becomes much better than that of 133.3pF/m. The insertion loss reduced and the operating range increases.

In figure 6.23, the varactor diodes provide capacitance of 60pF/m to the waveguide, which is the lowest capacitance. There is a significant fast mode propagation which has almost 1GHz operating frequency range.

Through the comparisons, the results compare well. The transition frequency points in simulated phase dispersion curves correspond to the dips in the measured S parameter results.

6.2.3 Periodically added high value varactor diodes

There is another type of varactor diode we try to measure. It is the high value varactor diode - BB149A UHF Varicap diode, which has the maximum capacitance 21.26pF at 1V and the minimum capacitance 2pF at 28V.

Without changing other components but only replacing the varactor diodes, we did the measurement and programme again. The capacitances we choose are 2834.7pF/m (V_R=1V), 666.7pF/m (V_R=10V) and 266.7pF/m (V_R=28V). One condition is that the actual capacitance may be reduced by applying high frequency on the varicap diode. Figure 6.24 - 6.26 shows the measured S parameter graphs with the theoretical phase constant dispersion plots.

The high value varactor diodes almost stop the fast mode propagation of the fundamental mode, because of the high element C that makes the slope of $-N$ too small. As the frequency increases, from the theoretical plots, we can see that the slow mode starts to have very short propagation range. However, due to the high loss distributed by the fast mode, we could not see the slow mode propagation in the measured results.

The second mode propagates very well at frequency range 4.5GHz – 7GHz with respect to different loaded capacitances. The variable capacitances only affect the starting frequency point of the higher order mode. As the capacitance reduced, the cut off frequency of the higher order mode increased.

Compared with the structure embedded with low value varactor diodes, this design has better second order mode propagations.

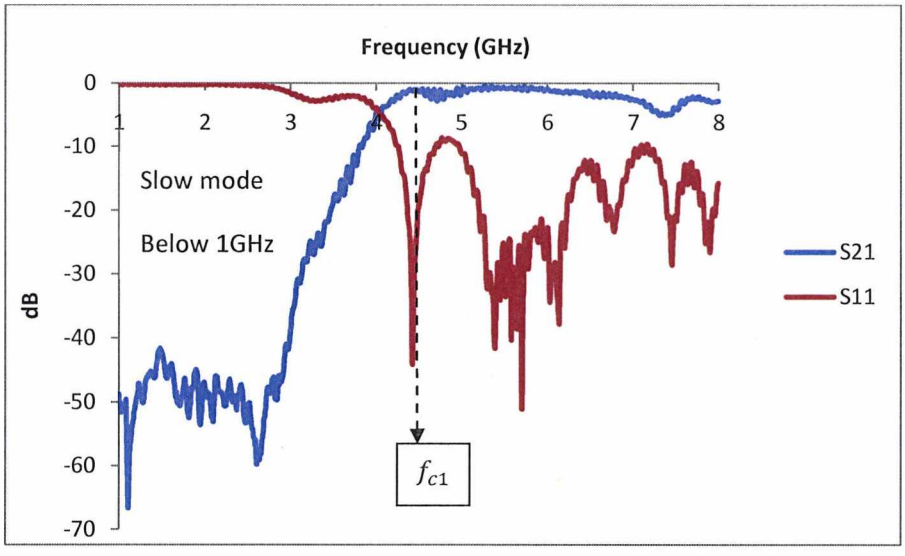

(a)

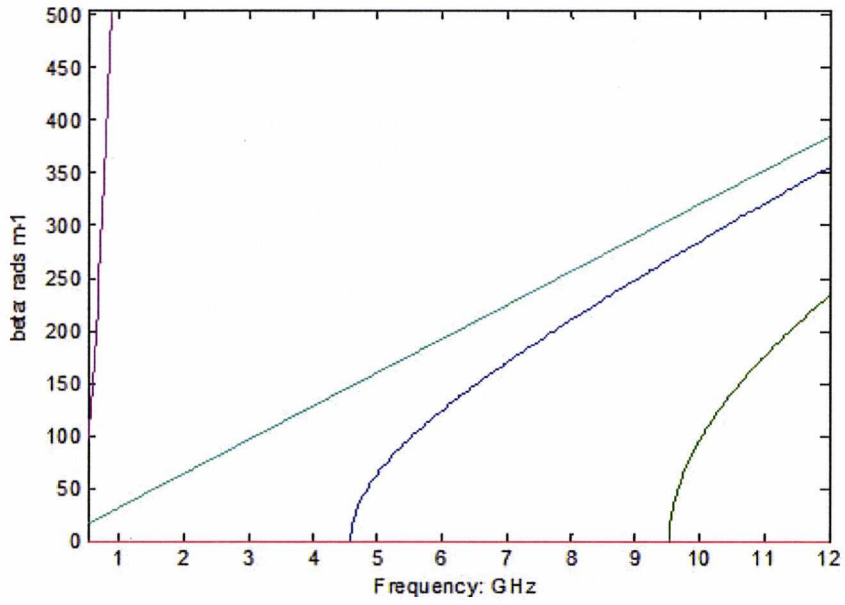

(b)

Figure 6.24. The structure by applying 1v voltage (input capacitance: 2834.7pF/m). (a) measured S parameters, (b) theoretical dispersion curves.

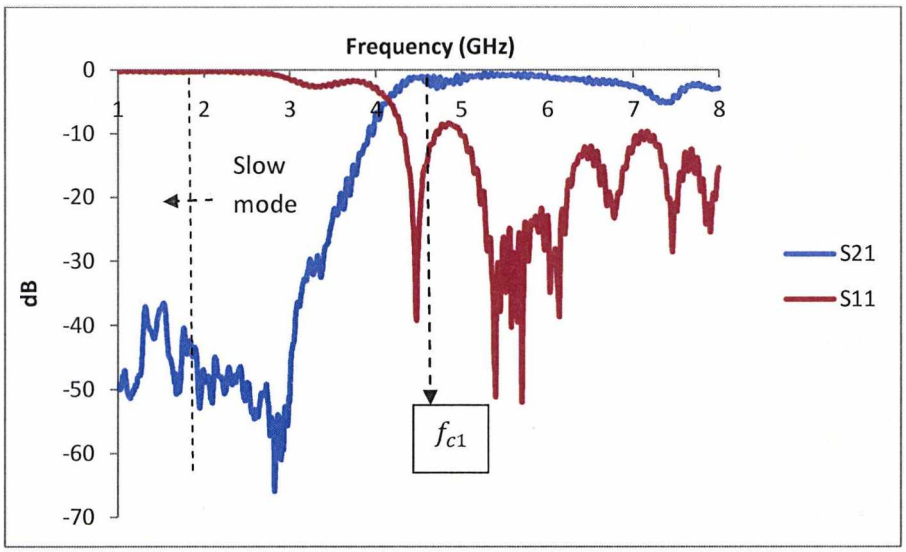

(a)

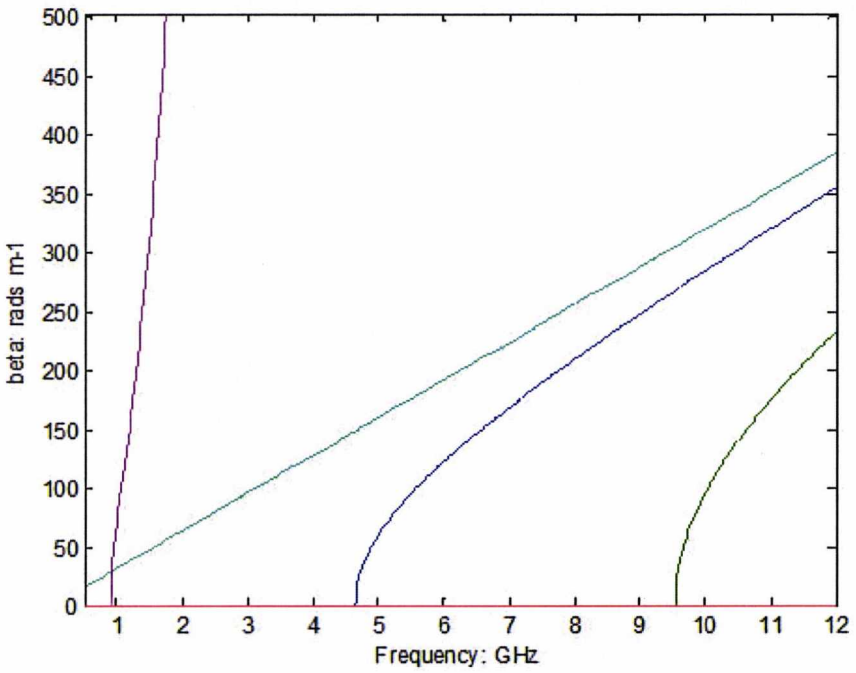

(b)

Figure 6.25. The structure by applying 10v voltage (input capacitance: 666.7pF/m). (a) measured S parameters, (b) theoretical dispersion curves.

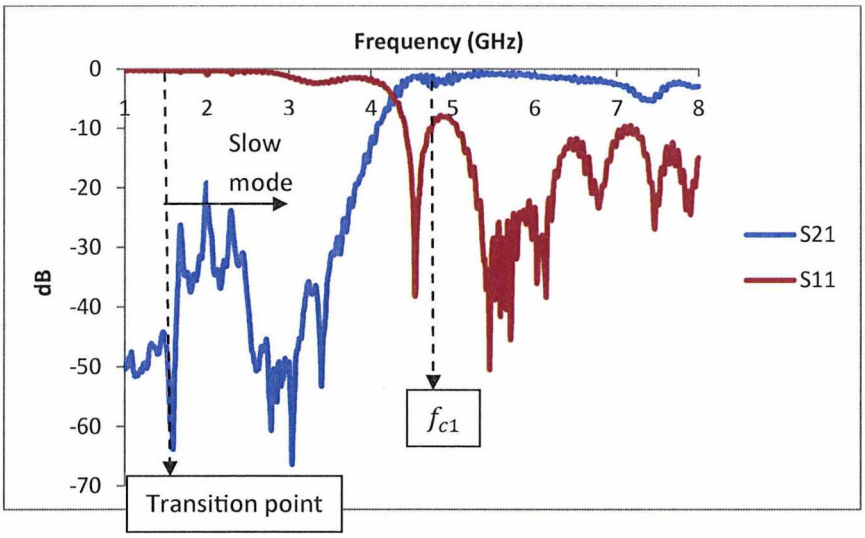

(a)

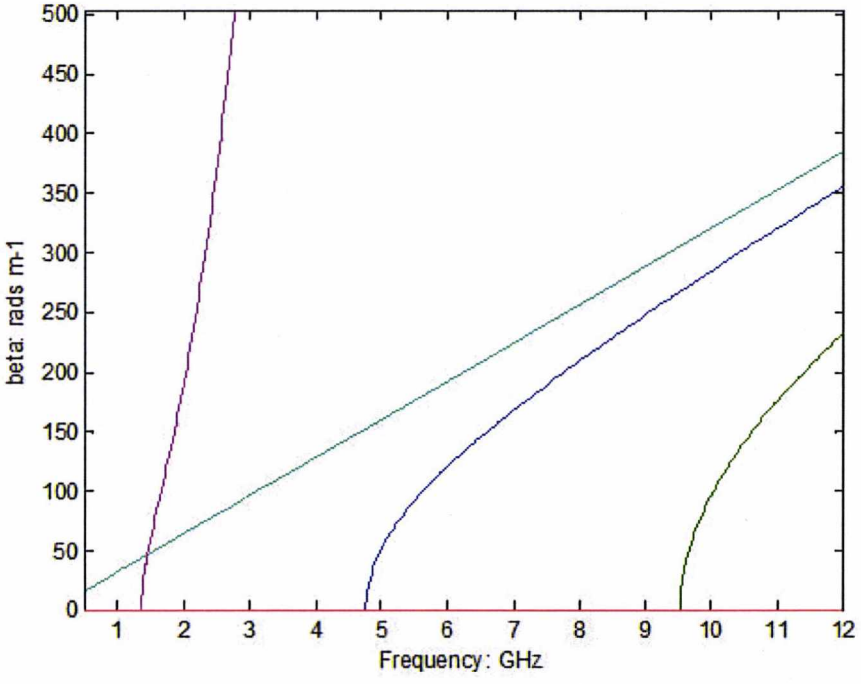

(b)

Figure 6.26. The structure by applying 28v voltage (input capacitance: 266.7pF/m). (a) measured S parameters, (b) theoretical dispersion curves.

6.3 Phase shifter design

The phase shifter is one of the most important devices in the signal transmission system [20]-[22]. In many years' research, it has been widely used in the communication system, measurement and instrumentation system, industrial system, etc, especially in the radar system [23]. As the phase changes of the signal, they provide the means for beam steering in antenna arrays [24].

There are two types of standard phase shifters – digital (binary) and analogue (continuously varied). The switched-type digital phase shifters have been well developed in the microwave systems [25] [26]. The switching devices such as pin diodes or transistors are applied. However, the insertion loss relates to the number of switches, in which case, the wider phase shift range means the more loss. Thus, the analogue type phase shifter has the applications by embedding the devices such as varactor diodes or ferrites [27]. The tunable phase shifter with ultra wideband performance by using microstrip-slot technique has been demonstrated [28]. Embedding with the SIW, novel phase shifters with the tuning or self-compensating abilities have been developed [16] [29]. By changing the loaded capacitance contributed to the waveguide, the cut off frequency and the phase constant can be easily controlled. In this section, this new technique and a tunable phase shifter have been demonstrated. Compared with other phase shifters, our novel phase shifter has the advantage of simple structure, easy fabrication processing, low cost and small size.

6.3.1 Structure

The biasing technique of loading the varactor diodes to the waveguide is similar to the previous design [30]. The varicator diodes are the BB857 SAT-TV varicap diode which has a range of capacitance from 0.45 pF to 7.2 pF. However, the new structure only has two varactor diodes on the top, and the size of the copper tape has been reduced. A dual 35V power supply provides the tunable voltage to the plates. The width of each copper tape is 2.5mm, and the distance between them is 2.5mm as well. The total length of the phase

shifter is therefore 7.5 mm. RF chokes are used to avoid coupling to the bias wires. Figure 6.27 shows the fabrication.

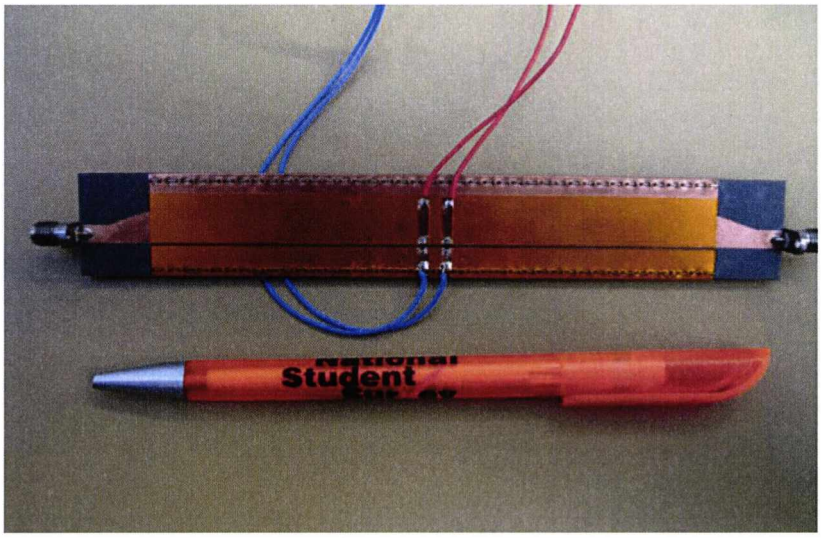

Figure 6.27. The picture of fabricated phase shifter

6.3.2 Measurements

We use the Anritsu 37397C vector network analyzer to measure the structure. The tunable voltage is provided by a dual 35V power supply. The test voltages we use are from 0 to 30v with 5 volts step.

Figure 6.28 shows the magnitude S_{21} in the higher order mode. Because the fundamental mode only appears when the diodes we have at the very low capacitance condition, so we choose the second order mode for our test. As the voltage increases, the capacitance provided by the varactor diodes decreases. Therefore, the cut off frequency of this mode increases.

Figure 6.29 shows the measured phase change (difference in phase shift between zero and biased condition) for various bias voltages. As we can see a phase shift of greater than 150 degrees can be achieved at 5 GHz for high bias values. However, we find that at this point the insertion and return loss are poor because the waveguide approaches cut-off at this

frequency and therefore the operation of the phase shifter should be limited to above 5.3 GHz.

Figure 6.30 shows the change of phase as a function of applied bias for the four frequency points 5.3, 5.5, 5.7 and 6 GHz. The phase shift is reasonably linear with applied bias for voltages less than 20 V.

Figure 6.31 shows the measured insertion loss of the structure at 5.3, 5.5, 5.7 and 6 GHz as a function of bias. As can be seen the insertion loss is increased at low frequencies where the waveguide approaches cut-off. This is particularly so for large bias voltages. However, if we limit the bias to 20 or 25 V then the insertion loss is generally lower than 3 dB over the 5.3 - 6 GHz range. With reference to figure 6.29 this implies that a maximum phase shift of 50 degrees is obtainable at 5.3 GHz with 20 V bias and 4dB insertion loss. The return loss is below 10 dB over the entire range and generally below 20 dB.

However, this phase shifter design is not very successful, due to the large change in amplitude, non-linear phase response, limited working frequency etc. By increasing the number of loading diodes, the performance can be improved.

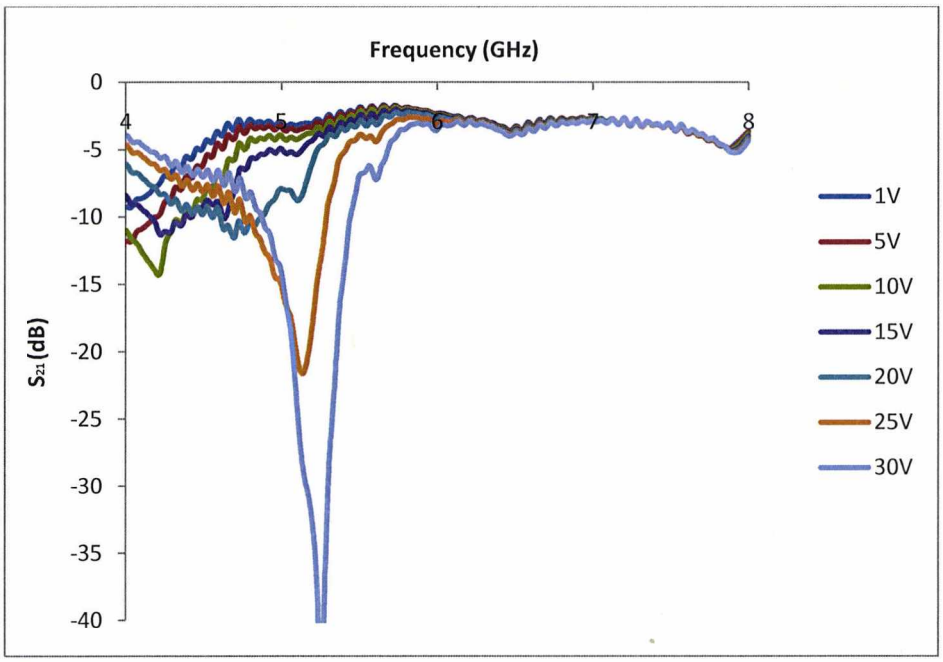

Figure 6.28. Magnitude S_{21} in the higher order mode for various bias voltages

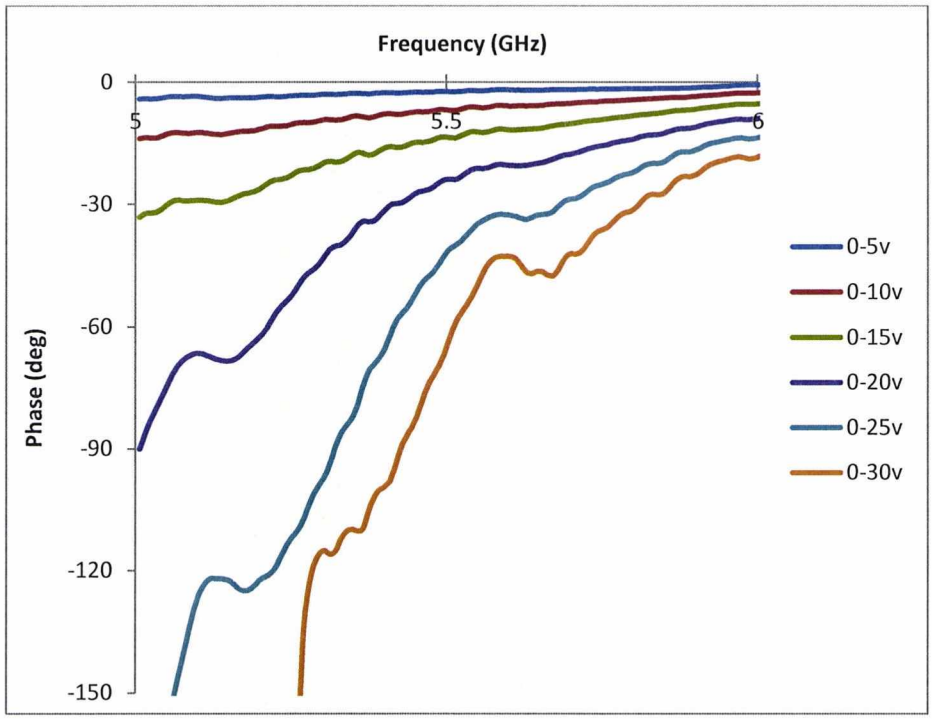

Figure 6.29. Measured phase shift versus frequency (GHz) for various bias voltages

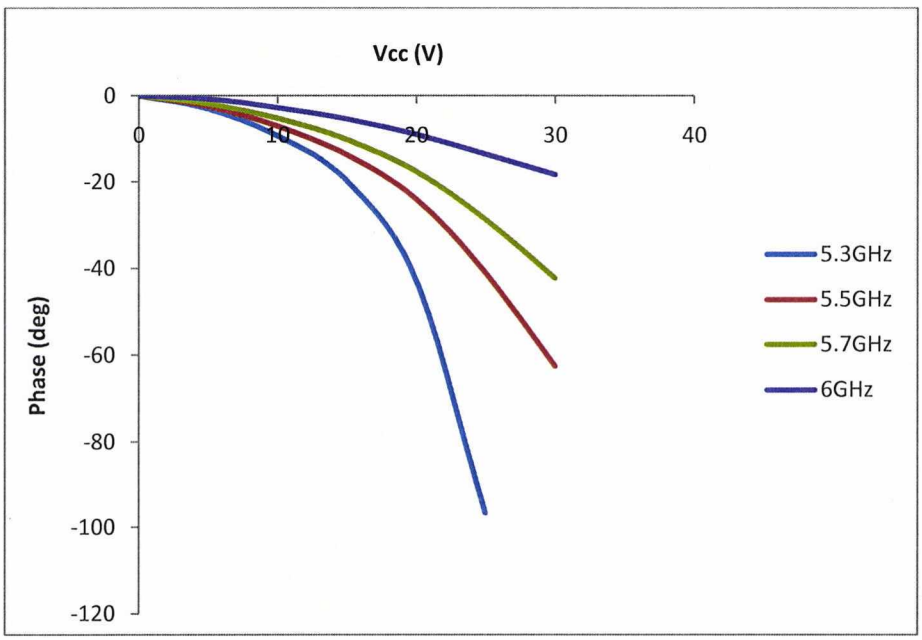

Figure 6.30. Measured phase shift versus voltage (V) for four frequency points

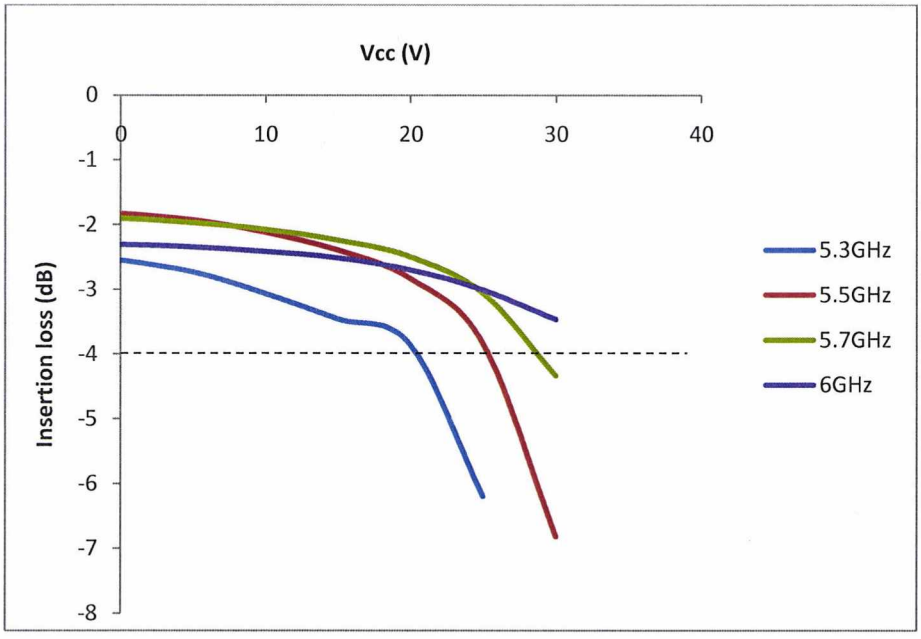

Figure 6.31. Measured insertion losses versus voltage (V) for four frequency points

6.4 Summary

In this chapter, based on the transverse resonance technique (TRT), we introduced a new mathematics method to model the substrate integrated waveguide with loaded components. This method can define the properties of the structure theoretically, and the results match well with that of the simulated and measured.

The half mode substrate integrate waveguide can lose the first mode propagation-which is the half mode solution, if the loaded capacitance is too large. In this case the first mode will occur in the higher order mode range, and by checking the E-field distribution, it turns to the full mode solution.

For capacitive loaded circuit, the fundamental mode may include two types of propagations - the fast and slow modes that are related to the velocity of propagation in the substrate material. We found the governing equations for these two regions and the transition points between them. The different phase constant pattern causes the fundamental mode to

converge to the unusual direction and the loss increases significantly in the slow mode that leads to a frequency dip during the transmission.

We added the non-periodic capacitance to the waveguide first. It makes the cut-off frequency reduce significantly. We have not found the slow mode exists in this case, that is because the transverse resonance technique only can analyse the current vector on the surface.

Then, the research in periodically loaded varactor diodes shows how varying capacitance affects the characteristics of the waveguide. The comparisons between the measured S parameters and dispersion curves are presented. The fast and slow mode propagations compare well in simulated and measured results. Furthermore, as expected, the dips caused by the large loss in the slow mode presented in the measured S parameter results.

In the end of this chapter, a phase shifter design has been demonstrated. It has the tunable performance and only occupies 5 mm longitudinal length. According to figure 6.29 - 6.31, it gives about 50 degrees phase shift for 4dB insertion loss. However, this design is not good, and more improvements need to be done, such as reducing changes in amplitude, linearising the phase response etc.

This work has been accepted by Antennas and propagation symposium 2010 in Cochin, India, Dec 2010.

References

[1] H.-S. Wu and C.-K. C. Tzuang, "Artificially integrated synthetic rectangular waveguide," *IEEE Trans. Microw. Theory Tech.*, vol. 53, no. 9, pp. 2872–2881, Sep. 2005.

[2] R. Coccioli, F.-R. Yang, K.-P.Ma, and T. Roh, "Aperature-coupled patch antenna on UC-PBG substrate," *IEEE Trans. Microwave Theory Tech.*, vol. 47, no. 11, pp. 2123–2130, Nov. 1999.

[3] S. Maci, R. Magliacani, and A. Cucini, "Leaky-wave antennas realized by using artificial surfaces," in *Proc. IEEE Antennas Propag. Int. Symp.*, pp. 1099–1102, 2003.

[4] k.-C. Chen, Y. Qian, C.-k. C. Tzuang, and T. Itoh, "A periodic microstrip radial antenna array with a conical beam," *IEEE Trans. Antennas Propag.*, vol. 51, no. 4, pp. 756–765, Apr. 2003.

[5] C.-k. Wu, Y.-C. Chen, and C.-k. C. Tzuang, "Compressed-width leaky EH mode PBG antenna," *IEEE Microwave Wireless Comp. Lett.*, vol. 13, no. 8, pp. 343–344, Aug. 2003.

[6] D. Deslandes and k. Wu, "Single-substrate integration technique of planar circuits and waveguide filters," *IEEE Trans. Microwave Theory Tech.*, vol. 51, no. 2, pp. 593–596, Feb. 2003.

[7] H. Xin, A. Higgins, J. Hacker,M. kim, and M. Rosker, "Electromagnetic crystal (EMXT) waveguide band-stop filter," *IEEE Microwave Wireless Comp. Lett.*, vol. 13, no. 3, pp. 108–110, Mar. 2003.

[8] H. Xin, A. Higgis, and M. kim, "Tunable millimeter-wave band-stop filter using electromagnetic crystal (EMXT) surfaces," in *2003 IEEE AP-S Int. Microwave Symp. Dig.*, pp. 1107–1110, 2003.

[9] M. N. M.kehn and P.-S. kildal, "The N-guide: a novel miniaturized hard quasi-TEM waveguide," in *Proc. IEEE Antennas Propag. Int. Symp.*, pp. 1111–1114, 2003.

[10] S. Hrabar, J. Bartolic, and Z. Sipus, "Waveguide miniaturization using uniaxial negative permeability metamaterial," *IEEE Trans. Antennas Propag.*, vol. 53, no. 1, pp. 110–119, Jan. 2005.

[11] S. Pioch and J.-M. Laheurte, "Size reduction of microstrip antennas by means of periodic metallic patterns," *Electron. Lett.*, vol. 39, no. 13, pp. 959–961, Jun. 2003.

[12] H.-S. Wu and C.-K. C. Tzuang, "Miniaturized synthetic rectangular waveguide," in *2003 IEEE MTT-S Int. Microwave Symp. Dig.*, Philadelphia, PA, Jun. 8–13, pp. 1099–1102, 2003.

[13] W. J. Chappell, M. P. Little, and L. P. B. katehi, "High Q two-dimensional defect resonators-measured and simulated," in *2000 IEEE MTT-S Int. Microwave Symp. Dig.*, pp. 1437–1440, 2000.

[14] M. J. Hill, R.W. Ziolkowski, and J. Papapolymerou, "Ahigh-Q reconfigurable planar EBG cavity resonator," *IEEE Microwave Wireless Comp. Lett.*, vol. 11, no. 6, pp. 255–257, Jun. 2001.

[15] C.-L. Zhong, J. Xu, Z.-Y. Yu, M.-Y. Wang, and J. H. Li, "Half mode substrate integrated waveguide broadband bandpass filter using photonic bandgap structures," in *Int. Microw. Millimeter Wave Conf. Tech. Dig.*, Nanjing, China, pp. 22–24, Apr. 2008.

[16] Lin Sheng Wu, Xi Lang Zhou, Wen Yan Yin, Chun Tian Liu, Liang Zhou, Jun Fa Mao and Hong Li Peng, "A New Type of Periodicly Loaded Half-Mode Substrate Integrated Waveguide and Its Applications," *IEEE Trans. Microw. Theory Tech.*, vol. 58, no. 12, pp. 882-893, Apr. 2010.

[17] D.Pozar, "*Microwave Engineering*," Second edition, Wiley, 1998.

[18] Fred I. Shimabukuro and C. Yeh, "Attenuation Measurement of Very Low Loss Dielectric Waveguides by the Cavity Resonator Method Applicable in the Millimeter/Submillimeter Wavelength Range," *IEEE Trans. Microw. Theory Tech.*, vol. 36, no. 7, July 1988.

[19] http://docs-europe.origin.electrocomponents.com/webdocs/0278/0900766b8027897c.pdf

[20] Abbosh, A.M., "Ultra-Wideband Phase Shifters," *IEEE Trans. Microw. Theory Tech.*, vol.55, no. 9, pp. 1935-1941, Sep 2007.

[21] Eldek, A.A.," Microstrip 180 degree phase shifter for ultra wideband applications," *IEEE Antennas and Propagation Society International Symposium,* pp. 1-4, 2008.

[22]Xinyi Tang and koen Mouthaan, "180° and 90° Phase Shifting Networks With an Octave Bandwidth and Small Phase Errors," *IEEE Microwave Wireless Comp. Lett.*, vol. 19, no. 8, Aug 2009.

[23] Rober V. Garver, "*Microwave Diode control Devices*," Artech House, Inc, 1976.

[24] Sellal k., Talbi L., Denidni, T.A., and Lebel J., "Design and implementation of a substrate integrated waveguide phase shifter," *IET Microw. Antennas Propag.*, vol. 2, no. 2, pp. 194-199, 2008.

[25] Z. Jin, S. Ortiz, and A. Mortazawi," Design and performance of a new digital phase shifter at X-band," *IEEE Microwave Wireless Comp. Lett.*, vol.14, no.9, pp.428-430, 2004.

[26] S. Cheng, E. Öjefors, P. Hallbjörner, and A. Rydberg, "Compact reflective microstrip phase shifter for traveling wave antenna applications," *IEEE Microwave Wireless Comp. Lett.*, vol.16, no.7, pp.413 433, 2006.

[27] Elisa Sbarra, Luca Marcaccioli, Roberto Vincenti Gatti and Roberto Sorrentino, "Ku-band analogue phase shifter in SIW technology," in *39th European Microwave Conference*, pp. 264-267, 2009.

[28] Abbosh A., Bialkowski M.and Thiel D., "Tunable ultra wideband phase shifter using Liquid Crystal Polymer," *Asia Pacific Microwave Conference*, pp. 2076-2079, 2009.

[29] Cheng Y. J., Hong W. and Wu K., 'Broadband Self-Compensating Phase Shifter Combining Delay Line and Equal-Length Unequal-Width Phaser,' *IEEE Trans. Microwave Theory and Tech.*, Vol 58 , Issue 1, pp. 203 – 210, 2010.

[30] B.Sanz-Izquierdo, E.A. Parker, J.B.Robertson and J.C.Batchelor, "Tuning Technique for active FSS Arrays" *Electron. Letters*, vol. 45, Issue 22, p. 1107-1109. 22 Oct. 2009.

7. Conclusions

As completion, this section includes a summary of the researches and most important results in this thesis. At the end, three brief suggestions for future work are discussed.

7.1 Summary

In chapter 2, two novel composite right/left-handed (CRLH) transmission lines are introduced. One is the planar type and another is via type. They are separated by the shape of electrical scatterers embedded inside the host line. The shielded stripline is applied to be the host line, which has the advantage of no radiation. Both CRLH lines have great left-handed propagation ranges. In the mean time, a method of using transmission matrix analysis to define the equivalent circuit of the structure is proposed. A rough left-handed range can be determined by changing shunt inductance L_L and series capacitance C_L in the matrix. In the same chapter, a discussion of calculating inductance L_L and series capacitance C_L is presented.

Chapter 3 is the general study of the multilayer substrate integrated folded waveguide. The designs of microstrip transmission lines and transitions are presented. This chapter also describe the folded narrowband waveguide, which has the narrow bandwidth with smaller size. At the end of this chapter, the folded half-mode waveguides are introduced. It becomes the fundamental concepts for the next chapter.

In chapter 4, a novel planar half-mode substrate integrated waveguide (HMSIW) has been designed. Maintaining all properties and advantages of original half-mode HMSIW, this

new open structure has no radiation loss and is easy to integrate the planar circuits on the top slot. We also discussed how the open slot affects the loss and bandwidth of the waveguide. Then, a theoretical method to analyse the propagation constant is introduced by using transverse resonance technique (TRT). This mathematical idea gives us the systematic way to determine the cut off frequency of the planar half-mode SIW.

In chapter 5, based on the design of planar half-mode substrate integrated waveguide, a novel pin diode switch has been designed. The propagating mode of waveguide can be switched between two types of mode via the biasing of pin diodes. The periodic loaded method is chosen to integrate pin diodes to avoiding the resonance. This new switchable waveguide can achieve >40dB of isolation up to 3.7GHz, with little resonance and noise.

Chapter 6 introduced a new theoretical analysis to model the substrate integrated waveguide with loaded components and how that affects the properties of propagations. By verifying this method with the simulation, we found that if very large capacitance is loaded on the half-mode waveguide, the waveguide loses the first mode propagation and make it occur in the higher order mode range. By changing the capacitance, the propagation of fundamental mode is managed to control. Furthermore, in a capacitive periodic loaded circuit, the fundamental mode includes two types of propagations – the fast and slow modes. The slow mode is an unusual propagation, which will become very lossy at higher frequency.

Two applications are presented in chapter 6. One is by adding non-periodic capacitance to the waveguide, which reduced the cut-off frequency, but no slow mode. Another one is to periodic load varactor diodes, which brought the fast and slow mode propagations in the fundamental mode.

In the end of this chapter, a novel phase shifter with the tunable performance has been demonstrated. This device has a maximum phase shift of 50 degrees with acceptable return and insertion loss and only occupies 5 mm longitudinal length.

It is hoped that these designs will further enhance the benefits of substrate integrated waveguides.

7.2 Future work

7.2.1 Half-mode substrate integrated waveguide (HMSIW) antenna

The half-mode guide technique is widely applied on the antenna system, such as the leaky-wave antenna [1], the slot antenna [2], frequency scanning antenna [3], etc. Based on the half-mode technique, the antennas have the advantages of easy fabrication and integration with planar circuits, low cost and loss, bandwidth enhancement, and size reduction.

One further research is to design a HMSIW horn type antenna (figure 7.1).

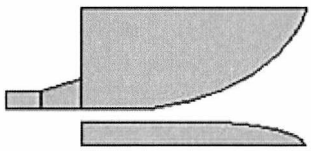

Figure7.1. A HMSIW horn type antenna

One end of the planar half-mode waveguide is modified to be an open side, which has the horn shape. The energy can radiate through the top slot to the far field. The size of the horn part could be well designed to achieve the maximum gain and the lowest return loss.

7.2.2 Composite right/left-handed (CRLH) half-mode substrate integrated waveguide

Recently, a new technique has been developed, which combines the metamaterials transmission lines with the half-mode substrate integrated waveguide (SIW) [4]. The shunt inductances are provided by the via-walls of the waveguide, and the multiple metallised slots on the top create the series capacitances. The unbalanced and balanced cases are easy to be satisfied. The shunt inductances are attributed to the width and height of the waveguide; the series capacitances are controlled by the width and length of top slots.

The advantage of this technique is that it can greatly improve the waveguide miniaturization. The half-mode SIW already has nearly the half cross-sectional area. The metamaterials transmission lines can provide left-handed characteristics which obtain the backward wave passband below the cut off frequency [5] [6]. Therefore, the guide wavelength can be further reduced. The new technique has been applied to some devices, such as dual-band couplers [7].

A future research is to embedding the left-handed transmission line circuits with the planar half-mode SIW.

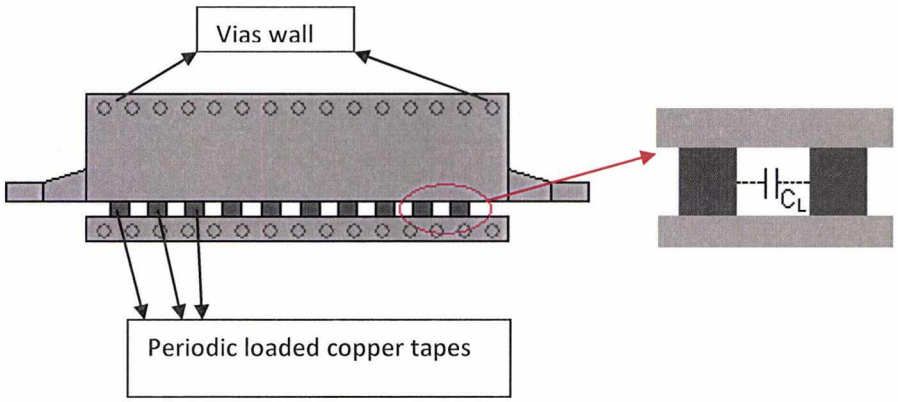

Figure7.2. Planar half-mode SIW embedded left-handed transmission line

Figure 7.2 shows the model of the design. Along the top slot of the planar half-mode SIW, a series copper tapes are periodic loaded. The gaps between two tapes form the series capacitors C_L. The vias wall consists of the shunt inductors.

The distance between each copper plane will determine the series capacitance value, and the height of the planar half-mode SIW will determine the shunt inductance.

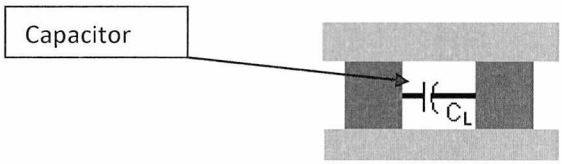

Figure 7.3. Loaded series capacitances

An alternative method of the distributed series capacitances is to load the capacitor components between two copper planes (figure 7.3). This method can greatly increase the series capacitances to satisfy the balanced case of CRLH line:

$$L_R \times C_L = L_L \times C_R \tag{7.1}$$

7.2.3 The switchable CRLH transmission line

A further improvement is to design a switchable CRLH transmission line. By series embedding biasing controlled pin diodes between two copper planes (figure 7.4), the transmission can be switched between the normal waveguide propagation and left-handed distribution transmission line. In this case, the taper need to be redesigned.

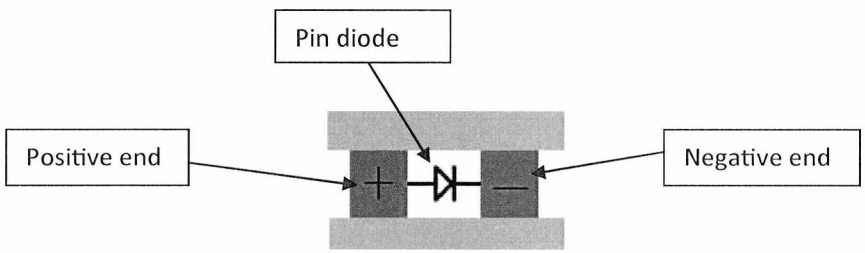

Figure 7.4. Embedded pin diodes

The bias problems need to be considered in this design. We can try to embed the positive and negative end into different layers, and use the insulator to separate two parts.

7.2.4 The planar half-mode SIW embedded Gunn diodes

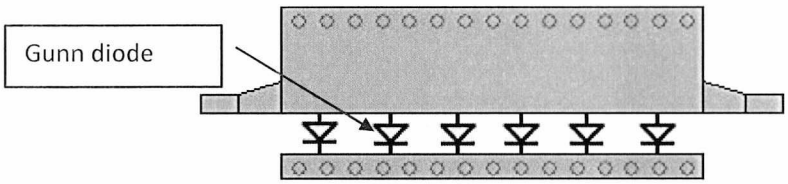

Figure 7.5. Geometry of planar half-mode SIW embedded Gunn diodes

Furthermore, we could embed the gunn diodes into the planar half-mode SIW (figure 7.5). The Gunn diode is a transferred electron device used in high frequency range. It can provide negative resistance in which case the attenuation constant becomes positive. Therefore, the resistive loss can be considered as the gain of the waveguide. This technique has applications in amplifiers [8], generators [9] and Gunn diode sources [10].

These designs are very promising as long as the structure has been well optimized.

References

[1] Junfeng Xu, Wei Hong, Hongjun Tang, Zhenqi Kuai, and Ke Wu, "Half-Mode Substrate Integrated Waveguide (HMSIW) Leaky-Wave Antenna for Millimeter-Wave Applications," *IEEE Antennas and Wireless Propag. Lett.*, Vol.7, 2008.

[2] Liang Wu, Izquierdo, B.S., and Young, P.R., "Half mode substrate integrated waveguide slot antenna, " *IEEE Antennas and Propagation Society International Symposium*, APSURSI, pp. 1-4, 2009.

[3] Yu Jian Cheng, Wei Hong, and Ke Wu," Millimeter-Wave Half Mode Substrate Integrated Waveguide Frequency Scanning Antenna With Quadri-Polarization," *IEEE Trans. Antennas Propag.*, vol. 58, no. 6, pp.1848-1855, 2010.

[4] Y. Dong and T. Itoh, "Composite right/left-handed substrate integrated waveguide and half-mode substrate integrated waveguide," in *IEEE MTT-S Int. Microw. Symp. Dig., Boston,* USA, pp. 49-52, 2009.

[5] G. Eleftheriades and K. Balmain, *Negative Refraction Metamaterials: Fundamental Principles and Applications*, New York, Wiley-IEEE Press, 2005.

[6] C. Caloz and T. Itoh, *Electromagnetic Metamaterials: Transmission Line Theory and Microwave Applications.* New York: Wiley-IEEE Press, 2005.

[7] Dong Yuandan, Itoh Tatsuo, "Application of composite right/left-handed half-mode substrate integrated waveguide to the design of a dual-band rat-race coupler," *IEEE MTT-S International_Microwave Symposium Digest (MTT)*, pp. 712-715, 2010.

[8] Elad D., Nahoum A., "Ka band Gunn diode amplifiers," *17th Convention of Electrical and Electronics Engineers in Israel*, pp. 373 – 374, 1991.

[9] Klamka, J., Parafianowicz, J., Uszynski, A., "Gunn diode generator for frequency band 26-40 GHz," *13th International Conference on Microwaves, Radar and Wireless Communications*, vol. 2, no. 2000, pp. 699-702, August 2000.

[10] D.Pozar, "*Microwave Engineering*," Second edition, Wiley, 1998.